

FILLING BOX FLOWS IN POROUS MEDIA

by

Chunendra Kumar Sahu

A thesis submitted in partial fulfillment of the requirements for the degree of

Doctor of Philosophy

Department of Mechanical Engineering
University of Alberta

© Chunendra Kumar Sahu, 2016

Abstract

Drawing on ideas from turbulent plume theory, a novel solution is presented for buoyant convection from an isolated source in uniform and non-uniform porous media of finite extents. In the former case, the problem is divided into three flow regimes: (i) a negatively-buoyant plume, (ii) rectilinear or axisymmetric gravity current comprising discharged plume fluid that forms when the plume reaches the bottom (impermeable) boundary, and, (iii) the subsequent ascending motion of this discharged plume fluid towards the source after the gravity current reaches the vertical side walls.

We derive analytical solutions for all three regimes in a rectilinear geometry with a line source and in an axisymmetric geometry with a point source. By synthesizing the above three flow regimes, a “filling box” model is developed that can predict the time needed for a source of dense fluid to fill the control volume up to the point of overflow as a function of the source and reservoir parameters. For purposes of corroborating our model predictions, complimentary rectilinear laboratory experiments were performed with fresh water and salt water as the working fluids. Images were recorded during the experiments and later post-processed in Matlab by employing an interface detection algorithm to determine the height profiles of the gravity current and the first front. We find good agreement between the measured and predicted height profiles.

Extending the above results to a nonuniform porous medium, the effects of sudden permeability changes in a filling box flow are studied for the case of rectilinear geometry. The porous medium consists of two thick horizontal layers of different permeabilities. Two configurations are examined: a lower permeable medium on top of the higher permeability layer and vice-versa. While the

flow dynamics observed in the first configuration are qualitatively similar to the case of a uniform porous medium, a significantly different flow behaviour is observed in the latter configuration. Here not all of the plume fluid enters the lower layer. Rather some significant fraction propagates along the (horizontal) interface between the upper and lower layers as an intrusive gravity current exhibiting fingering instabilities along its bottom surface. Depending on the source parameters and permeability ratio, the gravity current can reach only a certain length before draining completely into the lower layer. Analytical solutions are presented for this runout length and the corresponding filling box time. Similitude experiments were then also performed to verify these predictions. While we find a good agreement in case of the filling box time, for the runout length an underprediction is observed. Reasons for this discrepancy are carefully examined.

Preface

This thesis is an original work by Chunendra K. Sahu. The mathematical formulations of Chapters 2, 3 and 4 are derived by myself, with the assistance of Dr. M. R. Flynn. Moreover, the experimental setups presented in Chapters 2 and 4 were designed by myself, with the assistance of Dr. M. R. Flynn, Mr. Mark Roes and University of Alberta, Department of Mechanical Engineering Technical Resources Group.

Chapter 2 of this thesis has been published as C. K. Sahu and M. R. Flynn, “Filling box flows in porous media”, *Journal of Fluid Mechanics*, vol. 782, 2015, 455–478. Chapter 3 of this thesis has been published as C. K. Sahu and M. R. Flynn, “Filling box flows in an axisymmetric porous medium”, *Transport in Porous Media*, vol. 112, 2016, 619–635. Chapter 4 of this thesis has been submitted for publication to *Journal of Fluid Mechanics* as C. K. Sahu and M. R. Flynn, “The effect of sudden permeability changes in porous media filling box flows” on May 6, 2016. I was responsible for theoretical developments, data collection and analysis as well as the manuscript writing. Dr. M. R. Flynn was the supervisory author and was involved with concept formations and manuscript revisions.

To all members of my beloved *Maaya* family

Acknowledgements

I sincerely thank and show my great regards to Dr. Morris Flynn, first for having given me this opportunity to pursue PhD under his supervision and then for his exceptional guidance through the course of my PhD program. His dedication to research and commitments as a supervisor have been continuous sources of inspiration and motivation for my research work. After years of working with him, I am proud to call him my mentor.

I wish to acknowledge the fruitful discussions with Dr. Carlos Lange and Dr. Marc Secanell through our committee meetings. Their constructive feedbacks have been non-trivial in making research progress and planning appropriate timeline for my PhD program. I owe much gratitude to several professors at the University of Alberta, explicitly Dr. Bruce Sutherland, Dr. Andrew Martin and Dr. Hassan Dehghanpour. I wish to thank Dr. Saleh Nabi, a senior member from our group, for his help and continuous encouragement and other group members, Mr. Mark Roes and Mr. Mitch Nocholson, for their assistance. The assistance of the University of Alberta, Department of Mechanical Engineering Technical Resources Group is also acknowledged with thanks. Financial support for this study was provided by NSERC through the Discovery Grant and RTI Programs and Carbon Management Canada.

A big thank to all my friends and fellow students at the University of Alberta with whom I have shared this big adventure. Finally, I would like to show much appreciation to my wonderful parents, siblings and family for always being very supportive and having faith in me.

Contents

1	Introduction and overview	1
1.1	Literature review	5
1.2	Applications	11
1.2.1	Geothermal energy recovery	11
1.2.2	Geological carbon sequestration	12
1.2.3	Leakage and contamination of DNAPL into groundwater	13
1.2.4	Solar thermal storage	14
1.2.5	Confined porous enclosures	15
1.3	Present contribution and thesis organization	15
2	Filling box flows in a rectilinear geometry	19
2.1	Abstract	19
2.2	Introduction	20
2.3	Theory	24
2.3.1	Plume in an unbounded medium	24
2.3.2	Gravity current	30
2.3.3	First front	34
2.4	Laboratory set-up and experiments	36
2.5	Results and discussion	39
2.6	Conclusions	47
3	Filling box flows in an axisymmetric geometry	50
3.1	Abstract	50
3.2	Introduction	51
3.3	Plume	56
3.4	Gravity current	63
3.5	First front	66
3.6	Discussion	67

3.7	Conclusions	70
4	The effects of sudden permeability changes in porous media filling box flows	73
4.1	Abstract	73
4.2	Introduction	74
4.3	Experimental technique	78
4.3.1	Laboratory set-up and experiments	78
4.3.2	Experimental images	80
4.4	Theoretical development	89
4.4.1	Permeability ratio $k_1/k_2 < 1$	90
4.4.2	Permeability ratio $k_1/k_2 > 1$	96
4.5	Comparison between theory and experiment	100
4.6	Conclusions	105
5	Summary and conclusions	108
5.1	Primary contributions from the present work	113
5.2	Future work	114
	Appendices	117
A	Rectilinear plumes in Darcy regime with $Pe \lesssim \mathcal{O}(1)$	118
B	Axisymmetric plumes in Darcy regime with $Pe \lesssim \mathcal{O}(1)$	121
C	Curved interface methodology	123
D	Uniform porous medium experimental details	125
E	Layered porous medium experimental details	127
F	List of symbols	130

Chapter 1

Introduction and overview

A “filling box flow” can be defined as the buoyant convection that arises in a closed or ventilated control volume where the convection is driven by a localized source on the boundary that produces an ascending or descending plume. This plume, after reaching the opposite impermeable horizontal boundary, forms laterally propagating gravity current(s) that propagate towards the vertical sidewalls of the control volume. After the gravity current(s) reach the sidewalls, there appears a layer of discharged plume fluid that progressively deepens with time. In the long time limit, this discharged plume fluid is returned to the elevation of the source. A schematic of a representative filling box flow in porous media is shown in figure 1.1.

Filling box flows were first studied in the context of free turbulent plumes by Baines & Turner (1969), who considered a closed control volume filled with ambient fluid but devoid of porous media. Although there have been significant investigations of filling box flows in a free medium since then, in the context of a porous medium this problem still remains unexplored. From the environmental to industrial applications, e.g. underground thermal storage, cooling of electronic components etc., filling box type flows occur in porous media in numerous incarnations (to be discussed in detail in §1.2). Findings from the present investigation of filling box flows in porous media can be employed in these applications to determine the maximum amount of fluid, solute or heat that may be sequestered and the associated filling box time.

As shown in figure 1.1, filling box flows consist of three flow regimes: (i)

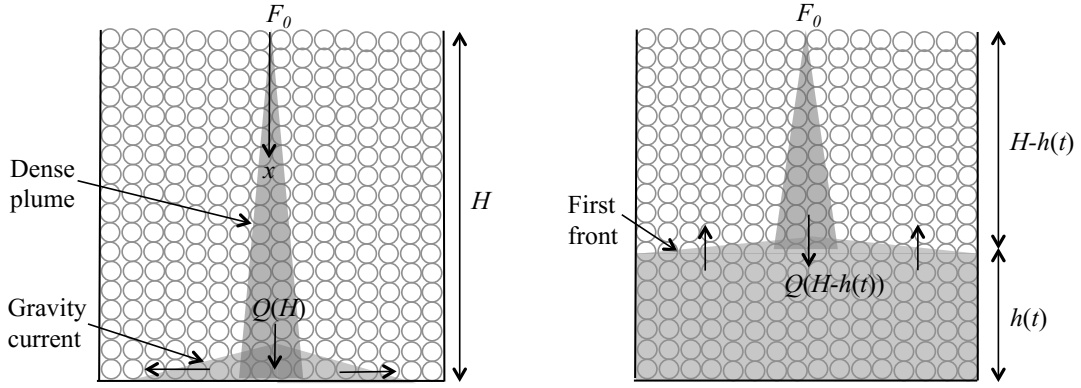


Figure 1.1: Convection in a confined porous medium: (a) plume and gravity current flow, (b) advection of the first front towards the source.

a negatively-buoyant plume originating from a discrete source, (ii) gravity current(s) moving horizontally sideways or outwards and (iii) a “first front” moving vertically upwards towards the source of the negatively-buoyant plume. Plumes are defined as a primarily vertical, buoyancy driven flow, generated from a local source. The buoyancy difference between the source and ambient fluids may be caused by a difference either in the solute concentration (haline plumes) or temperature (thermal plumes). However, if the source has both concentration and temperature differences, the plume is of thermohaline type. Because of the difference in the fluid velocity between the plume and ambient fluids, an entrainment of the latter into the former occurs resulting in an increase in the volume flux of the plume. Buoyant plumes are primarily characterized by three parameters: the volume flux, momentum flux and the buoyancy flux. For an ideal plume, the volume flux and momentum flux at the source are assumed to be zero such that the plume is generated as a result only of a source buoyancy flux. However, in reality, particularly in case of haline plumes, the volume flux and momentum flux at the source are almost always nonzero. An example of a negatively-buoyant plume in porous media is shown in figure 1.2. Notice that the plume diameter increases in the downstream direction which is indicative of an entrainment of (clear) ambient fluid into the (dark) plume fluid.

The second component of filling box flows, i.e. the gravity current, is a pri-

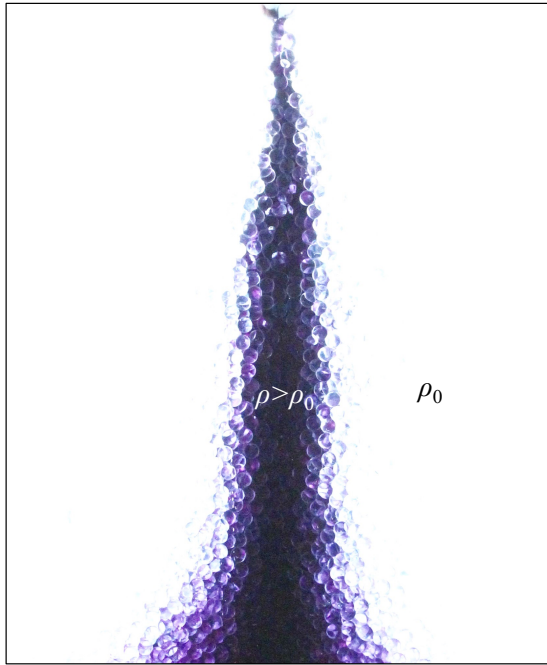


Figure 1.2: A (dark) dense plume falling in a uniform porous medium filled with a (clear) light fluid.

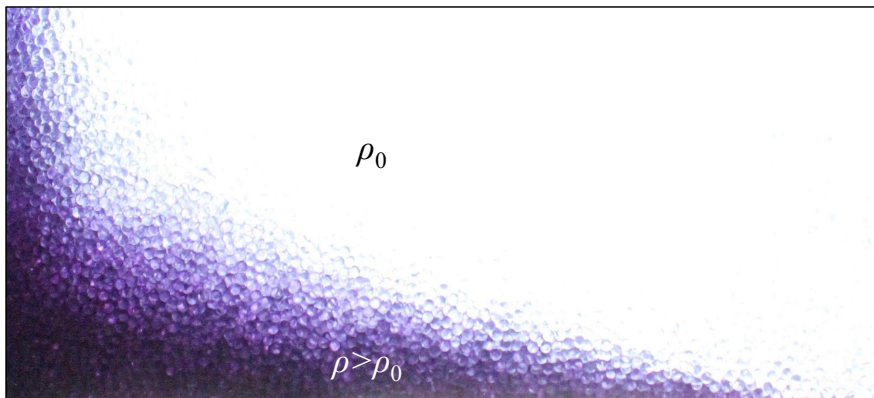


Figure 1.3: A dense gravity current propagating outwards over a horizontal impermeable boundary in a uniform porous medium.

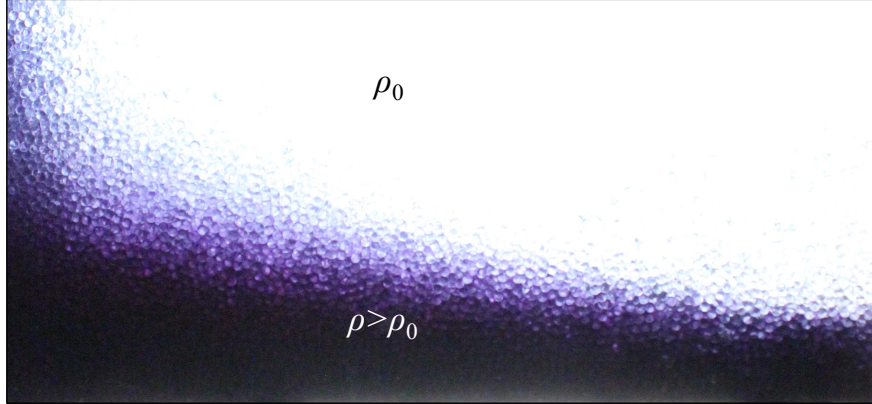


Figure 1.4: Image showing the advection of first front having a curved interface in a confined porous medium.

marily horizontal flow, driven by the density-difference between the contaminated and ambient fluids. A gravity current is created by dense fluid in a lighter ambient, over an impermeable or a less permeable boundary. Unlike the case of the plumes, no significant entrainment occurs in this case, and therefore the density of the gravity current is assumed to be constant during its propagation. An example of the dense gravity current flowing over an impermeable boundary is shown in figure 1.3. Because gravity currents are invariably considered as semi-infinite flows, a new flow classification is needed for the period of time after the gravity current first strikes a lateral sidewall. The interface between the contaminated fluid and the ambient light fluid is known as the “first front” (Baines & Turner, 1969). The motion of the first front is primarily vertical, and any diffusive or turbulent entrainment across the first front is neglected over advection. A sample image showing the first front can be found in figure 1.4.

It is important to note that all of the above discussion assumes a negatively-buoyant plume that falls through an ambient of comparatively light fluid. In fact, provided the system is Boussinesq so that density differences are comparatively small (i.e. $\lesssim 10\%$), entirely equivalent dynamical results would be obtained if a source of a light fluid is located at the bottom of the control volume that is filled with a comparatively denser fluid, thereby creating a rising light plume, followed by a light gravity gravity current(s) flow below the top impermeable boundary

and finally a subsequent downwards advecting first front.

1.1 Literature review

Mathematical derivations describing the behavior of free turbulent plumes were presented by (Morton *et al.*, 1956). The set of 1D integral equations that describe the variation of the plume volume flux, momentum flux and reduced gravities with the vertical coordinate, z , were then termed as the MTT equations. By adapting the MTT equations for axisymmetric turbulent free plumes, Baines & Turner (1969) studied filling box flows in a confined rectangular box devoid of porous media. While the horizontal outflow, i.e. the gravity current, of the plume upon reaching the impermeable boundary was omitted, the vertical flow obtained after this outflow reaches the lateral sidewalls was characterized with reference to the time dependent elevation of the “first front”, the interface that separates contaminated and uncontaminated (ambient) fluid. For an ideal plume having zero source volume (and momentum) flux, Baines & Turner (1969) found that the first front reaches the top of the control volume asymptotically at large time. The gravity current part that was omitted by Baines & Turner (1969) was considered later by several researchers like Britter (1979); Manins (1979); Kaye & Hunt (2007) and others.

In considering free turbulent plumes, the behavior of the plume outflow greatly depends upon the ratio of the box height to radius, H/R . If this ratio is sufficiently large, i.e. $H/R \gtrsim 4.0$ according to Barnett (1991), the discharged plume fluid fails to form a stable horizontal interface. Rather, because of the smaller box cross-section, the discharged dense fluid upon reaching the sidewall overturns. The overturning of the discharged fluid, based on H/R , is studied by Kaye & Hunt (2007) in detail. By contrast, overturning type motions are not believed to be significant in porous media filling box flows where the flow is laminar and inertial effects are much smaller by comparison.

Since the investigation of Baines & Turner (1969), filling box flows have been studied in significant detail in the context of numerous industrial and environmen-

tal applications. Some of the primary applications include: building ventilation (Caulfield & Woods, 2002; Nabi & Flynn, 2013), overturning in chemical storage tanks (Germeles, 1975), submarine pumice plumes (Head & Wilson, 2003; Woods, 2010), hydrothermal plumes (Speer & Rona, 1989; Baker *et al.*, 1989), seafloor lava eruptions (Speer & Marshall, 1995; Bush & Woods, 1999) and atmospheric volcanic plumes (Woods, 2010).

Although filling box type flows are not an unusual occurrence in porous media (examples to be discussed in §1.2), they have, with the exception of Roes *et al.* (2014), remained unexplored from a theoretical point of view. By assuming a leaky porous medium, Roes *et al.* (2014) studied the effects of fissure outflow on the long time behavior of the filling box flow. Consistent with Linden *et al.* (1990), they found that in the $t \rightarrow \infty$ limit the first front height reaches a constant value and the volume flux at the elevation of the first front equals the volume flux exiting through the fissures. They characterized the mean first front height based on the number and size of the fissures, the source parameters and the porous media properties, i.e. the porosity and permeability.

Although filling box flows in porous media have not been studied significantly, a reasonably voluminous literature has accumulated that seeks to describe the behavior of plumes and gravity currents in porous media. Before discussing the relevant papers in further detail, it is however vital to first understand the basics of flow and transport in porous media.

Flows in porous media are characterized primarily by two dimensionless numbers: Reynolds number, Re , and Péclet number, Pe . The Reynolds number gives the ratio of inertia to viscous dissipation. Mathematically, $\text{Re} = \frac{d_0 U}{\nu}$, where d_0 is the mean grain diameter, U is the average transport velocity, and ν is the kinematic viscosity. If $\text{Re} \lesssim \mathcal{O}(10)$, the flow regime is assumed to be laminar and hence

$$\frac{\mu}{k} \mathbf{u} = -\frac{\partial P}{\partial \mathbf{x}} + \rho \mathbf{g}, \quad (1.1)$$

where \mathbf{u} is the transport velocity in any direction \mathbf{x} , ρ is fluid density, μ is dynamic viscosity and \mathbf{g} is the gravitational acceleration. Moreover, k is the permeability that works as a constant of proportionality in above equation. It defines the ease

with which fluid can pass through a porous medium, and depends primarily on the porosity, ϕ , and d_0 . For instance, a porous medium comprised of particle grains has a permeability of $k = \frac{d_0^2 \phi^{5.5}}{5.6}$, which is an empirical formula given by Rumpf & Gupte as presented in Dullien (1992). Equation (1.1) is one of the forms of Darcy’s equation (Bear, 1972; Nield & Bejan, 2013). It describes momentum conservation for porous media flow and is therefore the analogue of the Navier-Stokes equations for flows that occur outside of a porous medium. Darcy’s equation is based on a series of assumptions that flow is steady, isothermal and incompressible, the cross-section of the flow is uniform and the medium has uniform porosity and permeability (Bear, 1972). If $\text{Re} > \mathcal{O}(10)$, the flow is no longer Darcy. Rather inertial effects, which were neglected in the derivation of Darcy’s law, become significant. To account for the inertia term, Forchheimer presented a modified form of Darcy’s equation, now popularly known as the Darcy-Forchheimer equation (Nield & Bejan, 2013; Nield & Kuznetsov, 2013). It reads

$$\frac{\mu}{k} \mathbf{u} + \frac{c_F}{k^{1/2}} \rho \mathbf{u}^2 = -\frac{\partial P}{\partial \mathbf{x}} + \rho \mathbf{g}. \quad (1.2)$$

Here c_F is an inertial coefficient, which for flow through particle beds can be defined using Ergun’s formula as $c_F = \frac{1.75}{150^{1/2} \phi^{3/2}}$ (Ergun, 1952; Nield & Kuznetsov, 2013). Note, moreover, that in case of high viscous flows or when the grains of the porous medium are themselves porous, another modified form of Darcy’s law should be employed which is known as Darcy-Brinkman equation and reads

$$\frac{\mu}{k} (\mu_e \nabla^2 \mathbf{u} + \mathbf{u}) = -\frac{\partial P}{\partial \mathbf{x}} + \rho \mathbf{g}. \quad (1.3)$$

Here, $\mu_e = \frac{\mu}{\phi \tau}$ is an effective viscosity term (Nield & Kuznetsov, 2013). Moreover, τ is the flow path tortuosity, i.e. the ratio of total length travelled by a fluid particle to that it would travel devoid of porous materials.

The Péclet number, on the other hand, gives a ratio of mass transport by mechanical dispersion vs. molecular diffusion. Mathematically, $\text{Pe} = \frac{d_0 U \tau}{D_d}$, where D_d is the molecular diffusion coefficient. If $\text{Pe} \lesssim \mathcal{O}(1)$, the molecular diffusion part, D_d/τ , dominates over the mechanical dispersion part, $d_0 U$, and vice-versa

when $Pe \gtrsim \mathcal{O}(1)$. The formula for the dispersion coefficient reads

$$D = d_0 U \left(1 + \frac{1}{Pe} \right). \quad (1.4)$$

Thus if the velocity is large such that $Pe \gg \mathcal{O}(1)$, the dispersion coefficient becomes strongly dependent on the flow-field and basically independent of molecular effects. Thus the details of the mass transfer are significantly different from the case where $Pe \ll \mathcal{O}(1)$, a difference that must be reflected in the form and solution of the relevant governing equations.

By assuming Darcy's regime with $Pe \lesssim \mathcal{O}(1)$, such that $D_d/\tau \ll d_0 U$, Wooding (1963) derived a similarity solution for laminar plumes in porous media. For the rectilinear and axisymmetric geometries, Wooding's formulas for plume volume flux read

$$Q = \left(\frac{36 D_d \phi F_0 k \Lambda^2 x}{\nu} \right)^{1/3} \quad \text{and} \quad Q = 8\pi D_d \phi x, \quad (1.5)$$

respectively. Here, F_0 is the source buoyancy flux and Λ is the width of line source (Phillips, 1991). The complete derivations of Wooding's formulas can be found in Appendices A and B for the rectilinear and axisymmetric geometries, respectively.

Wooding's solution was later extended to a non-Darcy regime by several researchers like Chen & Ho (1986), Lai (1991) and Nakayama (1994) for the line source and Leu & Jang (1995) for the point source. While Chen & Ho (1986) and Nakayama (1994) considered $Pe \lesssim \mathcal{O}(1)$, Lai (1991) and Leu & Jang (1995) assumed $Pe \gg \mathcal{O}(1)$. Because of the non-linearity of the velocity term in the Darcy-Forchheimer equation as in (1.2), finding an analytical solution in the non-Darcy flow regime is not always feasible or straightforward. Therefore most of the above papers present only numerical solutions of porous media plume flows. Moreover, the above mentioned examples consider only one type of source whether haline or thermal. There are, on the other hand, applications such as packed-bed catalytic reactors and enhanced oil recovery where the plume buoyancy is due to both heat and the presence or absence of a dissolved constituent, thus creating thermohaline plumes (Jumah *et al.*, 2001). Therefore, adding more complications to the

above plume models, several researchers like Nield (1968), Bejan & Khair (1985) and Jumah *et al.* (2001) studied thermohaline plumes in porous media by simultaneously considering advection-diffusion equations for heat and a solute. This necessitates the introduction of two dispersion coefficients. While the mechanical dispersion coefficient as in (1.4) works well for solute transport, a thermal diffusivity constant must be used when considering thermal transport. Regarding momentum conservation, while Nield (1968) and Bejan & Khair (1985) assumed that Darcy’s law is valid, Jumah *et al.* (2001) extended the problem into the Darcy-Forchheimer regime.

We found that plume solutions are available in the literature for a very broad range of Péclet numbers in the non-Darcy regime. On the contrary, in the Darcy flow regime a solution has been derived only for $Pe \lesssim \mathcal{O}(1)$. However, plumes in a Darcy regime with $Pe \gtrsim \mathcal{O}(1)$ are not at all unusual. This can be explained by introducing a Schmidt number, Sc , that is defined as the ratio of momentum to mass diffusion. Symbolically, $Sc = \nu/D_d \equiv Pe/Re$, where ν is the fluid kinematic viscosity. For instance, the Schmidt number for salt water at room temperature and pressure is $Sc \approx 1000$ within the limits of the Boussinesq approximation (Ramsing & Gundersen, 1994). Likewise the Schmidt number of supercritical CO_2 (sc- CO_2) in underground brine is $Sc \approx 400$ (Kestin *et al.*, 1981; Iglauer, 2011) and that of dense non-aqueous phase liquids (DNAPL), e.g. tetrachloroethene, in groundwater is $Sc \approx 1000$ (Watch *et al.*, 2014). These large values imply that if $Re \lesssim \mathcal{O}(10)$, then $Pe \gtrsim \mathcal{O}(1)$. Motivated by the above discussion, we derive novel self-similar solutions for laminar plumes with $Pe \gtrsim \mathcal{O}(1)$ for the line and point source cases. These solutions are respectively presented in Chapters 2 and 3.

The second part of filling box flows, i.e. gravity currents, have been studied widely in uniform porous media. It should be noted, however, that these studies were not performed in the context of filling box flows but rather in consideration solely of the dynamics of the primarily horizontal (and therefore hydrostatic) flow. Relevant examples include Huppert (1986), Huppert & Woods (1995), Lyle *et al.* (2005) and others. Huppert & Woods (1995) presented a similarity solution

for gravity current propagation over an impermeable horizontal boundary in a rectilinear geometry with a line source, whereas in the case of an axisymmetric geometry with a point source, a similarity solution was presented by Lyle *et al.* (2005). The similarity solutions so obtained were extended to find the height profiles and the distance of the gravity current leading edge from the source against time, t . Huppert & Woods (1995) found that for a constant volume flux line source, the height and extent of the gravity current edge should respectively vary as $t^{1/3}$ and $t^{2/3}$. Conversely, in case of a point source with constant volume flux, Lyle *et al.* (2005) confirmed that the extent of the gravity current leading edge should vary with $t^{1/2}$, whereas the height profile should be constant and independent of time, provided $t \neq 0$. This problem has been studied further in porous media with some additional complications, for example one including an inclined surface (Vella & Huppert, 2006; Gunn & Woods, 2011), two-layer gravity currents (Woods & Mason, 2000), or a localized sink/vertical fracture (Neufeld *et al.*, 2011; Pritchard & Hogg, 2002). Studies have also been made of gravity current flow over layered porous medium (Pritchard *et al.*, 2001; Neufeld *et al.*, 2009; Goda & Sato, 2011).

In the first part of the current research, we consider a uniform porous medium. The similarity solutions presented by Huppert & Woods (1995) and Lyle *et al.* (2005) are therefore appropriately adapted in our models. The similarity solutions are used to define the propagation of the gravity currents in terms of height and length vs. time. In the latter part of our investigation, where a sudden change in permeability is considered, Goda & Sato (2011)'s numerical solution is correspondingly adapted. More precisely, we use the asymptotic solution presented by Goda & Sato (2011) to predict the long time behavior of a gravity current flowing in a layered porous medium. As shall be outlined in much greater below, comparisons can then be made against the measurements made in analogue laboratory experiments.

1.2 Applications

Just as with standard filling box flows, those that arise within a porous medium are related to several industrial and environmental phenomena. Some notable examples are subterranean thermal storage, carbon sequestration, DNAPL leakage into potable water, solar thermal storage and the cooling of electrical components.

1.2.1 Geothermal energy recovery

Geothermal energy recovery is a method of injecting cold fluid into a hot aquifer for subsequent extraction and industrial/domestic use. In other words, this is a method of recovering geothermal energy for the purpose of fulfilling energy needs without the combustion of coal or natural gas. With the depletion of fossil fuels (Sauty *et al.*, 1982; MacKay, 2009), and aiming towards a low carbon environment (Dickinson *et al.*, 2009), geothermal energy represents an effective sustainable source of energy. According to Sauty *et al.* (1982), in the harnessing of geothermal energy two factors are important above all others: the recovery factor and the energy level in the recovered water. While the former defines the ratio of thermal energy recovered to that injected, the latter indicates the level of thermal energy available in the recovered water. However, both parameters depend upon the effective filling and extraction of the fluids and the reservoir's physical properties, e.g. porosity and permeability. Thus when the porosity and permeability are large so that water easily flows through the reservoir, the recovery factor and energy level increase.

Generally a single bore or two bore system is used for the operation of geothermal energy recovery (Nordell, 2000). While in the former the same bore is used for injection and production, the latter one has a separate bore for the injection and extraction processes. The observed flow closely resembles that of a filling box, particularly in the former case when injecting cold fluid into a hot aquifer. Because the injected fluid and the already existing ambient fluid are water of low and high temperatures, respectively, a dense negatively-buoyant plume is created if the injection point is towards the top of the aquifer. A gravity current is sub-

sequently formed when the cold water plume reaches the bottom impermeable boundary. If, on the other hand, the injection well is at the bottom of the aquifer, only the gravity current is formed Woods (1999); Dudfield & Woods (2012). In both cases, the aim is to eventually fill the pore space with a maximum amount of cold fluid that can be later extracted in the form of hot fluid. Filling box flow concepts can be applied when calculating the maximum possible injection rate based on the source and reservoir conditions. Moreover, because geothermal energy recovery is operated on a cyclic basis depending on energy demand, the timescales associated with the injection and extraction of fluids are nontrivial variables. Given the reservoir's specification, the rate of injection and the associated timescales can be optimized using the analytical formulas presented later on in this thesis.

1.2.2 Geological carbon sequestration

Carbon sequestration is a process of injecting anthropogenic CO₂ underground to a depth of greater than 750 m with an aim of mitigating global warming (Bickle, 2009). The complete process consists of capturing CO₂ from a localized source e.g. industrial chimneys, then compressing it to a supercritical state (sc-CO₂) and finally injecting this fluid into a deep saline aquifer. The injected fluid stays in the supercritical phase and has a lower density than that of the surrounding brine, yielding a buoyant plume of sc-CO₂ that rises through the aquifer (Bolster, 2014). Upon reaching the upper impermeable boundary of a particular aquifer, this plume then propagates sideways in the form of gravity currents, creating a layer of CO₂-rich material (Riaz *et al.*, 2006). Although the sc-CO₂ has only a very limited solubility in the brine, the vast quantities of the latter suggest that, in a long time limit, sc-CO₂ ultimately dissolves into the brine as observed in the experimental investigation of Kneafsey & Pruess (2010). After dissolving, a dense layer of CO₂-rich brine is formed whose density is greater than the uncontaminated brine that appears underneath (Riaz *et al.*, 2006). The resultant mixture therefore flows downward towards the lower impermeable boundary. The overall process of mixing of CO₂ in brine is called “convective dissolution”

(Neufeld *et al.*, 2010; MacMinn *et al.*, 2012; Szulczewski *et al.*, 2013). From the point of view of safe, long-term storage, it is very important that the CO₂-rich brine moves downward instead of sc-CO₂ moving upwards and escaping to the surface level (Bolster, 2014). Furthermore, apart from convective dissolution, the capillary trapping of sc-CO₂ in a brine aquifer plays an equally important role in permanently and safely sequestering anthropogenic CO₂ (Huppert & Neufeld, 2014).

While other factors like cost and long time feasibility are important parameters to be considered in connection with geological sequestration, both the timescales associated with convective dissolution as well as the storage capacity, i.e. the maximum possible mass of sc-CO₂ that may be injected into an aquifer of fixed volume, are equally important. Filling box timescales are therefore important in estimating the timescales for completely contaminating the available pore space in a particular saline aquifer with the mixture of dissolved sc-CO₂ and brine.

1.2.3 Leakage and contamination of DNAPL into groundwater

Dense nonaqueous phase liquids (DNAPL), e.g. creosote, coal tar and chlorinated solvents, are generally denser than underground potable water and also slightly soluble (Kueper *et al.*, 2003). Indeed, the infiltration of DNAPL through the vadose zone, i.e. the unsaturated zone between the surface and the underground water table, then into the potable groundwater is considered as one of the most dangerous forms of groundwater contamination. This contamination is, in turn, linked to a myriad of health problems. After reaching to the depth of water table, a dense plume of DNAPL is created. When, as is typically the case, the groundwater has its own velocity, the chances of spreading the DNAPL are significantly increased. To try to limit the reach of dissolved DNAPL, it is important to consider the timescale associated with the rate of mixing due to the vertically downwards flow and subsequent horizontal outflow along a particular lens or other impermeable layer (Khachikian & Harmon, 2000). For understanding the overall process of leakage, dissolution and movement of DNAPL into potable groundwater, the equations describing the DNAPL plume volume flux and re-

duced gravity are necessary; by extension, the concepts associated with filling box flows may prove helpful.

1.2.4 Solar thermal storage

The increasing popularity of renewable energy has accelerated research on solar thermal storage. One particular technology employs phase change materials (PCM) encapsulated within spherical or cylindrical capsules (Nallusamy *et al.*, 2007; Dutil *et al.*, 2011). The storage of thermal energy in PCMs can happen both by way of sensible and latent energies. The PCM capsules are generally kept inside an insulated cylindrical box and the pore space is filled with water, thus creating a saturated porous medium (Sarafraz, 2013). The addition or subtraction of thermal energy from the storage are done by a coiled heat exchanger that works as an areal source of heating or cooling. The heat exchanger contains a charge fluid that is warmed by solar collectors and circulated by a pump. During the daytime, the capsules are warmed as a result of the absorption of solar energy by the charging fluid. The PCM therefore melts. At night, by contrast, thermal energy may be needed for domestic heating and the heat energy is extracted in the form of thermal or latent energy from the storage through the cooling and subsequent solidification of PCM materials. Nizami *et al.* (2013) explain and numerically study the formation of negatively-buoyant plumes inside the storage medium. The lateral outflow of the plume at the opposite horizontal boundary gives rise to a filling box type flow. For optimizing the storage capacity based on the PCM capsule properties, the dimension of the storage medium and the design of the heat exchanger, it may be helpful to adapt the findings of this thesis. For example, the mass flow rate of charge fluid inside the heat exchanger can be fixed by setting the pump speed to value optimized for maximal storage efficiency given a particular maximum allowable time for melting/solidifying the PCM.

1.2.5 Confined porous enclosures

With the advancements in electronics (Alhashash *et al.*, 2013), nano-technologies (Oztop *et al.*, 2015) etc., there occur several cases when heating of components happens in a confined space. Bubnovich & Toledo (2007) explain that by filling the confined space with porous materials supplemental cooling can be achieved, provided that the thermal conductivity of the porous material is greater than that of the saturated fluid. Expanding upon this idea, Saleh & Hashim (2013), Mansour *et al.* (2013), Siddiki *et al.* (2015) and others numerically investigated the heating or cooling that occurs because of natural convection from a localized source in confined enclosures filled with porous materials. One of the primary objectives of their studies was to optimize the volume and other physical parameters of the enclosure, e.g. the porosity, against the size of the heating dissipating component. We find that the flow behavior observed is similar to a filling box type, and hence our current analytical models can be used in guiding the optimization process.

1.3 Present contribution and thesis organization

In spite of the manifold possible applications of this research, this is, at its core, a thesis devoted to an improved fundamental understanding of the flow depicted schematically in figure 1.1. The objectives of this thesis are threefold: (i) to derive similarity solutions for porous media plumes in a Darcy regime with Péclet number $Pe \gg \mathcal{O}(1)$ for both the line and point source geometries, (ii) to estimate the filling box time, and therefore the maximum amount of source fluid that can be injected into a confined porous medium as a function of the source and reservoir parameters and (iii) to study the effect of sudden permeability changes vis-à-vis flow behaviors and filling box times.

As discussed in §1.1, while plume solutions are available in the literature for a large range of Péclet numbers in a non-Darcy regime, in the Darcy regime the solution has been derived only for $Pe \lesssim \mathcal{O}(1)$. However, the cases of laminar plumes with $Pe \gtrsim \mathcal{O}(1)$ are not unrealistic and therefore cannot be overlooked.

The present gap of scientific understanding motivates us to derive a new solution for Darcy plumes in the $Pe \gg \mathcal{O}(1)$ regime. As we shall see, this new solution represents an improvement of sorts over one of the key formulas derived by Wooding (1963), namely that given by (1.5). According to this result, the plume volume flux is predicted to be independent of the fluid viscosity, the permeability and even the source buoyancy flux. As we shall see, these surprisingly omissions do not apply as Pe is increased.

The second important contribution and the main objective of this thesis is to outline an experimentally corroborated analytical model of filling box flows in porous media. Although filling box flows have been studied in great detail in free media with turbulent plumes, to our best knowledge, no analogue study has yet been performed in the porous medium case. We first derive analytical solutions for all three flow regimes, i.e. the plumes, gravity currents and first fronts, and couple these to make a filling box model. The analytical solutions of this filling box model give an estimation of the filling box time, i.e. the time required by the first front to reach the source elevation as a function of the source and reservoir parameters. This filling box time indirectly also yields the amount of source fluid that can be injected up to the point of overflow. Furthermore, we also present an analysis that explains how this filling box time and the amount of source fluid injected can be optimized or maximized by altering the source parameters for fixed reservoir conditions. Finally, the analytical predictions are supported by similitude laboratory experiments.

In the third part of our research, considering the real geophysical scenarios where the porosity and permeability may be nonuniform, we relax the requirement of medium uniformity. We thus investigate the effects of a sudden permeability change on the plume and its outflow. While there is significant literature on plumes in uniform media, the precise effect of sudden changes in permeability has not yet been studied in the filling box context. In case of a gravity current in a two-layer medium, the majority of studies are analytical and numerical in nature (Ungarish & Huppert, 2000; Pritchard *et al.*, 2001; Goda & Sato, 2011). As a consequence, there is a need to develop a comprehensive experimental data

Table 1.1: Scientific contribution arising from the present thesis. Here CANCAM and ISSF stand for the Canadian Congress of Applied Mechanics and International Symposium on Stratified Flows, respectively.

Chapter	Journal/Conference proceeding	Status	Co-author(s)
2	<i>J. Fluid Mech.</i>	Published	M. R. Flynn
2	<i>Proc. 25th CANCAM</i>	Published	M. R. Flynn
2	<i>Proc. 8th ISSF</i>	Submitted	M. R. Flynn, M. A. Roes, D. Bolster
3	<i>Transp. Porous Med.</i>	Published	M. R. Flynn
4	<i>J. Fluid Mech.</i>	Submitted	M. R. Flynn

set that can be used to validate the predictions of related numerical models.

Considering my contributions to the scientific community, parts of this thesis work have appeared or have been submitted to appear in a total three journal publications and two conference proceedings (see Table 1.1). Chapter 2 of the thesis has already appeared in the Journal of Fluid Mechanics (Sahu & Flynn, 2015), whereas Chapter 3 has been published in Transport in Porous Media (Sahu & Flynn, 2016*b*). Moreover, Chapter 4 of the thesis has been submitted to Journal of Fluid Mechanics for a possible publication (Sahu & Flynn, 2016*a*). My work has also been presented at several symposiums and conferences – details can be found in Table 1.2.

The rest of the thesis is organized as follows: Chapter 2 presents the analytical solution along with the experimental methods for filling box flows in a rectilinear geometry. It also compares model predictions with the measurements made in laboratory experiments. Chapter 3 then discusses the theoretical modeling of filling box flows in an axisymmetric geometry with a point source. In Chapter 4, theoretical and experimental investigations of filling box flows in nonuniform porous medium are presented. Finally in Section 5 the conclusions of this thesis work are presented and topics for future study are identified and discussed.

Table 1.2: List of scientific meetings where parts of this thesis work have been presented by the author. Abbreviations are as follows: CAIMS: Canadian Applied Industrial and Mathematical Society, SCS: Subsurface Carbon Storage, CANCAM: Canadian Congress of Applied Mechanics, IGR: Institute of Geophysical Research. Moreover, Interpore is an annual conference organized by the International Society of Porous Media.

Chapter(s)	Conference/Symposium	Location	Month and Year
2	21 st CAIMS Meeting	Saskatoon, SK	Jun. 2014
2	SCS Symposium	University of Calgary	Oct. 2014
2	25 th CANCAM	London, ON	Jun. 2015
2, 4	8 th Interpore	Cincinnati, OH, USA	May 2016
2, 3	23 rd CAIMS Meeting	Edmonton, AB	Jun. 2016
2, 3, 4	IGR Symposia	University of Alberta	Oct. 2013, Oct. 2014, Oct. 2015, Apr. 2016

Chapter 2

Filling box flows in a rectilinear geometry

2.1 Abstract

We report upon a theoretical and experimental investigation of a porous medium “filling box” flow by specifically examining the details of the laminar, descending plume and its outflow in a control volume having an impermeable bottom boundary and sidewalls. The plume outflow is initially comprised of a pair of oppositely-directed gravity currents. The gravity currents propagate horizontally until they reach the lateral sidewalls at $y = \pm L$. The flow then becomes of filling box type, with a vertically ascending “first front” separating discharged plume fluid below from ambient fluid above. The flow details are described analytically by first deriving a new similarity solution for Darcy plumes with $Pe > \mathcal{O}(1)$ where Pe is the Péclet number. From the similarity solution so obtained we then derive expressions for the plume volume flux and mean reduced gravity as functions of the vertical distance from the source. Regarding the plume outflow, a similarity solution adopted from Huppert & Woods (*J. Fluid Mech.*, vol. 292, 55–69, 1995) describes the height and front speed of the gravity currents, whereas a semi-implicit finite difference scheme is used to predict the first front elevation versus time and horizontal distance. As with high-Reynolds number filling box flows, that studied here is an example of a coupled problem: the gravity current source conditions are prescribed by the plume volume flux and mean reduced gravity. Conversely, discharged plume fluid may be re-entrained into the plume,

be it soon or long after reaching the bottom impermeable boundary.

To corroborate our model predictions, analogue laboratory experiments are performed with fresh water and salt water as the working fluids. Our experiments consider as independent variables the porous medium bead diameter and the plume source volume flux and reduced gravity. Predictions for the gravity current front position and height compare favourably against analogue measured data. Good agreement is likewise noted when considering either the mean elevation or the profile of the first front.

Results from this study may be adopted in modelling geological plumes. For example, our equations can be used to predict the time required for discharged plume fluid to return to the point of injection in the case of aquifers closed on the sides and below by impermeable boundaries.

2.2 Introduction

The behaviour of free plumes has been well studied since the development of the MTT equations (Morton *et al.*, 1956). These describe the dynamics of a turbulent plume in an infinite stratified or unstratified ambient, and require the application of an empirically-determined entrainment coefficient to prescribe lateral inflow by turbulent engulfment. By adopting the MTT equations, the behaviour of a free plume in a closed control volume was studied by Baines & Turner (1969). The associated “filling box” model has fluid from the (descending) plume spreading laterally upon reaching the bottom of the control volume then forming an ever deepening layer. The top surface of this layer is referred to as the “first front”; it approaches the plume source asymptotically for large time, t , so that $h_f \propto t^{2/3}$, where h_f is the first front elevation. The inner solution of the filling box flow describes the vertical variation of the plume volume, momentum and buoyancy fluxes. Conversely the outer solution predicts, among other quantities, the first front advection speed. In Baines & Turner’s treatment, the horizontal motion of the discharged plume fluid was omitted, however, this flow was included in the form of a gravity current by later researchers e.g. Britter (1979), Manins (1979)

and Kaye & Hunt (2007).

Whereas a voluminous literature has accumulated on the above convection problem and its application to mixing in chemical storage tanks (Germeles, 1975), the built environment (Caulfield & Woods, 2002; Nabi & Flynn, 2013) and ocean basins (Manins, 1979; Hughes & Griffiths, 2006), comparatively less work has been conducted to understand plumes and filling box flows in porous media. However, this latter problem is very much deserving of attention because, here again, numerous industrial and environmental applications arise. For instance: (i) geological sequestration of supercritical CO₂ (sc-CO₂) into deep saline aquifers for purposes of isolating anthropogenic CO₂ (Baines & Worden, 2004; Bickle *et al.*, 2007). When brine becomes saturated with dissolved sc-CO₂ in the upper layer of aquifers, its density becomes larger than the unsaturated brine. There follows the appearance of negatively-buoyant plumes that result in convective dissolution of this dense sc-CO₂-brine mixture into the unsaturated brine below (Ennis-King & Paterson, 2003). Thus in evaluating the long-term efficacy of carbon sequestration, convective dissolution of the injected sc-CO₂ into brine must be considered and this, in turn, requires an understanding of porous media plumes and their mixing with ambient fluid (Neufeld *et al.*, 2010; MacMinn *et al.*, 2012). Moreover, because of the finite horizontal and vertical extent of aquifers, such plumes must be often studied in the context of filling-box-type flows. (ii) dissolution of non-aqueous phase liquids (NAPL) in the subsurface environment (Khachikian & Harmon, 2000; Kueper *et al.*, 2003). NAPL seepage through the vadose zone and into zones containing groundwater is primarily driven by density differences between the NAPL and groundwater. Because the zones in question may have restricted boundaries, filling box models should again be deployed in quantifying rates of mixing and contamination. Seeking to address some of the flow behaviours specific to these applications, the recent study of Roes *et al.* (2014) considered a filling box flow in a “leaky” porous medium, i.e. one having one or more discrete fissures, which allow for an outflow of discharged plume fluid. Steady state is achieved once this outflow equals the plume volume flux at the level of the (flat, stationary) first front. Note, however, that Roes *et al.*

(2014) did not examine the transient approach towards steady state nor the case of a reservoir sealed by caprock boundaries devoid of fissures for which no steady state solutions exist. Further aspects of Roes et al.’s study are considered below.

Flows in porous media can be divided into the two following categories depending on the value of the Reynolds number, $\text{Re} = \frac{d_0 U}{\nu}$, where d_0 is the mean grain diameter, U is a characteristic velocity that depends upon transport velocity, which we will define in section 2.3.1, and ν is the kinematic viscosity: (i) Darcy flow where $\text{Re} \lesssim \mathcal{O}(10)$, and (ii) non-Darcy flow where $\text{Re} > \mathcal{O}(10)$ (Bear, 1972; Dullien, 1992). A second, equally important non-dimensional number in (variable-component, miscible) porous media flow, is the Péclet number, $\text{Pe} = \frac{d_0 U \tau}{D_d}$, in which D_d is the molecular diffusion coefficient and $\tau (> 1)$ is the tortuosity constant, which is defined as the ratio of the actual path length traveled by a solute molecule to the distance it would travel in the absence of a porous medium. The Péclet number characterizes the importance of advection vs. diffusion with diffusive transport playing a subordinate role to mechanical dispersive transport when $\text{Pe} \gg \mathcal{O}(1)$. The combined influence of diffusion and dispersion can be modelled by defining the following transport coefficient:

$$D = d_0 U \left(1 + \frac{1}{\text{Pe}} \right) \quad (2.1)$$

(Delgado, 2007; Houseworth, 1984). When $\text{Pe} \ll \mathcal{O}(1)$, $D \simeq \frac{D_d}{\tau}$, however, when $\text{Pe} \gg \mathcal{O}(1)$, $D \simeq d_0 U$. In this latter limit, it is appropriate to refer to D as the dispersion coefficient.

The dynamics of rectilinear line plumes in porous media were first studied by Wooding (1963) for Darcy flow with $\text{Pe} \ll \mathcal{O}(1)$. Starting from mass continuity, Darcy’s law and a solute transport equation, Wooding (1963) derived a similarity solution based on the assumption that the plume is long and thin. On this basis, he obtained the following equation for the variation of the plume volume flux, Q , with the vertical coordinate, x :

$$Q = \left(\frac{36 D \phi F_0 k \Lambda^2 x}{\nu} \right)^{1/3}. \quad (2.2)$$

Here ϕ is the porosity, F_0 is the source buoyancy flux, k is the permeability and Λ is the source width in the third dimension.

Roes *et al.* (2014) adopted Wooding’s equations into the $Pe \gg \mathcal{O}(1)$ filling box framework, but could only do so by making a limiting assumption on D , namely that its numerical value was the same everywhere inside the porous medium. Although there exists some practical justification for this approach, this assumption is, strictly speaking incorrect: D depends upon the flow speed and the flow speed, in turn, varies both horizontally and vertically. In fact, Lai (1991) considered the case of spatially-variable D . However, Lai’s analysis was complicated by the fact that, as with the earlier investigation by Chen & Ho (1986), he assumed a non-Darcy flow regime. Thus the Darcy equations were replaced by the Darcy-Forchheimer equations, which are obtained by introducing Dupuit-Forchheimer inertial terms into the Darcy equations (Nield & Kuznetsov, 2013). These inertial terms are proportional to the square of the transport velocity and also include a drag coefficient whose value depends on the geometry of the porous media. In these studies of non-Darcy plumes, it was proved that no similarity solution exists, and hence solutions were instead presented in terms of a non-similar variable, whose magnitude depended on various physical parameters e.g. the permeability and fluid viscosity.

Here we synthesize these previous approaches by assuming Darcy flow with a spatially-variable D . Our objectives are two-fold: (i) to derive self-similar plume equations in a rectilinear geometry germane to this case and, (ii) to use the associated solutions to examine the time-dependent behaviour of porous media filling box flows, from which various pertinent flow time-scales can be estimated. Importantly, our analysis includes a description of the gravity current dynamics associated with plume outflow along the impermeable bottom boundary. As noted above, these dynamics are sometimes omitted when studying turbulent free plumes. The theory is validated (where possible) by comparison with analogue laboratory experiments that employ salt water and fresh water, respectively, as the source and ambient fluids.

The rest of the manuscript is organized as follows. Our plume solution is given

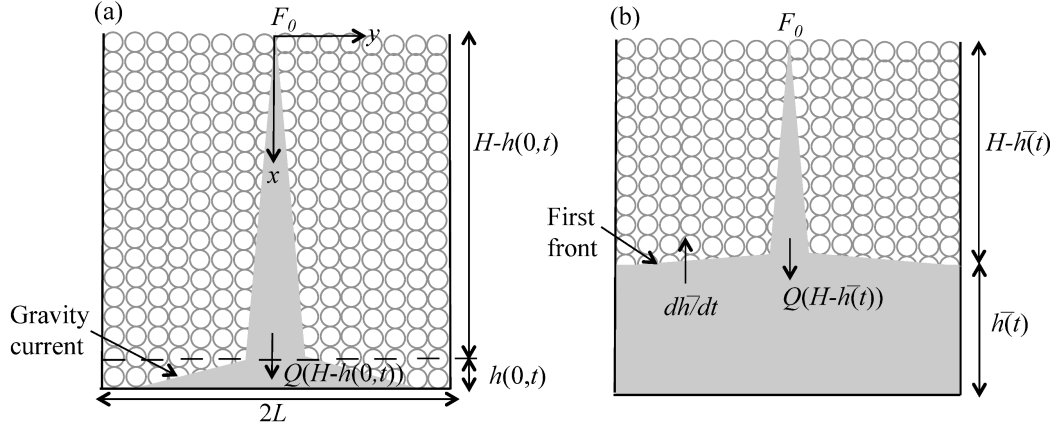


Figure 2.1: Convection in a confined porous medium: (a) plume and gravity current flow, (b) advection of the first front towards the source.

in section 2.3.1 whereas sections 2.3.2 and 2.3.3 describe, respectively, the gravity current and the ascending first front. Thereafter in section 2.4, the laboratory experiments are discussed. This description is followed by a comparison between theory and experiment which appears in section 2.5. Finally section 2.6 presents conclusions of this work and identifies topics for future study.

2.3 Theory

2.3.1 Plume in an unbounded medium

To derive a solution for laminar plume flow in a porous medium, we begin by presenting the governing equations based on mass and momentum continuity, solute transport and a linear equation of state. In contrast to Wooding (1963) and Roes *et al.* (2014), we consider a dispersion coefficient that varies in x and y , where the x and y directions are defined in figure 2.1.

The flow is assumed to be steady, Boussinesq and two dimensional-rectilinear and the ambient is assumed to remain unstratified above the first front so that

the governing equations read

$$\frac{\partial u}{\partial x} + \frac{\partial v}{\partial y} = 0, \quad (2.3)$$

$$\frac{1}{\rho_0} \frac{\partial P}{\partial x} + \frac{\nu}{k} u = \frac{g\rho}{\rho_0}, \quad (2.4)$$

$$\frac{1}{\rho_0} \frac{\partial P}{\partial y} + \frac{\nu}{k} v = 0, \quad (2.5)$$

$$\frac{1}{\phi} \left(u \frac{\partial C}{\partial x} + v \frac{\partial C}{\partial y} \right) = \frac{\partial}{\partial x} \left(D_L \frac{\partial C}{\partial x} \right) + \frac{\partial}{\partial y} \left(D_T \frac{\partial C}{\partial y} \right), \quad (2.6)$$

$$\rho = \rho_0(1 + \beta C). \quad (2.7)$$

The above equations represent, in sequence, the mass continuity, the momentum continuities in x and y directions, the solute transport and the linear equation of state. Here P is the fluid pressure, C is the solute concentration and β is the solute contraction coefficient. Moreover, ρ is the fluid density, whose far-field value is ρ_0 corresponding to a solute concentration of zero. Furthermore, D_L and D_T are the longitudinal and transverse dispersion coefficients.

The momentum equations, (2.4) and (2.5), are combined to eliminate the fluid pressure, whereby

$$\frac{\nu}{k} \left(\frac{\partial u}{\partial y} - \frac{\partial v}{\partial x} \right) = \frac{g}{\rho_0} \frac{\partial \rho}{\partial y}. \quad (2.8)$$

We then apply Wooding's boundary layer approximation so that

$$\left| \frac{\partial v}{\partial x} \right| \ll \left| \frac{\partial u}{\partial y} \right| \quad \text{and} \quad \left| \frac{\partial}{\partial x} \left(D_L \frac{\partial C}{\partial x} \right) \right| \ll \left| \frac{\partial}{\partial y} \left(D_T \frac{\partial C}{\partial y} \right) \right|. \quad (2.9)$$

The validity of the latter boundary layer approximation is outlined at the end of section 2.3.1.

Following Delgado (2007), Houseworth (1984) and others, for $Pe \gg \mathcal{O}(1)$, the transverse dispersion coefficient can be expressed as

$$D_T \simeq \alpha u. \quad (2.10)$$

Here α is the transverse dispersivity, and its value shall, consistent with the turbulent plume entrainment coefficient (Morton *et al.*, 1956), be determined based on experimental measurement. α is typically on the order of pore space length-scale, thus it tends to vary with the size of grains in a porous medium. The

above representation for D_T , in particular the use of u rather than the horizontal transport velocity, v , and the incorporation of α follows from the methodology of Lai (1991). Finally, and for $Pe \gg \mathcal{O}(1)$, we can now make a connection between u and the characteristic velocity, U , that appears in (2.1), i.e $U = \frac{\alpha u}{d_0}$.

On the basis of the above discussion, (2.6) becomes

$$u \frac{\partial C}{\partial x} + v \frac{\partial C}{\partial y} = \alpha \phi \frac{\partial}{\partial y} \left(u \frac{\partial C}{\partial y} \right). \quad (2.11)$$

Furthermore, a stream-function, ψ , is introduced such that $u = \frac{\partial \psi}{\partial y}$ and $v = -\frac{\partial \psi}{\partial x}$. Equations (2.8) and (2.11) can then be rewritten as

$$\frac{\partial^2 \psi}{\partial y^2} = \frac{g\beta k}{\nu} \frac{\partial C}{\partial y} \quad (2.12)$$

$$\frac{\partial \psi}{\partial y} \frac{\partial C}{\partial x} - \frac{\partial \psi}{\partial x} \frac{\partial C}{\partial y} = \alpha \phi \left(\frac{\partial^2 \psi}{\partial y^2} \frac{\partial C}{\partial y} + \frac{\partial \psi}{\partial y} \frac{\partial^2 C}{\partial y^2} \right), \quad (2.13)$$

respectively. We seek a self-similar solution to (2.12) and (2.13) of the form

$$\psi = A_1 x^p \mathcal{F}(\eta), \quad C = A_2 x^q \mathcal{G}(\eta) \quad (2.14)$$

where the self-similar variable, η , is defined as $\eta = A_3 \frac{y}{x^n}$. The constants, p , q , n , A_1 , A_2 and A_3 , will be determined shortly. Applying (2.14) in (2.12) yields

$$A_1 x^p \mathcal{F}'' \left(\frac{A_3}{x^n} \right)^2 = \frac{g\beta k}{\nu} A_2 x^q \mathcal{G}' \frac{A_3}{x^n}. \quad (2.15)$$

Thus, $\mathcal{G}(\eta) = \mathcal{F}'(\eta) \equiv d\mathcal{F}/d\eta$, $n = p - q$ and $A_2 = A_1 A_3 \frac{\nu}{g\beta k}$. Hence, (2.13) becomes

$$x^{2q-1} \{ [q\mathcal{F}' - (p-q)\mathcal{F}''\eta] \mathcal{F}' - [p\mathcal{F} - (p-q)\mathcal{F}'\eta] \mathcal{F}'' \} = \alpha \phi A_3^2 x^{2(2q-p)} (\mathcal{F}'' \mathcal{F}'' + \mathcal{F}''' \mathcal{F}'). \quad (2.16)$$

For a possible self-similar solution, we need to get rid of all constants from the above equation so that its final form contains a single independent variable, namely η . In that spirit, the factors of x that appear on the left- and right-hand sides of the equation disappear provided $p - q = \frac{1}{2}$. Equation (2.16) is further simplified by selecting $A_3 = \frac{1}{\sqrt{\alpha \phi}}$ whereupon

$$\mathcal{F}''' \mathcal{F}' + \mathcal{F}'' \mathcal{F}'' + p \mathcal{F}'' \mathcal{F} - q \mathcal{F}' \mathcal{F}' = 0. \quad (2.17)$$

To determine the values for p and q , we recall that the buoyancy flux, F_0 , is conserved i.e. it is independent of the vertical coordinate in an unstratified medium. Formally, F_0 is defined as

$$F_0 = \Lambda \int_{-\infty}^{\infty} u g' dy,$$

where $g' = g \frac{\rho - \rho_0}{\rho_0} \equiv g\beta C$ is the reduced gravity. By applying the above results, it can be shown that

$$F_0 = \Lambda g \beta A_1 A_2 x^{(p+q)} \int_{-\infty}^{\infty} \mathcal{F}'^2 d\eta, \quad (2.18)$$

which implies that $p + q = 0$. But we previously showed that $p - q = \frac{1}{2}$ and therefore $p = \frac{1}{4}$ and $q = -\frac{1}{4}$. Consequently, (2.17) takes the form

$$\mathcal{F}''' \mathcal{F}' + \mathcal{F}'' \mathcal{F}'' + \frac{1}{4} \mathcal{F}'' \mathcal{F} + \frac{1}{4} \mathcal{F}' \mathcal{F}' = (\mathcal{F}'' \mathcal{F}')' + \frac{1}{4} (\mathcal{F}' \mathcal{F})' = 0. \quad (2.19)$$

In solving (2.19), we recall the assumption that $D \simeq d_0 \bar{U}$ i.e. $Pe \gg \mathcal{O}(1)$. In the neighbourhood of the plume center-line, this is a reasonable approximation, however, its validity is highly suspect far away from the center-line where flow velocities become small. We therefore restrict ourselves to finding an ‘‘inner’’ solution to (2.15), valid in the limit of small y (small η). In the outer region, by contrast, spatial variations in u , v or S are ignored. Such a division of the flow into inner and outer regions would be inappropriate in case of constant D (Wooding, 1963; Roes *et al.*, 2014), but is, in fact, not at all dissimilar to the approach followed in the ‘‘top hat’’ description of free turbulent plumes where molecular diffusive effects are likewise ignored (Morton *et al.*, 1956; Linden *et al.*, 1990). We therefore proceed by integrating (2.19) remembering that $\mathcal{F}'(\eta) = \mathcal{G}(\eta)$ prescribes the non-dimensional solute concentration. This concentration cannot be negative and must vanish altogether in the far field; symbolically, $C(x, y) > 0 \Rightarrow \mathcal{F}'(\eta) > 0$ and $C(x, \pm\infty) = C_0 \Rightarrow \mathcal{F}'(\pm\infty) = 0$. Symmetry suggests, moreover, that the concentration must be identical left and right so that $C(x, y) = C(x, -y) \Rightarrow \mathcal{F}'(\eta) = \mathcal{F}'(-\eta)$. Symmetry also requires that $\psi(x, 0) = 0$ so that $\mathcal{F}(0) = 0$.

Therefore it can be shown that

$$\mathcal{F} = \begin{cases} -c, & \eta < -\pi \\ c \sin \frac{\eta}{2}, & -\pi < \eta < \pi \\ c, & \eta > \pi \end{cases} \quad \text{and} \quad \mathcal{G} = \begin{cases} \frac{c}{2} \cos \frac{\eta}{2}, & -\pi < \eta < \pi \\ 0, & |\eta| > \pi \end{cases}. \quad (2.20)$$

Here c is a constant of integration and will automatically disappear shortly. Note that (2.20) is the only symmetric, nontrivial solution to (2.19) satisfying $\mathcal{G} = \mathcal{F}' \geq 0$. Now on applying (2.18), and recalling that $A_2 = A_1 A_3 \frac{\nu}{g\beta k}$, we find

$$A_1 = \left(\frac{F_0 k}{\Lambda \nu} \frac{\sqrt{\alpha \phi}}{\int_{-\infty}^{\infty} \mathcal{F}'^2 d\eta} \right)^{1/2}.$$

Equation (2.20) can then be combined with (2.14) to determine the volume flux, Q , of the plume. More specifically,

$$Q = \Lambda \int_{-\infty}^{\infty} u dy = \left[\left(\frac{16 F_0 k \Lambda}{\pi \nu} \right)^2 \phi \alpha x \right]^{1/4}. \quad (2.21)$$

Similarly, the plume momentum flux and mean reduced gravity are found to be, respectively,

$$M = \frac{F_0 k}{\nu} \quad \text{and} \quad \bar{g}' = \frac{F_0}{Q} = \left[\left(\frac{\pi F_0 \nu}{16 k \Lambda} \right)^2 \frac{1}{\phi \alpha x} \right]^{1/4}. \quad (2.22)$$

Note that Q and \bar{g}' are proportional to $x^{1/4}$ and $x^{-1/4}$, respectively, whereas in previous investigations such as Wooding (1963) and Roes *et al.* (2014) where $\text{Pe} \lesssim \mathcal{O}(1)$, these quantities are proportional to $x^{1/3}$ and $x^{-1/3}$. The formula for M is unchanged, however, because our plumes plus those of Wooding (1963) satisfy the conditions for Darcy flow.

Equation (2.21) is derived in the limit of an ideal plume whereby $Q \rightarrow 0$ as $x \rightarrow 0$. However, for a nonideal plume, which has a finite source volume flux, this assumption cannot be applied. Therefore, a virtual origin correction is determined by extrapolating the flow to negative x -values and a fictitious point, $x = -x_0$, where the plume volume flux vanishes (Wooding 1963; see also Hunt & Kaye 2001). More formally, x_0 is given by

$$x_0 = \frac{1}{\phi \alpha} \left(\frac{\pi \nu}{16 F_0 k \Lambda} \right)^2 Q_0^4 \quad (2.23)$$

so that the plume volume flux and mean reduced gravity are given, respectively, by

$$Q = \left[\left(\frac{16F_0k\Lambda}{\pi\nu} \right)^2 \phi\alpha(x+x_0) \right]^{1/4} \quad (2.24)$$

and

$$\bar{g}' = g\beta\bar{C} = \left[\left(\frac{\pi F_0\nu}{16k\Lambda} \right)^2 \frac{1}{\phi\alpha(x+x_0)} \right]^{1/4}. \quad (2.25)$$

We prefer to think of solute concentration in terms of its influence on buoyancy, thus our preference for using \bar{g}' in place of \bar{C} . But the relationship between the two is, by virtue of the linear equation of state (2.7), very direct, as confirmed by the above equation.

Finally, we verify the validity of the boundary layer approximation made in (2.9) by estimating, using scaling analysis, the range of D_L and D_T for which the stated inequality holds. When (2.9) is valid,

$$\frac{D_L C}{L_x^2} \ll \frac{D_T C}{L_y^2} \quad \text{or} \quad \frac{D_L}{D_T} \ll \left(\frac{L_x}{L_y} \right)^2 \quad (2.26)$$

where L_x and L_y respectively denote characteristic vertical and horizontal length scales associated with the plume. Given the finite size of the control volume shown schematically in figure 2.1, we choose $L_x = H$. Conversely, L_y is defined to be the plume width at $x = H$; following from the self-similar solution obtained in (2.20), it can be shown that $L_y \sim \pi\sqrt{\alpha H}$. Thus (2.26) holds provided

$$\frac{D_L}{D_T} \ll \frac{H}{\pi^2\alpha}. \quad (2.27)$$

Using results from section 2.5, it can be argued that $\frac{1}{\pi^2\alpha} \sim \mathcal{O}(10) \text{ cm}^{-1}$, at least for the experiments of interest here. Moreover, $H \sim \mathcal{O}(10) \text{ cm}$ and therefore, in the present context, $\frac{H}{\pi^2\alpha} \sim \mathcal{O}(10^2)$. By contrast, we expect $\frac{D_L}{D_T}$ to be significantly less: according to Bear & Verruijt (1987), $\frac{D_L}{D_T} \simeq 100$ only for large Péclet numbers, i.e. $Pe \sim \mathcal{O}(10^6)$, roughly three orders of magnitude greater than the values of Pe relevant to our laboratory experiments. We therefore expect (2.27) to be satisfied both experimentally and, equally importantly, in real geophysical

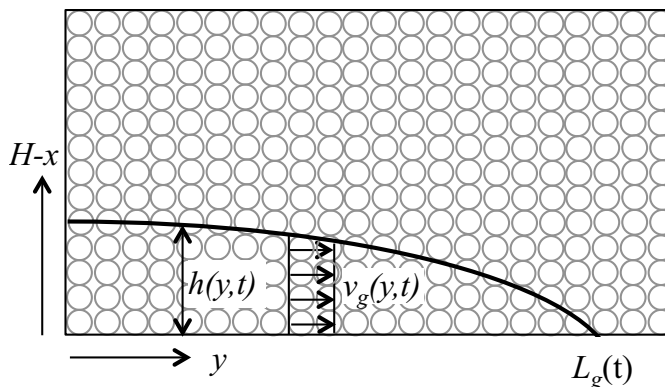


Figure 2.2: Gravity current flow in a porous medium.

flows for which H and α are expected to be larger and smaller, respectively, than the values germane to section 2.4.

It should also be recalled that numerous authors (Guin *et al.*, 1972) recommend application of a dispersion tensor in (2.6) according to which there must appear the additional right-hand side terms $\frac{\partial}{\partial x} \left(D_{xy} \frac{\partial C}{\partial y} \right)$ and $\frac{\partial}{\partial y} \left(D_{yx} \frac{\partial C}{\partial x} \right)$ in which $D_{xy} = D_{yx}$ is the off-diagonal component of the (symmetric) 2×2 dispersion tensor. Using a similar analysis to that described in the previous paragraph, it can likewise be shown that the contribution of these additional terms is small compared to $\frac{\partial}{\partial y} \left(D_T \frac{\partial C}{\partial y} \right)$.

2.3.2 Gravity current

When the plume fluid collides with the (impermeable) bottom boundary of the control volume a pair of gravity currents, traveling in the $+y$ and $-y$ directions, are formed (Manins, 1979; Kaye & Hunt, 2007). Although the flow initiates at the instant that the source nozzle is “switched on”, we take $t = 0$ to be the time when plume fluid first reaches the bottom boundary. We justify this assumption as follows. Using (2.14) and (2.20), it is straightforward to estimate the time, t_R , that a fluid particle resides within the plume whilst flowing a vertical distance H . (The residence time associated with flow within a thermal is expected to be larger than, but still comparable to, the residence time associated with flow

within a plume.) Comparing t_R against the time, t_L , required for the gravity current to reach the lateral sidewalls, we find that $t_R/t_L \sim \mathcal{O}(10^{-1})$ for the geometry of interest here. (The time-scale t_L is defined more precisely below.) In like fashion, $t_R/t_H \sim \mathcal{O}(10^{-2})$ where t_H , defined in section 2.3.3, is the time required for the first front to reach the top of the control volume. By ignoring the flow dynamics within the time interval t_R , we implicitly exclude from considering control volumes that are tall and narrow. However, this case is not representative of many real geophysical scenarios where $L \gg H$ and, in any event, is unlikely to yield well-defined gravity currents of the type investigated below in section 2.3.2.

The propagation of a gravity current through a porous medium has been described by Huppert & Woods (1995) – only a brief review of their formulation is provided below.

Presuming a hydrostatic flow, the gravity current horizontal flow speed, v_g , is depth-independent and varies with $\partial h/\partial y$ where h is the interface height (see figure 2.2) according to

$$v_g = -\frac{kg'_g}{\nu} \frac{\partial h}{\partial y} \quad (2.28)$$

(Huppert & Woods, 1995, equation 2.5). Here g'_g is the reduced gravity of the discharged plume fluid turned gravity current fluid. Strictly speaking, g'_g is a function of t , however, we verify below that the time rate of change of g'_g is small enough to be considered negligible, at least for the problem of interest here.

The equation of local volume flux balance reads

$$\phi \frac{\partial h}{\partial t} = -\frac{\partial}{\partial y} \left[\int_0^{h(y,t)} v_g(y,t) d(H-x) \right]. \quad (2.29)$$

On substituting (2.28) into (2.29), it can easily be shown that

$$\frac{\partial h}{\partial t} - S \frac{\partial}{\partial y} \left(h \frac{\partial h}{\partial y} \right) = 0. \quad (2.30)$$

where $S = \frac{kg'_g}{\nu\phi}$. Also, the boundary condition at the leading edge of the gravity current and the mass conservation equation are given by

$$h(L_g(t), t) = 0 \quad \text{and} \quad \phi \int_0^{L_g(t)} h(y, t) dy = V(t), \quad (2.31)$$

respectively (Huppert & Woods, 1995, equation 3.5). Here V is the total volume of discharged plume fluid turned gravity current fluid measured from the initial instant, when the plume first reaches the bottom surface, up to time t at which point the gravity current is L_g units long.

The methodology presented by Huppert & Woods (1995) is adopted to solve (2.30); thus, we seek a self-similar solution of the form

$$h = \left(\frac{Q_g^2}{S}t\right)^{1/3} \mathcal{H}(\xi) \quad \text{where} \quad \xi = \left(\frac{1}{Q_g S}\right)^{1/3} \frac{y}{t^{2/3}} \quad \text{and} \quad t \neq 0. \quad (2.32)$$

Here Q_g is the volume flux per unit span of the discharged plume fluid turned gravity current fluid. With a similar argument as above for g'_g , we neglect the time dependence of Q_g for which a verification is presented at the end of this section. After some simplification, the PDE (2.30) can be rewritten as the following ODE in ξ :

$$3\mathcal{H}''\mathcal{H}' + 3\mathcal{H}'\mathcal{H}' + 2\xi\mathcal{H}' - \mathcal{H} = 0. \quad (2.33)$$

The associated boundary conditions, which come from (2.31), read

$$\mathcal{H}(\lambda) = 0 \quad \text{and} \quad \phi \int_0^\lambda \mathcal{H} d\xi = 1 \quad (2.34)$$

where λ is the dimensionless length of the gravity current so that $\max(\xi) = \lambda$. A numerical solution is obtained for (2.33) by employing a shooting method to find $\mathcal{H}(\xi = 0)$ and λ . Note that in this equation, ξ is the independent variable of integration, not t . Therefore, we initialize our solver using a ‘‘clever guess’’ for the appropriate condition at $\xi = 0$ and solve the ODE. We then look to see whether the volume conservation equation $\phi \int_0^\lambda \mathcal{H} d\xi = 1$ is satisfied given that $\mathcal{H}(\lambda) = 0$. The ‘‘clever guess’’ is then updated and the process repeated till the solution converges. Numerical values of $\mathcal{H}(\xi = 0)$ and λ are found to be, respectively, 2.470 and 2.046. The solution obtained is then used to predict the gravity current shape as a function of time for which sample results are exhibited in figure 2.3. Because $t = 0$ is outside of the region of interest here, the final solution is plotted only for $t \gg 0$.

It should be noted that the result obtained from the similarity solution is only valid when the gravity current is long and thin, i.e. $h(0, t) \ll L_g(t)$. Here $L_g(t)$

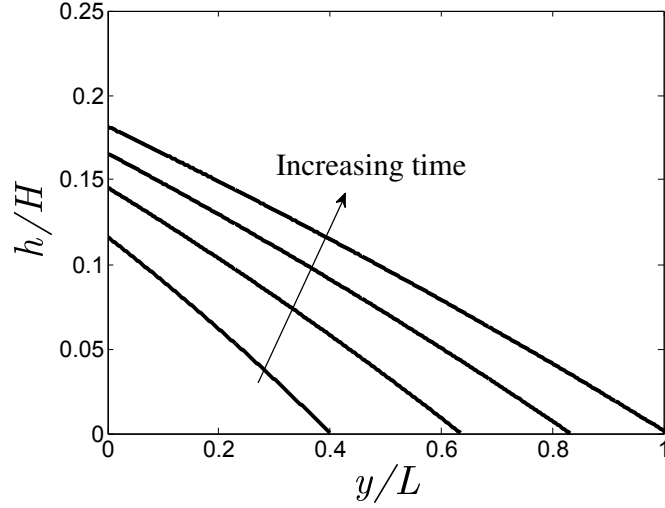


Figure 2.3: Gravity current height and length vs time. The non-dimensional time increment is $0.25t_L$, starting with $t = 0.25t_L$ for the lowest curve and finishing with $t = t_L$ with the gravity current front located at $y/L = 1$. Also, $S = \frac{kg'}{\phi\nu} = 0.6$ cm/s, where $\phi = 0.38$.

is the length of the gravity current and is given as

$$L_g = \lambda(Q_g S)^{1/3} t^{2/3}. \quad (2.35)$$

Furthermore, the time required by the gravity current front to reach the sidewall of the control volume, which is at a horizontal distance L from the source, is

$$t_L = \left[\left(\frac{L}{\lambda} \right)^3 \frac{1}{Q_g S} \right]^{1/2}. \quad (2.36)$$

From (2.35) and (2.36), a straightforward relation between the dimensionless length and time can be derived as

$$\frac{L_g}{L} = \left(\frac{t}{t_L} \right)^{2/3}. \quad (2.37)$$

Note also that when $t = t_L$, the mean height of the gravity current is given by

$$\bar{h}_{t_L} = \frac{1}{L} \int_0^L h(y, t_L) dy = \frac{1}{\lambda} \left(\frac{Q_g^2}{\phi^3 S} t_L \right)^{1/3}. \quad (2.38)$$

This mean height of the gravity current will be used in section 2.5 when comparing the theoretical model with the experimental measurements.

From (2.24) and (2.25) we observe that $Q_g \propto (1 - h/H)^{1/4}$ and $g'_g \propto (1 - h/H)^{-1/4}$, respectively. Furthermore, $h/H \ll 1$ – see figure 2.3. These observations support our assumption that the time rates of change of Q_g and g'_g are negligible. For instance, the change in Q_g and g'_g between the times, $t = 0.25t_L$ and $t = t_L$ for the curves presented in figure 2.3 are -1.59% and 1.59% , respectively, whereas the increase in time is 300% .

2.3.3 First front

After the gravity current reaches the sidewall of the control volume, the dense fluid near the sidewall begins to move primarily vertically. Following the terminology introduced by Baines & Turner (1969), we refer to the interface between the discharged plume fluid and the overlying ambient fluid as the first front. Whereas the first front evolves in time and becomes horizontal in the long-time limit, its initial profile is prescribed by the shape of the gravity current at $t = t_L$. For $t > t_L$, the pressure remains hydrostatic and therefore the horizontal velocity below the first front remains independent of x . Hence, (2.30) can be employed to describe the spatio-temporal evolution of the first front. In this case, however, one must replace the front condition (2.31a) with a no-flux condition at the (impermeable) sidewalls. Symbolically

$$\partial h / \partial y = 0 \quad \text{when} \quad y = \pm L \quad \text{and} \quad t > t_L. \quad (2.39)$$

The second boundary condition is obtained from a straightforward extension of (2.31b), i.e.

$$\phi \int_0^L [h(y, t - t_L) - h(y, t_L)] dy = V(t - t_L). \quad (2.40)$$

The finite length of the box obviously imposes an external length-scale on the problem at hand and, as a consequence, no self-similar solution is possible. However, a numerical solution can be obtained by applying a semi-implicit finite difference scheme (Causon & Mingham, 2010). We rewrite (2.30) in the form

$$\frac{\partial h}{\partial t} = \frac{S}{2} \frac{\partial^2 h^2}{\partial y^2}. \quad (2.41)$$

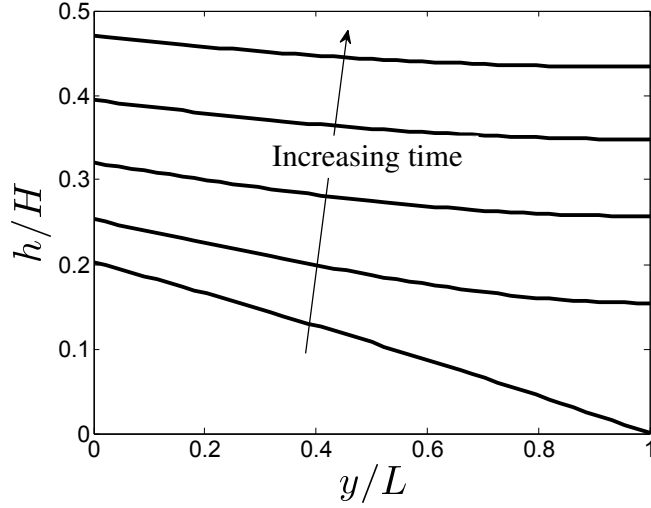


Figure 2.4: Evolution of the first front. The non-dimensional time increment is $0.08t_H$, starting with $t = t_L$ for the lowest curve. Note that t_H is defined by (2.45). The values used for the numerical scheme are: $\frac{\Delta y}{L} = 10^{-3}$, $\frac{\Delta t}{t_H} = 10^{-6}$ and $S = \frac{kg'}{\phi\nu} = 0.6$ cm/s, where $\phi = 0.38$.

The numerical solution is then obtained using the methodology outlined in Appendix C; sample results are given in figure 2.4.

As the first front advects upward, its curvature diminishes in time so that as $t \rightarrow \infty$, the boundary between discharged plume fluid and external ambient fluid becomes horizontal. The vertical advection of the first front can then be determined by simple volume flux balance, i.e.

$$\lim_{t \rightarrow \infty} [\phi A U_f(h)] = \lim_{t \rightarrow \infty} [Q(x = H - h)] \quad (2.42)$$

where Q is defined by (2.24), A is the control volume cross-sectional area, which is assumed to be both constant and much larger than that of the plume, and U_f is the vertical velocity of the (horizontal) first front, which has an elevation of h , i.e. $U_f(h) = \frac{dh}{dt}$. Even before the long time limit is realized, (2.42) can still be applied provided h and U_f are replaced by their y -averaged mean values, i.e.

$$\phi A \bar{U}_f(\bar{h}) = Q(H - \bar{h}) \quad (2.43)$$

where $\bar{U}_f(\bar{h}) = \frac{d\bar{h}}{dt}$. After applying (2.24), and with further integration and simplification, the predicted vertical distance, $\bar{h}_2 - \bar{h}_1$, traveled by the first front

in time $t_2 - t_1$ can be determined from

$$\bar{h}_2 = H + x_0 - \left[(H + x_0 - \bar{h}_1)^{3/4} - \frac{3(t_2 - t_1)}{4A} \left(\frac{16F_0 k \Lambda \alpha^{1/2}}{\pi \nu \phi^{3/2}} \right)^{1/2} \right]^{4/3}. \quad (2.44)$$

By rearranging (2.44) and setting $\bar{h}_2 = H + x_0$ and $\bar{h}_1 = \bar{h}_{t_L}$, we obtain the following characteristic time-scale associated with the ascent of the first-front from the bottom to the top of the control volume:

$$t_H = \frac{4}{3} A \left(\frac{\pi \nu \phi^{3/2}}{16F_0 k \Lambda \alpha^{1/2}} \right)^{1/2} (H + x_0 - \bar{h}_{t_L})^{3/4}. \quad (2.45)$$

Qualitatively, this result is similar to (B3) of Caulfield & Woods (2002), who studied filling box flows for a control volume devoid of porous material and containing a free turbulent plume.

2.4 Laboratory set-up and experiments

Laboratory experiments were performed to verify select theoretical predictions from section 2.3. A transparent acrylic rectangular box 88.9 cm long \times 7.6 cm wide \times 50.8 cm tall was filled with tap water and Potters Industries A Series Premium glass beads. The beads were of uniform size, and had a diameter of either 0.3 cm or 0.5 cm and a density of 1.54 g/cm³ as compared to 0.99 g/cm³ for the tap water. We assume a porosity of $\phi = 0.38$ for randomly distributed spherical beads (Happel & Brenner, 1991).

A schematic of the experimental set-up is shown in the figure 2.5. A specially designed line nozzle, manufactured to minimize the momentum of the source fluid by limiting the discharge velocity (Roes, 2014, Appendix C.3), was used as the source and had a discharge area, $A_{\text{nozzle}} = 2.8 \text{ cm}^2$. For simplicity, the nozzle, which spanned the width of the box, was positioned on-centre at $y = 0$. However, we expect that similar observations would have been recorded had the nozzle been located off-center (but not too close to either sidewall). Also, because the tank was confined from all sides, except the top, the vertical location of the nozzle, and therefore that of the free surface of tap water, was kept roughly 14 cm below the top of the tank. Thus, leaving a fraction of tank volume that

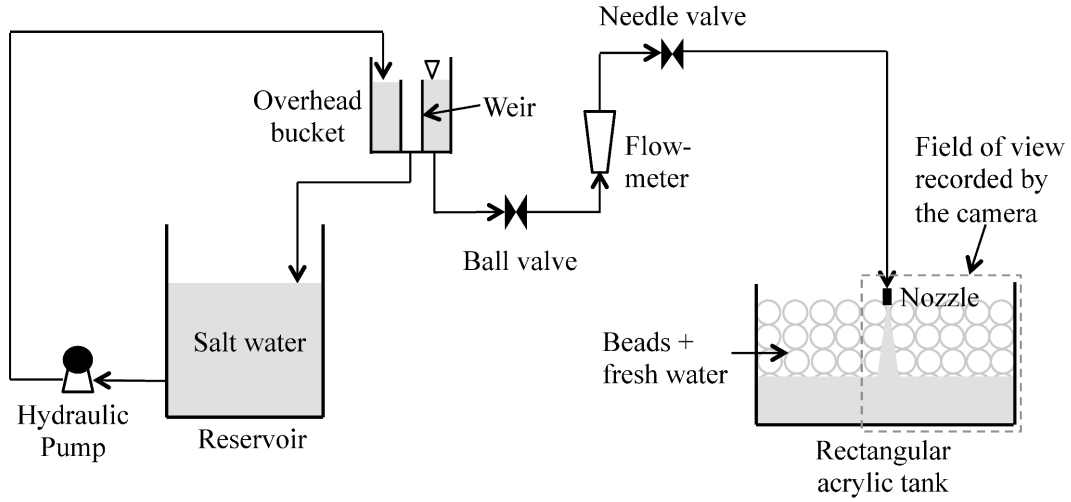


Figure 2.5: Schematic of the experimental set-up.

got filled during the experiments in absence of any outlet. The filling of this volume during experiments, however, did not affect the flow behavior because the flow remains hydrostatic throughout; a changing free surface height would only matter if the free surface elevation varied with y , but that's not the case here. An overhead bucket was used for supplying dense fluid, which consisted of salt water dyed with Procion MX Cold Water dye. Dye was used for flow visualization purposes; its addition did not change the fluid density ($<1.10 \text{ g/cm}^3$) or kinematic viscosity ($0.01 \text{ cm}^2/\text{s}$). The overhead bucket contained a cylindrical internal weir to maintain a constant level. A Gilmont GV-2119-S-P flowmeter was used to measure the (time-invariant) source volume flux which was set with the help of a ball valve and a needle valve. The overhead bucket was, in turn, supplied by a reservoir having a maximum capacity of 100 L. Fluid densities were measured to an accuracy of 0.00005 g/cm^3 using an Anton Paar DMA 4500 density meter.

A Canon Rebel EOS T2i 18.0 PM camera with an 18-55 mm IS II zoom lens was used to capture experimental images, which were collected every 120 s. Thus, over the course a single experiment, which usually took approximately 3 h to complete, roughly 90 images were recorded. The camera was placed perpendicular to the front face of the acrylic tank below which was located a mirror angled at

45° whose purpose was to provide details of the gravity current advance. The tank was backlit using a 3M 1880 overhead projector; to diffuse the light from this projector, a large sheet of white sketching paper was taped to the back of the tank. To minimize parallax effects, and also because of the symmetric nature of the flow, only one-half of the tank was in the field of view of the camera (figure 2.5).

All experimental images, including reference images which were recorded before the start of each experiment, were cropped to remove unwanted regions outside of the flow domain. Cropped images were then converted into gray-scale and the reference image was subtracted to specifically highlight the descending plume, gravity current and ascending first front. Subtracted images were then divided into 20 vertical bands of equal width with bands 3 through 20 falling outside of the near plume region. We used the post-processing algorithm described in Roes (2014) to estimate the interface height of the gravity current or first front in each of bands 3 through 20. Thus in each band and for every time instant, pixels were first binned into 10×10 boxes. Row-averaged pixel intensities were then calculated, which allowed us to compute the elevation corresponding to the maximum vertical intensity gradient. To improve upon this initial estimate for the interface height, data within ± 150 pixels of the previously determined elevation were fit using a high-order polynomial. Our refined estimate of the interface height was based on the vertical location corresponding to the maximum of the derivative of the polynomial. Thus we could measure the variation of the gravity current or first front interface height with y or, by averaging over all 18 bands, compute the mean elevation over the width of the entire right-hand side of the tank.

A list of the experiments performed is shown in Appendix D, table D.1. We regard the bead diameter, d_0 , and the plume source volume flux, Q_0 , and reduced gravity, g'_0 , as independent variables. From these, the following derived variables were computed: the source buoyancy flux, F_0 , Reynolds number, Re_0 , Péclet number, Pe_0 , and the permeability of the porous medium, k . Note that $F_0 = Q_0 g'_0$. Moreover, Re_0 is given by $Re_0 = Q_0 d_0 / (A_{\text{nozzle}} \nu)$. In the ma-

majority of experiments, the source Reynolds number was $\text{Re}_0 \approx \mathcal{O}(10)$. (Note that Re_0 is the maximum value of the Reynolds number, which decreases with increasing x as $\text{Re} \propto (x + x_0)^{-1/4}$). In all cases, the source Péclet number, $\text{Pe}_0 = Q_0 d_0 \tau / (A_{\text{nozzle}} D_d) > 100$, where the molecular diffusion coefficient of the solute, D_d , was estimated using the method suggested by Tyn and Calus – see (11-9.5) of Poling *et al.* (2000) and following Winsauer *et al.* (1952) the tortuosity constant was assumed to be $\tau = 2.0$ for $\phi = 0.38$. Furthermore, the permeability of the porous medium, corresponding to a medium comprised of uniform spherical beads, is calculated based on the empirical relationship derived originally by Rumpf and Gupte, and subsequently applied by Acton *et al.* (2001), Lyle *et al.* (2005) and many others, such that $k = \frac{d_0^2 \phi^{5.5}}{5.6}$.

2.5 Results and discussion

Illustrative experimental images are shown in figure 2.6. The curves on top of the laboratory images show the measured heights of the gravity current and first fronts. Panel a shows the time instant $t = 0$ at which the descending plume, dyed purple, first reaches the impermeable bottom boundary. Thereafter, a rightward propagating gravity current is formed, as exhibited in panel b. Although our equations of section 2.3.2 assume a gravity current of a constant reduced gravity and corresponding gravity current density, we see in this experimental image evidence of a horizontal density gradient within the gravity current. By combining Darcy’s law, a hydrostatic pressure equation and Leibniz’s rule, it can be shown that this density gradient is dynamically insignificant provided

$$\left| (\rho - \rho_0) \frac{\partial h}{\partial y} \right| \gg \left| \int_0^h \frac{\partial \rho}{\partial y} d(H - h) \right|.$$

We assume that $\rho \propto I$, where I is the intensity of the false-colour grayscale laboratory images and note that $I(\rho = \rho_0) = 0$. Therefore the condition to be satisfied becomes:

$$\left| I \frac{\partial h}{\partial y} \right| \gg \left| \int_0^h \frac{\partial I}{\partial y} d(H - h) \right|.$$

A separate analysis, not presented here, confirms that the above inequality is satisfied in our experiments. Thus we conclude that the assumption made in de-

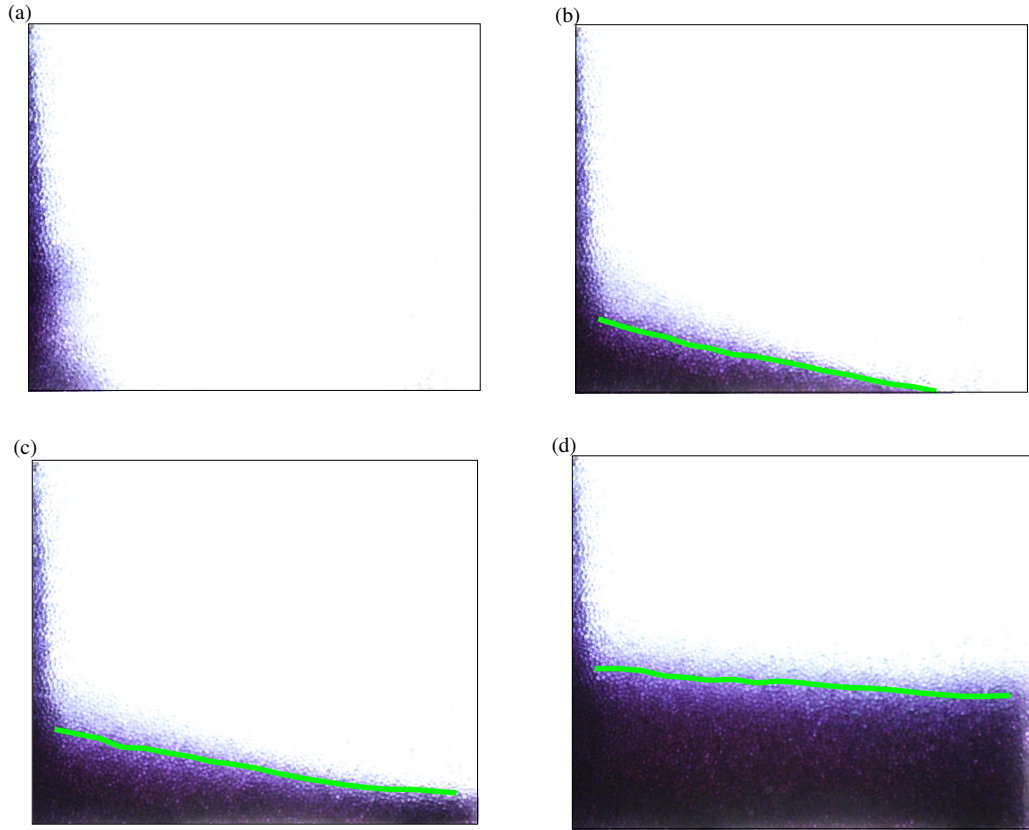


Figure 2.6: [Colour online] Plume, gravity current and curved interface experimental images. Images correspond to Experiment 13 at (a) $t = 0$, (b) $t = 0.7t_L$, (c) $t = t_L + 0.1t_H$ and (d) $t = t_L + 0.3t_H$ where t_L and t_H are defined by (2.36) and (2.45), respectively. The curves shown in (b), (c) and (d) are the interface heights as computed using the Matlab algorithm of section 2.4. The field of view for each image measures 44 cm long \times 36 cm tall.

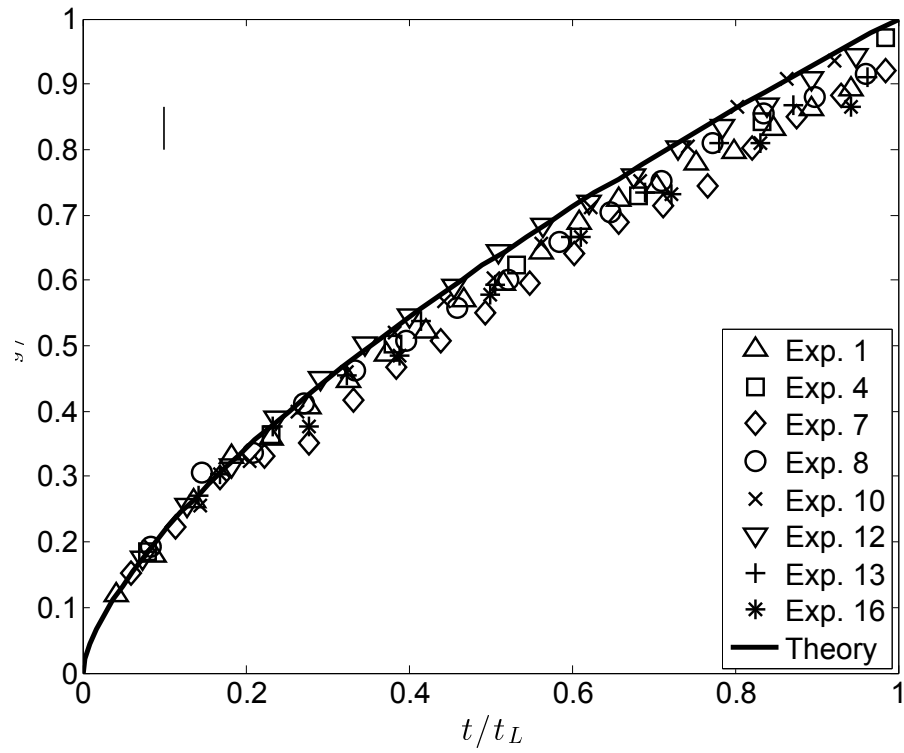


Figure 2.7: Gravity current front position vs. time. A representative error bar is indicated in the upper left hand side corner.

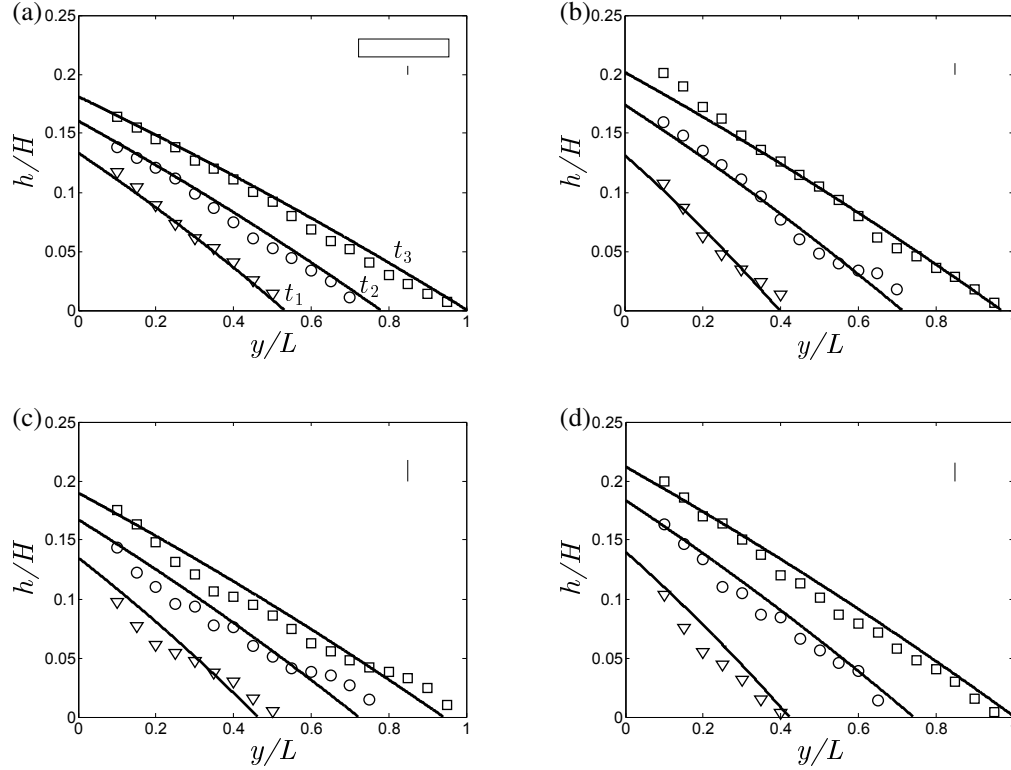


Figure 2.8: Gravity current profile: (a) Experiment 1, $t_1 = 0.37t_L$, $t_2 = 0.67t_L$, $t_3 = 1.0t_L$, (b) Experiment 4, $t_1 = 0.25t_L$, $t_2 = 0.60t_L$, $t_3 = 0.95t_L$, (c) Experiment 10, $t_1 = 0.34t_L$, $t_2 = 0.64t_L$, $t_3 = 0.95t_L$, and (d) Experiment 13, $t_1 = 0.27t_L$, $t_2 = 0.64t_L$, $t_3 = 1.0t_L$. The time scales t_L and t_H are defined by (2.36) and (2.45), respectively. Representative average error bars are indicated in the upper right hand side corner of each figure. Also, a rectangle having unit aspect ratio in physical coordinates is indicated in panel a.

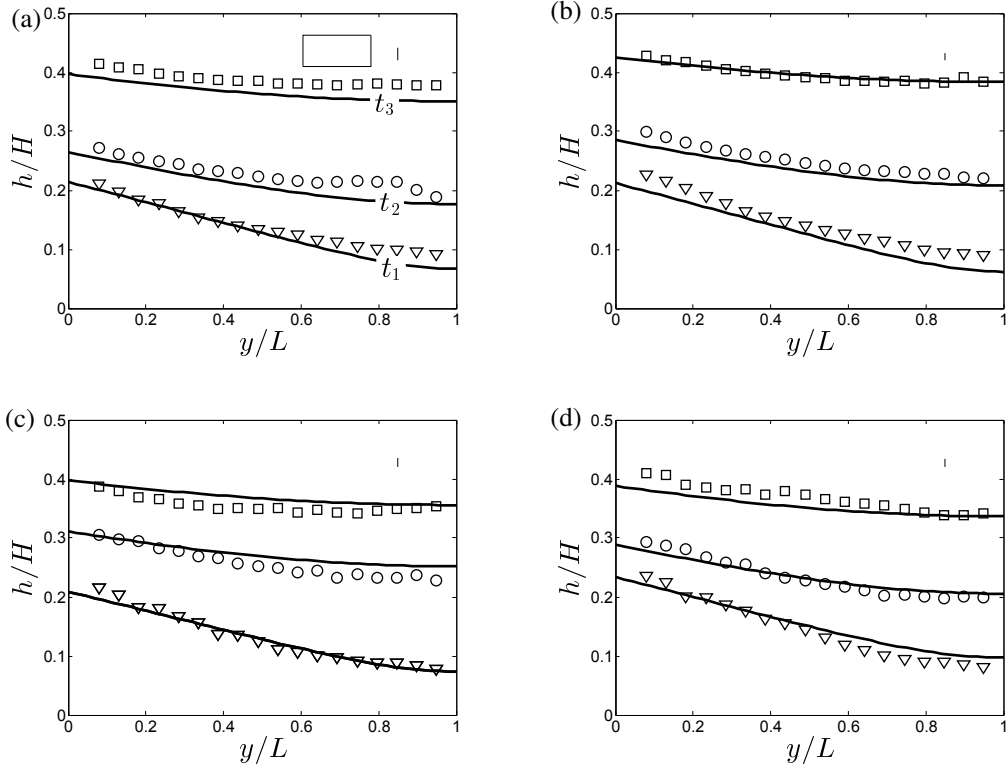


Figure 2.9: Curved interface profile: (a) Experiment 1, $t_1 = t_L + 0.04t_H$, $t_2 = t_L + 0.08t_H$, $t_3 = t_L + 0.13t_H$, (b) Experiment 4, $t_1 = t_L + 0.04t_H$, $t_2 = t_L + 0.08t_H$, $t_3 = t_L + 0.13t_H$, (c) Experiment 10, $t_1 = t_L + 0.03t_H$, $t_2 = t_L + 0.09t_H$, $t_3 = t_L + 0.14t_H$, and (d) Experiment 13, $t_1 = t_L + 0.04t_H$, $t_2 = t_L + 0.07t_H$, $t_3 = t_L + 0.11t_H$. The time scales t_L and t_H are defined by (2.36) and (2.45), respectively. Representative average error bars are indicated in the upper right hand side corner of each figure and a rectangle having unit aspect ratio in physical coordinates is indicated in panel a.

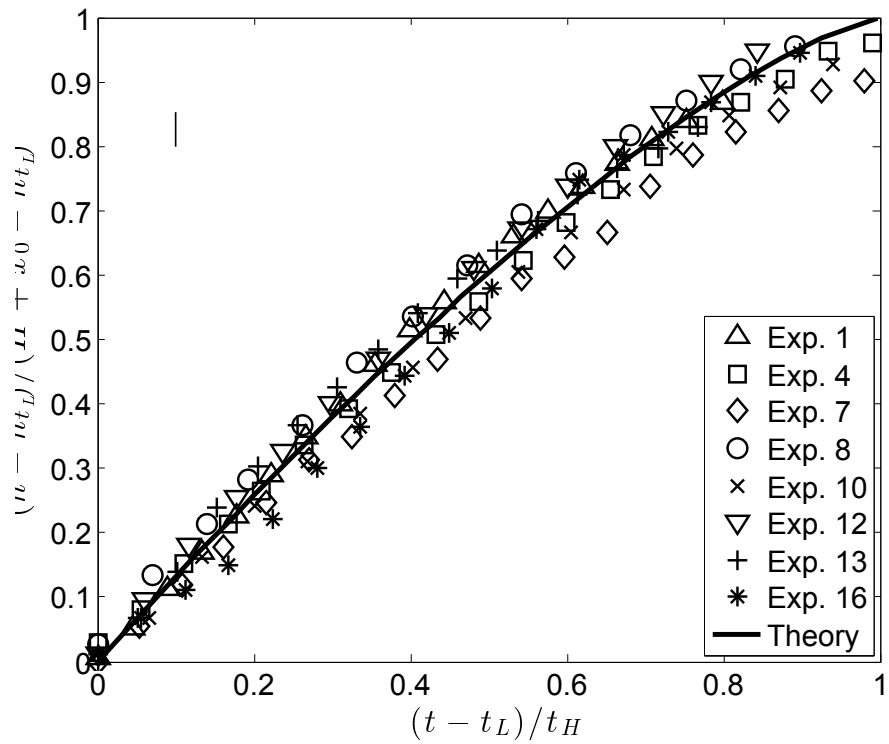


Figure 2.10: First front elevation vs time. A representative error bar is indicated in the upper left hand side corner.

riving (2.28) is appropriate. Finally, panels c and d correspond to times greater than t_L . Discharged plume fluid accumulates in a deepening layer of contaminated fluid at the bottom of the control volume. Qualitatively, the shapes of the gravity current and of the first front are similar to the results displayed in figures 2.3 and 2.4, respectively. However, to make this comparison between the analytical predictions of section 2.3 and the experimental measurements of section 2.4 quantitatively meaningful, it is first necessary to estimate the numerical value of α , which first appears in (2.10) and reappears, for instance, in (2.24) and (2.44). For this purpose, we focus specifically on the long time measurements of the first front elevation. (Note that, following the studies of free turbulent plumes e.g. Baines & Turner 1969, measuring the elevation of the first front is much more straightforward than trying to directly determine the plume volume flux and its variation with x). Using (2.42) as the reference analytical solution, the error-minimizing value of α is determined for each experiment. We then compute the average over all 16 experiments from table D.1 of Appendix D and find a mean value of $\alpha = 0.015$ cm. The mean errors presented in table D.1 have standard and maximum deviations of $\pm 3\%$ and $\pm 5\%$ for the entire data set. Although α may vary with bead sizes, in the current experiments the diameters of the larger and smaller beads are in the same order. Moreover, the small values of deviations reported above support the hypothesis that $\alpha = 0.015$ cm is a meaningful average value.

With this value for α to hand, separate comparisons can be made for the gravity current and first front problems. Starting with the gravity current, two different comparisons between theory and experiment are drawn: (i) the front position vs. time, t (figure 2.7), and (ii) the gravity current profile for various times (figure 2.8). In figure 2.7, the solid curve is adopted from (2.37). For clarity, we do not include the entirety of our experimental data set but rather choose eight representative experiments from table D.1 that span small and large Q_0 , g'_0 and d_0 . Because the plume has a finite thickness when it reaches the bottom of the control volume at $t = 0$ (see figure 2.6 a), the initial gravity current length is some finite value. Therefore measured values for $L_g > 0$ when $t = 0$. To make

a consistent comparison with the predictions of (2.37) for which $L_g = 0$ when $t = 0$, it is therefore necessary to adjust the measured data so that the first data point of each set coincides with the solid curve. The meaningful comparison to be drawn between theory and experiment is therefore for intermediate and large values of t ; in the former case, good agreement is observed whereas in the latter case predicted values for L_g typically over-predict their measured counterparts. This observation is consistent with Huppert & Woods (1995), who, in their investigation of a constant volume release in a Hele-Shaw cell, made similar observations and attributed their discrepancy to the influence of bottom friction near the front (see e.g. their figures 2 and 3). In figure 2.8, we show the gravity current profile at three distinct times for four different experiments. Experiments are chosen on the basis of their values for F_0 and d_0 , being in some instances comparatively small and in others comparatively large. In all cases, the measured heights show good agreement with the profiles predicted from (2.32). The positive comparisons drawn in figures 2.7 and 2.8 constitute an indirect validation for the computed value of α : the influx to the gravity current depends on Q_g and g'_g , which are, in turn, functions of α as prescribed, for instance, by (2.24) and (2.25).

In considering the first front, figure 2.9 compares the measured and predicted first front elevations for the same experiments, 1, 4, 10 and 13, as are considered in figure 2.7. In all cases, and consistent with figure 2.4, it is observed that the first front becomes more horizontal as t increases. Equation (2.40) shows that the elevation, h , of the first front depends upon the total volume, V , of plume fluid discharged into the lower layer up until that particular instant in time. Hence the minor discrepancies observed in figure 2.9 are likely the result of differences in the values of the actual volume flux vs. that estimated from (2.24).

Furthermore, we can estimate the y -averaged first front elevation vs. time by adopting (2.44). Results are shown in figure 2.10, which includes the same set of representative experiments as in figure 2.7. We do not separately show the solution of (C.1) because this curve overlaps with the solid curve already present in figure 2.10. Elevations are non-dimensionalized by $H + x_0 - \bar{h}_{t_L}$ where x_0 is defined by (2.23) and \bar{h}_{t_L} is defined by (2.38). Conversely, the abscissa is

non-dimensionalized by t_H , which is defined by (2.45). The overall comparison between theory and experiment is favourable. In particular, both suggest that the speed of ascent decreases as the first front approaches the source. This behaviour is qualitatively consistent with (2.24) and (2.43), the former of which indicates that the plume volume flux scales as $x^{1/4}$.

We tried rationalizing the variation of the (non-dimensionalized) data by grouping our experimental measurements into different families according to the values of g'_0 , Q_0 or d_0 . For better or worse, this analysis did not reveal any definitive trends other than that the first front elevation is moderately larger for small Q_0 – see figure 2.10. On this basis, we conclude that the non-dimensionalizations outlined above are appropriate in that they capture the leading order physics of the flow.

A video comparing the numerical and experimental height profiles of the gravity current and first front for Experiment 13 is included as Electronic Supplementary Material (Movie.mp4). The video is made in Matlab by first combining 29 images, spaced at 20 s intervals where the horizontal and vertical axes are respectively normalized by L and H . Analogue numerical solutions are then superposed on top of the experimental images where we use the equations of sections 2.3.2 and 2.3.3, respectively, when $t < t_L$ and $t > t_L$.

2.6 Conclusions

Motivated by studies of filling box flows with turbulent free plumes (Baines & Turner, 1969), and based on previous investigations of laminar plumes (Wooding, 1963; Roes *et al.*, 2014) and gravity current flow (Huppert & Woods, 1995) in porous media, a solution for filling box flows in the Darcy regime with $Pe \gg \mathcal{O}(1)$ is derived. We assume a Boussinesq system where the dense and light fluids are fully miscible. The following three flow components are considered: (i) a (negatively-buoyant) laminar plume, (ii) a pair of gravity currents comprised of discharged plume fluid that propagate along the bottom of the control volume and (iii) the subsequent vertical advection of the discharged plume fluid towards

the source.

In section 2.3.1, we derive a similarity solution for laminar plume flow. This solution assumes that molecular diffusion is negligible compared to mechanical dispersion, D , and so applies in the “inner” region close to the plume axis where flow speeds are comparatively large. In the context of (2.1), we assume that $\text{Pe} \gg \mathcal{O}(1)$. The solution is derived by employing a transverse dispersivity constant, α , in the governing equation (2.13) whose value, 0.015 cm, is determined by comparison with experimental measurements. In the inner region, variables such as the fluid density and vertical velocity change rapidly in the horizontal direction, y , so that a Wooding-type boundary-layer approximation can be applied in deriving the self-similar solution. In the outer region, by contrast, we assume that the vertical velocity and density perturbation are both zero. Our solution is therefore qualitatively similar to the “top hat” description of turbulent free plumes, first proposed by Morton *et al.* (1956), where molecular diffusion is likewise ignored.

The self-similar solution allows us to compute the plume volume flux, Q , and mean reduced gravity, \bar{g}' , as functions of x , the vertical coordinate. Indeed (2.24) and (2.25) respectively indicate that Q and \bar{g}' are proportional to $x^{1/4}$ and $x^{-1/4}$ contrary to the scalings $x^{1/3}$ and $x^{-1/3}$ that apply when $\text{Pe} \lesssim \mathcal{O}(1)$ (Wooding, 1963; Roes *et al.*, 2014). The values of Q and \bar{g}' calculated at the bottom of the control volume, comprise the source conditions for the pair of gravity currents that are formed when the plume encounters the impermeable bottom boundary. The equations governing porous media gravity current flow are reviewed in section 2.3.2. In particular, the self-similar ODE (2.33), originally derived by Huppert & Woods (1995) for (hydrostatic) gravity current flow and based on Darcy’s law (2.28) and a volume conservation equation (2.29), describes the variation of the gravity current height in space and time. The self-similar ODE (2.33), and associated boundary conditions (2.34), is solved by employing a shooting method to draw curves such as those shown in figure 2.3. Once the gravity current reaches the (impermeable) vertical sidewall of the control volume at $t = t_L$, the motion becomes primarily vertical. The solution describing the motion of the first front, the interface separating the discharged plume fluid from

the overlying ambient fluid, is presented in section 2.3.3. Similar to the gravity current problem, the equation that describes the spatio-temporal evolution of the first front, (2.41), is also based on Darcy’s law and a volume conservation equation. However, in this case no self-similar solution is possible and hence a finite difference numerical method is applied instead. Figure 2.4 indicates that the first front, whose initial shape matches that of the gravity current at $t = t_L$, becomes progressively more horizontal with time so that, in the large t limit, the first front moves only vertically. Moreover, the advection speed of the first front decreases as it moves towards the plume source.

To verify key model predictions, complementary experiments are performed using fresh water and salt water as the working fluids. Particular emphasis is placed on the motion of the gravity current and of the first front, both of which depend on Q and \bar{g}' . A comparison between theory and experiment is given in section 2.5. Figures 2.7 and 2.8 show, respectively, the gravity current front position, L_g , vs. t , and the gravity current height, h , vs. y at three different instants in time. Conversely figure 2.9 shows the shape of the first front, again for three different values of t . Finally figure 2.10 presents the time variation of the average first front elevation, \bar{h} . In all cases, the agreement between the predictions and the measurements is promising. Thus, the experimental measurements provide support for the functional form of our plume solution according to which $Q \propto x^{1/4}$.

By necessity, the present research is conducted using a set of limiting assumptions: the medium is isotropic, the fluids are miscible and the flow is both Boussinesq and of Darcy type. In many geological scenarios of interest, however, other factors e.g. surface tension and anisotropy may be relevant. In future research, the most restrictive of our assumptions will be relaxed by studying filling box flow in media characterized by spatially-variable ϕ and k . Further extensions of the research could include an examination of non-Boussinesq and/or non-Darcy flow.

Chapter 3

Filling box flows in an axisymmetric geometry

3.1 Abstract

We present an analytical solution for buoyancy-driven “filling box” flows in axisymmetric porous media having closed bottom and side boundaries. The flow consists first and foremost of a descending, point source plume. When plume fluid reaches the (horizontal) bottom boundary, it begins to flow radially outward in the form of an axisymmetric gravity current. The leading edge of the gravity current advances with time as $t^{1/2}$ until it reaches the vertical sidewalls. At this point, the flow is characterized by a vertically-ascending “first front” that steadily advects towards the plume source. We assume the plume to be in a Darcy regime, i.e. $\text{Re} \lesssim \mathcal{O}(10)$, with $\text{Pe} > \mathcal{O}(1)$, where Re and Pe are respectively the Reynolds and Péclet numbers, and derive a similarity solution for the plume by applying a boundary layer approximation. Formulas are thereby obtained for the vertical variation of the plume volume flux and area-averaged concentration. The former result shows important qualitative differences with the analogue equation derived in the limit $\text{Pe} < \mathcal{O}(1)$. In particular, the plume volume flux is now predicted to explicitly depend on the reservoir permeability, plume buoyancy flux and fluid viscosity. The gravity current problem is likewise solved using a self-similar solution, this time adapted from the work of Lyle et al. (*J. Fluid Mech.* vol. 543, 293–302, 2005) but connected to the outflow conditions of the plume. Finally, in solving for the motion of the first front, we apply a volume flux balance equation

and thereby estimate the time scale required for the first front to advect from the bottom of the control volume to the source elevation. By synthesizing the above results, we can estimate the total volume of source fluid and mass of solute that can be injected into an axisymmetric reservoir without overflow. Predictions can also be made for the time-variable mean concentration of this contaminated fluid layer, which must obviously be less than the source concentration.

3.2 Introduction

The term “filling box flows” was first coined by Baines & Turner in 1969 (Baines & Turner, 1969) in their study of buoyant convection from an isolated source in a closed cylindrical control volume devoid of porous media. Since then filling box flows have been studied extensively because of their applicability to numerous environmental and industrial scenarios, e.g. in volcanic and submarine pumice eruptions (Woods, 2010), hydrothermal plumes (Speer & Rona, 1989) and building ventilation (Nabi & Flynn, 2013). A recent theoretical and similitude laboratory experimental extension of the filling box methodology has been to the case of porous media plumes that rise or fall within “leaky” (Roes *et al.*, 2014) or closed (Sahu & Flynn, 2015) aquifers. The latter case is of particular interest because of its applicability to numerous geophysical and industrial scenarios, for instance, (i) injection of hot water underground for the purpose of thermal storage in a confined reservoir (Dudfield & Woods, 2012), (ii) injection, and subsequent dissolution, of supercritical CO₂ into deep saline aquifers for purposes of sequestering the CO₂ that is produced as a result of localized industrial activities, e.g. coal combustion for power generation (Bolster, 2014), (iii) dense plumes generated as a result of leakages from landfills, waste piles or composting facilities that subsequently contaminate potable groundwater (Lesage & Jackson, 1992; Ostrom *et al.*, 2007; Parlange & Hopmans, 1999), (iv) disposal by re-injection of the produced water associated with either shale gas or heavy oil activities (McCurdy, 2011; Shaffer *et al.*, 2013). In each case, a comprehensive analytical description of the flow requires combination of vertical convection and the primarily horizontal

flow that follows when plume fluid reaches an impermeable horizontal boundary.

In this spirit, a central objective of the present contribution is to expand upon existing descriptions of porous media filling box flows by extending the Cartesian analysis employed in Sahu & Flynn (2015) to an axisymmetric geometry. Such an extension is not at all trivial; for instance, it provides an opportunity to supplement a well-established, but physically counter-intuitive, expression for the plume volume flux – see (1) and the corresponding discussion below. A further objective of our research is to clarify the mathematical treatment of the different components of the dispersion tensor under the boundary layer approximation and thereby justify, more carefully than before, why some of these terms can be safely ignored.

As suggested by the schematics of figure 3.1, we divide our problem into three constituent parts comprising the plume, gravity current and the first front. Although the plume shown in figure 3.1 is negatively-buoyant, it should be understood that dynamically equivalent results are expected if the plume rises rather than falls, provided, of course, that the flow is Boussinesq, i.e. density differences are less than about 10%. Note that in either orientation, we assume that the plume originates from a compact source and thereafter propagates through a uniform porous medium. The gravity current describes the radially outward motion of the discharged plume fluid over an impermeable horizontal boundary. Unlike the studies of Neufeld *et al.* (2011) and Roes *et al.* (2014), we do not include any localized sinks in this bottom boundary and so the gravity current outflow is uniform in all directions. Finally the first front describes the primarily vertical motion of this discharged plume fluid after the leading edge of the gravity current has reached the impermeable vertical walls that define the sidewalls of the control volume.

A solution for axisymmetric plumes falling through an unbounded porous medium can be derived from a Wooding (1963)-type boundary layer approximation using a constant value for the dispersion coefficient. On this basis, and supposing that dispersion is, in fact, dominated by molecular diffusion effects, the plume volume flux, Q , can be shown to vary with the vertical distance, x ,

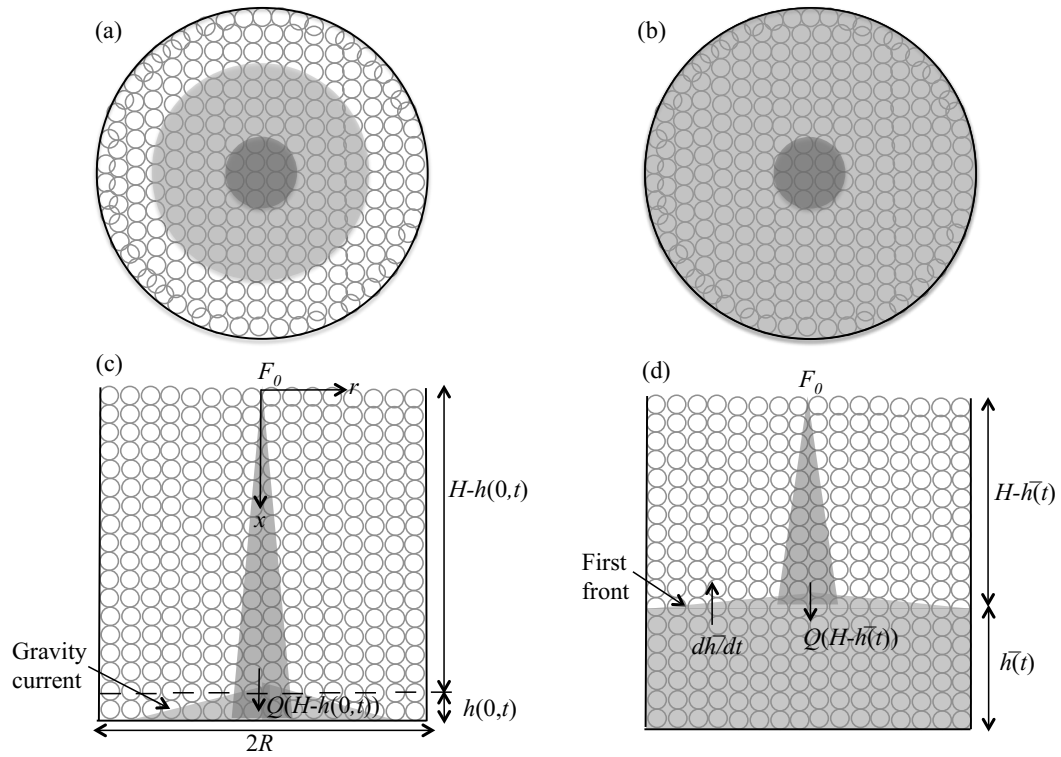


Figure 3.1: Schematic of a filling box flow in an axisymmetric geometry. (a) and (c) represent, respectively, the top view and front view of the plume and gravity current. (b) and (d) represent, respectively, the top and front view of the plume and the first front.

from the source as

$$Q = 8\pi D_d \phi x. \quad (3.1)$$

(see equation 7.5.34 of Phillips (1991), section 9.10 of Turcotte & Schubert (2014) and equation 3.1 of Roes *et al.* (2014)). Here D_d is the solute molecular diffusion coefficient and ϕ is the porosity. This equation is notable for several reasons. Firstly, and as suggested above, it assumes that mechanical dispersion is subordinate to molecular diffusion. Thus the Péclet number, which is defined as the ratio of mass transfer by mechanical dispersion to mass transfer by diffusion, is $\text{Pe} = \frac{dU\tau}{D_d} < \mathcal{O}(1)$, where d is the mean grain size, U is the transport velocity and $\tau (> 1)$ is the tortuosity constant, which is defined as the ratio of the actual path length traveled by a solute molecule to the distance it would travel in a free medium. Conversely when $\text{Pe} > \mathcal{O}(1)$, a situation not at all uncommon in practice, mechanical dispersion effects dominate over molecular diffusion and must therefore be taken into account when evaluating the mass transfer. In this case, the diffusion coefficient must be replaced by a dispersion tensor whose components depend on the flow velocity. More specifically, the components of the dispersion tensor are associated with the normal and tangential directions of the longitudinal and radial components of the velocity field as explained by Ogata (1970) and reviewed in greater detail below.

Equation (3.1) is also notable for the fact that Q is independent of the plume buoyancy flux, F . This prediction, though mathematically consistent, is quite different from the corresponding result for a line source plume for which

$$Q = \left(\frac{36D_d\phi Fk\Lambda^2x}{\nu} \right)^{1/3} \quad (3.2)$$

where Λ is the width of the line source, k is the permeability and ν is the kinematic viscosity (Phillips, 1991). Note, moreover, that free plumes, whether axisymmetric or 2D planar both predict Q to vary with F – see e.g. (5) and (16) of Baines & Turner (1969). Equations (1) and (2) also differ in that the plume volume flux depends on k and ν only in the latter instance. Thus one of the strong motivations for extending the analysis of Sahu & Flynn (2015) to the case of an axisymmetric plume issuing from a point source is to determine whether the unusual functional

form of (1) is somehow preserved. Indeed, as we illustrate below, by specifically considering $Pe > \mathcal{O}(1)$, it is possible to derive a self-similar solution for Q that more closely conforms to (2) and the related expressions from free plume theory.

The second part of the filling box flow consists of a gravity current, which is formed when dense plume fluid reaches the bottom impermeable boundary. In this case, the plume acts as a distributed source of dense fluid for the axisymmetric gravity current; the plume volume flux and mean reduced gravity at the bottom of the control volume are therefore needed in order to correctly specify the gravity current inflow conditions. Lyle et al. (2005) studied the axisymmetric gravity current problem both theoretically and experimentally, but in a radially infinite ambient. We adopt their theoretical solution, couple it with the equations describing the descending plume and finally present a solution for the horizontal motion of the discharged plume fluid in a finite ambient.

Note finally that as the gravity current propagates radially outward, it gets progressively thinner. At a particular point in time, t_R , the (well-defined) leading edge of the gravity current reaches the cylindrical sidewall. We develop estimates for t_R and also the height profile of the gravity current at this instant in time. The latter piece of information is needed when modelling the subsequent motion of the discharged plume fluid back towards the plume source. This primarily vertical motion is characterized by a so-called first front, which separates dense fluid below from fresh ambient fluid above. The shape of this first front obviously matches that of the gravity current when $t = t_R$ but its slope subsequently decreases as the first front advects upwards. We follow the approach of volume flux balance, presented by Sahu & Flynn (2015) for the rectilinear case, and derive an equation that describes the temporal evolution of the first front. Thus the motion of the first front will be shown to depend on both the solution of the plume and the gravity current problems.

The rest of the manuscript is organized as follows: we present a theoretical solution for the plume, gravity current and first front in sections 3.3, 3.4 and 3.5, respectively. Thereafter section 3.6 shows the output of our composite analytical model, discusses the key time scales associated with a filling box flow

and identifies conditions associated with a maximal filling of the control volume. Finally, section 3.7 summarizes the work as a whole and briefly identifies topics for further study.

3.3 Plume

The flows exhibited schematically in figure 3.1 are assumed to be both Boussinesq and miscible. Flow speeds are small enough that the flow remains laminar but large enough so that $Pe > \mathcal{O}(1)$. We further assume that the porous medium is uniform and saturated. Therefore the governing equations, i.e. mass continuity, momentum conservation in x and r , solute transport by advection-dispersion and a (linear) equation of state, are respectively given by

$$\frac{\partial u}{\partial x} + \frac{\partial v}{\partial r} = 0, \quad (3.3)$$

$$\frac{1}{\rho_0} \frac{\partial P}{\partial x} + \frac{\nu}{k} u = \frac{g\rho}{\rho_0}, \quad (3.4)$$

$$\frac{1}{\rho_0} \frac{\partial P}{\partial r} + \frac{\nu}{k} v = 0, \quad (3.5)$$

$$\frac{1}{\phi} \left(u \frac{\partial C}{\partial x} + v \frac{\partial C}{\partial r} \right) = \frac{\partial}{\partial x} \left(D_{xx} \frac{\partial C}{\partial x} + D_{xr} \frac{\partial C}{\partial r} \right) + \frac{1}{r} \frac{\partial}{\partial r} \left(D_{rx} r \frac{\partial C}{\partial x} + D_{rr} r \frac{\partial C}{\partial r} \right), \quad (3.6)$$

$$\rho = \rho_\infty (1 + \beta C). \quad (3.7)$$

Here u and v are the transport velocities in the axial and radial directions, respectively. Meanwhile, P is the fluid pressure, C is the solute concentration, β is the solute contraction coefficient and ρ is the fluid density, which approaches a constant value of ρ_∞ in the far-field limit, $r \rightarrow \infty$. Furthermore, D_{xx} , D_{xr} , D_{rx} and D_{rr} are respectively the components of the axial and radial dispersion coefficients in the tangential and normal directions.

By combining (3.4) and (3.5), it can be shown that

$$\frac{\nu}{k} \left(\frac{\partial u}{\partial r} - \frac{\partial v}{\partial x} \right) = \frac{g}{\rho_0} \frac{\partial \rho}{\partial r}. \quad (3.8)$$

Next, by applying the former of Wooding's two boundary layer conditions (Wooding, 1963), we conclude

$$\left| \frac{\partial v}{\partial x} \right| \ll \left| \frac{\partial u}{\partial r} \right|. \quad (3.9)$$

Incorporating (3.7) and (3.9) into (3.8) gives

$$\frac{\partial u}{\partial r} = \frac{g\beta k}{\nu} \frac{\partial C}{\partial r}. \quad (3.10)$$

Regarding the right-hand side of (3.6) and following Scheidegger (1961), the dispersion coefficients can be defined in terms of the axial velocity as follows: $D_{xx} = \alpha_{xx}u$, $D_{xr} = \alpha_{xr}u$, $D_{rx} = \alpha_{rx}u$ and $D_{rr} = \alpha_{rr}u$, where α_{xx} , α_{xr} , α_{rx} and α_{rr} are the corresponding dispersivity constants whose values vary between 0.01 to 1 cm (Delgado, 2007). Therefore (3.6) can be written as

$$\frac{1}{\phi} \left[u \frac{\partial C}{\partial x} + v \frac{\partial C}{\partial r} \right] = \frac{\partial}{\partial x} \left[u \left(\alpha_{xx} \frac{\partial C}{\partial x} + \alpha_{xr} \frac{\partial C}{\partial r} \right) \right] + \frac{1}{r} \frac{\partial}{\partial r} \left[ur \left(\alpha_{rx} \frac{\partial C}{\partial x} + \alpha_{rr} \frac{\partial C}{\partial r} \right) \right]. \quad (3.11)$$

Scheidegger (1961) further suggests that the tangential components of the dispersivity are larger than the normal components, and therefore $\alpha_{xx} \gg \alpha_{xr}$ and $\alpha_{rr} \gg \alpha_{rx}$. Also, from Wooding's latter boundary layer condition (Wooding, 1963), we have

$$\left| \frac{\partial C}{\partial x} \right| \ll \left| \frac{\partial C}{\partial r} \right|. \quad (3.12)$$

Thus, it can be shown that

$$\left| \alpha_{xx} \frac{\partial C}{\partial x} \right| \sim \left| \alpha_{xr} \frac{\partial C}{\partial r} \right| \quad \text{and} \quad \left| \alpha_{rx} \frac{\partial C}{\partial x} \right| \ll \left| \alpha_{rr} \frac{\partial C}{\partial r} \right|. \quad (3.13)$$

However, on performing a scaling analysis and remembering that axial length scales are much larger than their radial counterparts, we find

$$\left| \frac{\partial}{\partial x} \left(u \alpha_{xr} \frac{\partial C}{\partial r} \right) \right| \sim \left| \frac{1}{r} \frac{\partial}{\partial r} \left(ur \alpha_{rx} \frac{\partial C}{\partial x} \right) \right|, \quad (3.14)$$

which suggests that only the final term on the right hand side of (3.11) is dynamically significant. In other words, (3.11) can be rewritten in the following approximate form:

$$u \frac{\partial C}{\partial x} + v \frac{\partial C}{\partial r} = \frac{\phi}{r} \frac{\partial}{\partial r} \left(ur \alpha_{rr} \frac{\partial C}{\partial r} \right). \quad (3.15)$$

Hereafter we refer α_{rr} to simply as α .

We now introduce a streamfunction, ψ , such that $u = \frac{1}{r} \frac{\partial \psi}{\partial r}$ and $v = -\frac{1}{r} \frac{\partial \psi}{\partial x}$. Therefore on further substitution, (3.10) and (3.15) respectively become

$$\frac{1}{r} \frac{\partial^2 \psi}{\partial r^2} - \frac{1}{r^2} \frac{\partial \psi}{\partial r} = \frac{g\beta k}{\nu} \frac{\partial C}{\partial r}, \quad (3.16)$$

$$\frac{\partial \psi}{\partial r} \frac{\partial C}{\partial x} - \frac{\partial \psi}{\partial x} \frac{\partial C}{\partial r} = \alpha \phi \left(\frac{\partial^2 \psi}{\partial r^2} \frac{\partial C}{\partial r} + \frac{\partial \psi}{\partial r} \frac{\partial^2 C}{\partial r^2} \right). \quad (3.17)$$

We seek a self-similar solution to (3.16) and (3.17) of the form

$$\psi = A_1 x^p \mathcal{F}(\eta), \quad C = A_2 x^q \mathcal{G}(\eta) \quad (3.18)$$

where $\eta = A_3 \frac{r}{x^m}$ is the self-similar variable and A_1 , A_2 and A_3 are constants to be determined shortly. Substituting (3.18) into (3.16) and further simplifying gives

$$\eta \mathcal{F}'' - \mathcal{F}' = \frac{g\beta k}{\nu} \frac{A_2}{A_1} \frac{r^2 x^q}{x^p} \mathcal{G}' = \frac{g\beta k}{\nu} \frac{A_2}{A_1 A_3^2} \left[\frac{A_3 r}{x^{(p-q)/2}} \right]^2 \mathcal{G}' \quad (3.19)$$

Self-similarity requires that $p-q = 2m$ so that $\eta = A_3 \frac{r}{x^{(p-q)/2}}$ and $A_2 = \frac{\nu}{g\beta k} A_1 A_3^2$. Upon making these substitutions, (3.19) simplifies dramatically, i.e.

$$\eta \mathcal{F}'' - \mathcal{F}' = \eta^2 \mathcal{G}'. \quad (3.20)$$

From (3.18), and remembering that the solute concentration is maximal at $r = 0$ and vanishingly small when $r \rightarrow \infty$, we have the following boundary conditions to be applied in conjunction with (3.20): $\mathcal{G}' = 0$ at $\eta = 0$ and $\mathcal{G} = 0$ when $r \rightarrow \infty$. We shall apply the former boundary condition later; employing the latter boundary condition now, it can be shown that (3.20) has a general solution of the form

$$\mathcal{G} = \frac{\mathcal{F}'}{\eta}. \quad (3.21)$$

We now repeat the above process but focus attention on (3.17) rather than (3.16). Substituting (3.18) into (3.17), it can be shown that

$$\mathcal{F}'(q\mathcal{G} - m\mathcal{G}'\eta) - (p\mathcal{F} - m\mathcal{F}'\eta)\mathcal{G}' = \alpha\phi x^{(1-2m)} A_3^2 (\mathcal{F}''\mathcal{G}' + \mathcal{F}'\mathcal{G}''). \quad (3.22)$$

By selecting $m = 1/2$ and $A_3 = 1/\sqrt{\alpha\phi}$, (3.22) reduces to the following simpler form:

$$\mathcal{F}''\mathcal{G}' + \mathcal{F}'\mathcal{G}'' - q\mathcal{F}'\mathcal{G} + p\mathcal{F}\mathcal{G}' = 0. \quad (3.23)$$

To determine p and q , we recall that the buoyancy flux, F , is constant and equal to its source value, F_0 . Thus

$$2\pi \int_0^\infty ug'r \, dr = F_0. \quad (3.24)$$

Here $g' = g \frac{\rho - \rho_\infty}{\rho_\infty} = g\beta C$ is the reduced gravity of the plume. Substituting (3.18) into (3.24), shows that

$$2\pi x^{p+q} A_1 A_2 g \beta \int_0^\infty \mathcal{F}' \mathcal{G} dr = F_0, \quad (3.25)$$

and this in turn implies $p + q = 0$. Recalling $p - q = 2m = 1$, we conclude that $p = 1/2$ and $q = -1/2$. Also, with reference to (3.25), and remembering that $A_2 = \frac{\nu}{g\beta k} A_1 A_3^2$ and $A_3 = 1/\sqrt{\alpha\phi}$, it is easy to verify that

$$A_1 = \left(\frac{F_0 k \alpha \phi}{2\pi\nu} \frac{1}{\int_0^\infty \mathcal{F}' \mathcal{G} d\eta} \right)^{1/2}.$$

Using the above results, (3.23) takes the form

$$\mathcal{F}'' \mathcal{G}' + \mathcal{F}' \mathcal{G}'' + \frac{1}{2} \mathcal{F}' \mathcal{G} + \frac{1}{2} \mathcal{F} \mathcal{G}' = 0. \quad (3.26)$$

After combining (3.21) and (3.26), and with some algebra, we get

$$\mathcal{G}'' + \frac{\mathcal{G}'}{\eta} + \mathcal{G} = 0. \quad (3.27)$$

\mathcal{G} therefore represents a Bessel function of first kind, $J_0(\eta)$, and can be expressed in integral form as

$$\mathcal{G} = J_0(\eta) = \frac{2}{\pi} \int_0^{\pi/2} \cos(\eta \sin \theta) d\theta. \quad (3.28)$$

Before applying this solution to the problem at hand, we recall the assumption that $\text{Pe} > \mathcal{O}(1)$, or $D_{rr} = \alpha u$. In the region close to the plume centerline where flow velocities are comparatively large, this approximation is certainly appropriate, however, the above assumption breaks down as we move to the far-field, which is characterized by much smaller vertical (and radial) velocities. We therefore divide our solution into an inner region where $\text{Pe} > \mathcal{O}(1)$ and an outer region where $\text{Pe} \leq \mathcal{O}(1)$. In determining the appropriate boundary between the inner and outer region, recall that \mathcal{G} represents the solute concentration (see equation 3.18), whose value cannot become negative. Therefore the inner region is formally defined by $\eta \leq \eta_{\max} = 2.4048$ for which $\mathcal{G} \geq 0$ (Zakharov, 2009). In the outer region, we assume, consistent with the analysis of Sahu & Flynn (2015),

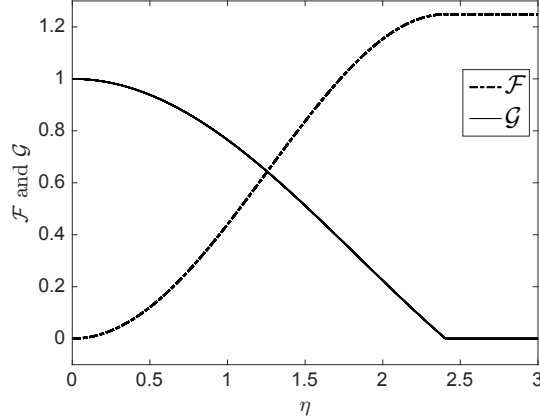


Figure 3.2: Analytical solution obtained for the self-similar functions \mathcal{G} and \mathcal{F} of (3.18) vs. the self-similar variable, η .

that the fluid velocity and solute concentration are identically zero. Thus, in place of (27), it is more appropriate to write

$$\mathcal{G} = \begin{cases} \frac{2}{\pi} \int_0^{\pi/2} \cos(\eta \sin \theta) d\theta, & \eta \leq \eta_{\max} \\ 0, & \eta > \eta_{\max}. \end{cases} \quad (3.29)$$

Furthermore, by considering the relationship between \mathcal{G} and \mathcal{F}' from (3.21), the solution for \mathcal{G} can be extended to find \mathcal{F} such that

$$\mathcal{F} = \begin{cases} \frac{2}{\pi} \int_0^{\eta} \int_0^{\pi/2} \cos(\eta \sin \theta) d\theta d\eta, & \eta \leq \eta_{\max} \\ 1.2485, & \eta > \eta_{\max}. \end{cases} \quad (3.30)$$

The variation of \mathcal{F} and \mathcal{G} with η are presented in figure 3.2. The kink, or a discontinuity in other words, observed in the curve of \mathcal{G} is because of the division of plume solution into inner and outer regions. The solution presented by (3.28) for (3.27) is therefore valid only in the inner region, i.e. when $\eta \leq \eta_{\max} = 2.4048$. Furthermore, by combining (3.29) and (3.30) with (3.18), a contour plot may be drawn that shows the variation of u/u_0 or, equivalently, C/C_0 with x/H and r/H where u_0 and C_0 are the plume vertical velocity and solute concentration at the source and H is the control volume height – see figure 3.3. Note that u and C therefore vary in proportion to one another.

With a formula for ψ to hand, it is straightforward to evaluate the plume

volume flux, Q , i.e.

$$Q = 2\pi \int_0^\infty u \, dr = \left[2\pi \frac{F_0 k \alpha \phi}{\nu} \frac{\left(\int_0^\infty \mathcal{F}' \, d\eta \right)^2}{\int_0^\infty \frac{\mathcal{F}'^2}{\eta} \, d\eta} x \right]^{1/2}. \quad (3.31)$$

From the solution presented in figure 3.2, we have $\frac{\left(\int_0^\infty \mathcal{F}' \, d\eta \right)^2}{\int_0^\infty \frac{\mathcal{F}'^2}{\eta} \, d\eta} = 2$. Thus the volume flux for an ideal plume with $\text{Pe} > \mathcal{O}(1)$ and $D_{rr} = \alpha u$ is given simply by

$$Q = \left(\frac{4\pi F_0 k \alpha \phi}{\nu} x \right)^{1/2}. \quad (3.32)$$

On comparing this result with (3.1), our result shows that the plume volume flux depends not only on the porosity, but also on the plume buoyancy flux, the reservoir permeability and the fluid kinematic viscosity, all of which seems very reasonable on physical grounds. Another potentially significant difference with (3.1) is that this previous equation predicts $Q \propto x$, whereas our solution predicts a more conservative result, namely $Q \propto x^{1/2}$.

Because the plume buoyancy flux is constant, it is straightforward to obtain an expression for the plume mean reduced gravity, averaged over the cross section. The corresponding formula,

$$\bar{g}' = g\beta\bar{C} = \left(\frac{F_0\nu}{4\pi k\alpha\phi} \frac{1}{x} \right)^{1/2}, \quad (3.33)$$

unambiguously specifies the connection between \bar{g}' , \bar{C} , F_0 and x . For (3.32) and (3.33) to be applicable to a nonideal plume, for which the source volume flux is not vanishingly small, we back-extrapolate our result so that $Q = 0$ at a virtual source defined by $x = -x_0$ (Hunt & Kaye, 2001; Wooding, 1963). Thus

$$x_0 = \frac{\nu Q_0^2}{4\pi F_0 k \alpha \phi} = \frac{\nu Q_0}{4\pi g'_0 k \alpha \phi}, \quad (3.34)$$

where g'_0 is the reduced gravity of the source fluid. Therefore for a nonideal plume, the volume flux and mean reduced gravity are given, respectively, by

$$Q = \left[\frac{4\pi F_0 k \alpha \phi}{\nu} (x + x_0) \right]^{1/2}. \quad (3.35)$$

and

$$\bar{g}' = g\beta\bar{C} = \left[\frac{F_0\nu}{4\pi k\alpha\phi} \frac{1}{(x + x_0)} \right]^{1/2}. \quad (3.36)$$

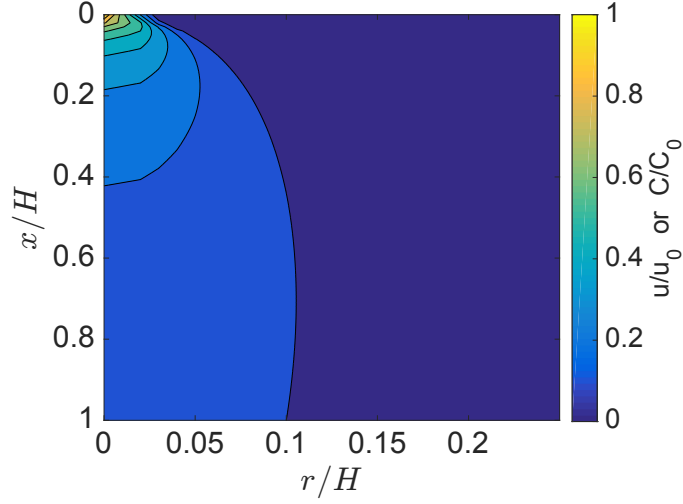


Figure 3.3: [Colour online] Contours showing the variation of u/u_0 or C/C_0 with x/H and r/H where u_0 and C_0 are respectively the plume vertical velocity and solute concentration at the source.

Substituting x_0 using (3.34) and expressing (3.35) and (3.36) in non-dimensional form yields

$$\begin{aligned} \frac{Q}{Q_0} &= \left[1 + \frac{4\pi g'_0 k \alpha \phi H}{Q_0 \nu} \left(\frac{x}{H} \right) \right]^{1/2} \quad \text{and} \\ \frac{\bar{g}'}{g'_0} &= \left[1 + \frac{4\pi g'_0 k \alpha \phi H}{Q_0 \nu} \left(\frac{x}{H} \right) \right]^{-1/2}. \end{aligned} \quad (3.37)$$

The functional variation of Q/Q_0 and \bar{g}'/g'_0 is depicted in the left- and right-hand side panels of figure 3.4, respectively.

The above results apply to a time-independent flow and so do not fully capture the dynamics associated with the initiation of dense source fluid and the thermal that results therefrom. Plumes and thermals share some similarities, of course, but also some important differences. In the former case, for instance, entrainment occurs only laterally whereas in the latter case, ambient fluid may also be entrained along the descending underside of the thermal. With this caveat in mind, we nonetheless proceed to estimate, on the basis of the previous formulas, the time interval, t_P , between activating the source and observing plume fluid along the lower impermeable boundary of the control volume. The average axial

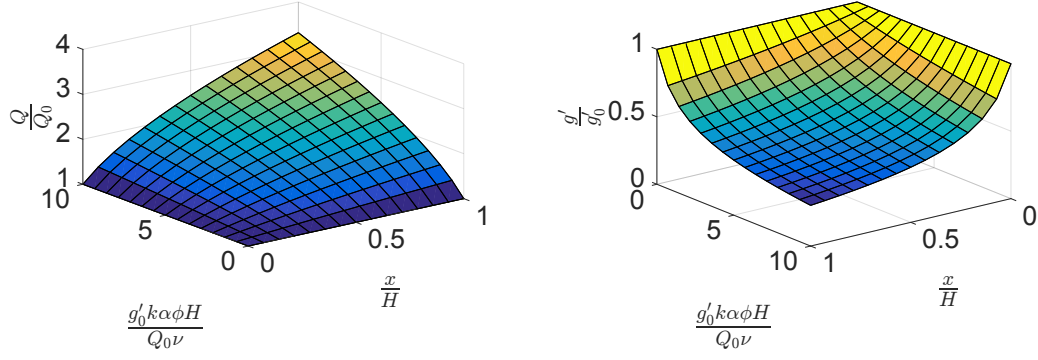


Figure 3.4: [Colour online] Variation of Q/Q_0 (left-hand side panel) and \bar{g}'/g'_0 (right-hand side panel) with x/H and $g'_0 k \alpha \phi H / (Q_0 \nu)$ – see (3.37).

plume velocity at any arbitrary elevation is given by

$$U(x) \equiv \frac{Q(x)}{A_p} = \left[\frac{4F_0 k}{\eta_{\max}^4 \pi \nu \alpha \phi} \frac{1}{(x + x_0)} \right]^{1/2} \quad (3.38)$$

where the plume cross-sectional area is given by $A_p = \pi b^2 = \pi \alpha \phi \eta_{\max}^2 x$. By extension, the mean value of $U(x)$ in a control volume having height H is given by

$$\bar{U} = \frac{1}{H} \int_0^H U(x) dx = \left(\frac{16F_0 k}{\pi \eta_{\max}^4 \nu \alpha \phi} \right)^{1/2} \left[(H + x_0)^{1/2} - x_0^{1/2} \right]. \quad (3.39)$$

Employing this result, the time required for the plume to traverse a vertical distance H is estimated as

$$t_P = \left(\frac{\pi \eta_{\max}^4 \nu \alpha \phi}{16F_0 k} \right)^{1/2} \frac{H}{\left[(H + x_0)^{1/2} - x_0^{1/2} \right]}. \quad (3.40)$$

Below, we shall compare t_P against other relevant time-scales of the flow e.g. those due to the gravity current and ascending first front.

3.4 Gravity current

As the dense plume reaches the impermeable bottom of the cylindrical control volume, it transitions to a gravity current and propagates radially outward. Assuming a hydrostatic pressure condition, and adapting the self-similar solution

presented by Lyle *et al.* (2005), we may describe the motion of the gravity current as outlined below.

According to Darcy's law, the outward radial velocity of the discharged dense fluid can be expressed as a function of the slope of the interface that separates this fluid from the overlying ambient, i.e.

$$v_g = -\frac{kg'_g}{\nu} \frac{\partial h}{\partial r}. \quad (3.41)$$

Here h is the interface height as depicted in figure 3.1 and g'_g is the mean reduced gravity calculated at $x = H$ using (3.36).

Local volume flux balance states that the difference of the volumetric inflow and outflow at any radial location r must be balanced by the time rate of change of the interface height at the same location. Expressing this balance mathematically yields

$$\phi \frac{\partial h}{\partial t} + \frac{1}{r} \frac{\partial}{\partial r} (rv_g h) = 0. \quad (3.42)$$

On combining (3.41) and (3.42), we find that

$$\frac{\partial h}{\partial t} - \frac{S}{r} \frac{\partial}{\partial r} \left(rh \frac{\partial h}{\partial r} \right) = 0, \quad (3.43)$$

where $S = \frac{kg'_g}{\nu\phi}$. The above equation is a nonlinear heat equation and is subject to the following boundary conditions:

$$h(r_N, t - t_P) = 0 \quad \text{and} \quad 2\pi\phi \int_0^{r_N(t-t_P)} rh(r, t - t_P) dr = V_g(t - t_P). \quad (3.44)$$

Here r_N is the radial distance measured from the origin to the gravity current leading edge (or nose) and V_g is the total volume of fluid discharged by the plume up till time $t - t_P > 0$. The former boundary condition states that the height of the gravity current at its leading edge is always zero. By contrast, the latter boundary condition states that the amount of the dense fluid contained within the gravity current must equal V_g . Following Lyle *et al.*'s approach, we define a self-similar solution of the form

$$\begin{aligned} h(r, t - t_P) &= \xi_N^2 \left(\frac{Q_g}{S} \right)^{1/2} \mathcal{H}(y) \quad \text{where} \\ \xi(r, t - t_P) &= \frac{r}{(SQ_g)^{1/4} (t - t_P)^{1/2}}. \end{aligned} \quad (3.45)$$

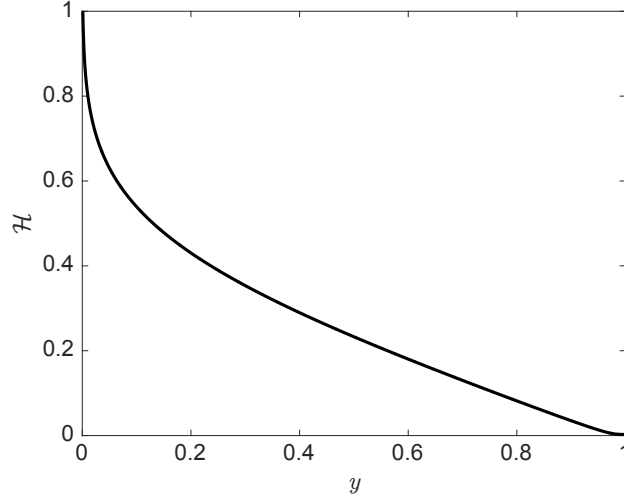


Figure 3.5: Dimensionless gravity current height \mathcal{H} vs dimensionless radius y .

Here $0 \leq y = \xi/\xi_N \leq 1$ and $\xi_N = \xi(r_N, t - t_P)$ is the dimensionless radius of the leading edge. On substituting (3.45) into (3.43), we obtain

$$y\mathcal{H}''\mathcal{H} + y\mathcal{H}'\mathcal{H}' + \mathcal{H}'\mathcal{H} + \frac{y^2}{2}\mathcal{H}' = 0, \quad (3.46)$$

subject to the boundary conditions

$$\mathcal{H}(1) = 0 \quad \text{and} \quad \left[2\pi \int_0^1 y\mathcal{H} dy \right]^{-1/4} = \xi_N. \quad (3.47)$$

To find a solution to the above ODE, a shooting method is employed. Graphical results are presented in figure 3.5 and the value of ξ_N is found to equal 1.19. These results match very well with figures 2 and 3 of Lyle *et al.* (2005).

Using the above equations, the radius of the gravity current as a function of time $t > t_P$ can be given as

$$r_N = \xi_N(SQ_g)^{1/4}(t - t_P)^{1/2}. \quad (3.48)$$

On the other hand, the time required for the gravity current to reach the sidewalls of the cylindrical control volume, located at $r = R$, can be found from

$$t_R = \frac{R}{\xi_N(SQ_g)^{1/4}}, \quad (3.49)$$

where we assume that the plume radius at $x = H$ is negligible compared to R . In light of this definition, (3.48) can be simplified to read

$$\frac{r_N}{R} = \left(\frac{t - t_P}{t_R} \right)^{1/2} \quad \text{where} \quad t > t_P. \quad (3.50)$$

Finally we can also calculate the mean height of the gravity current at $t = t_R + t_P$ from the following equation:

$$\bar{h}_{t_R} = \frac{1}{R} \int_0^R h(y, t_R) dy = \xi_N^2 \left(\frac{Q_g}{S} \right)^{1/2} \int_0^1 \mathcal{H} dy = \xi_N^2 \left(\frac{Q_g}{S} \right)^{1/2} \bar{\mathcal{H}}. \quad (3.51)$$

From the numerical solution presented in figure 3.5, we find that $\bar{\mathcal{H}} \equiv \int_0^1 \mathcal{H} dy = 0.2641$. This result will be used in the following section where we describe the evolution of the flow for $t > t_R$.

3.5 First front

Once the gravity current reaches the impermeable sidewall, dense fluid begins moving upward and thus turns into a primarily vertical flow. As noted above, the interface between this ascending dense fluid and the ambient fluid is termed as the first front (Baines & Turner, 1969). In the analogue Cartesian problem (Sahu & Flynn, 2015), we observe that the curvature of the first front is comparatively high initially but then relaxes as the first front approaches the plume source. We expect similar behaviour here and so focus on the variable of greatest dynamical significance, namely the mean elevation, \bar{h} , of the first front, averaged over the cross sectional area of the control volume. Further following Sahu & Flynn (2015), we can apply a volume flux balance approach to find \bar{h} vs. time i.e.

$$\phi A \bar{U}_f(\bar{h}) = Q(H - \bar{h}). \quad (3.52)$$

Here $A = \pi R^2$ is the control volume cross-sectional area and $\bar{U}_f = \frac{d\bar{h}}{dt}$ is the mean advection speed of the first front, averaged over A . On substituting Q from (3.35) it can be shown that

$$\bar{h}_2 = H + x_0 - \left[(H + x_0 - \bar{h}_1)^{1/2} - \frac{(t_2 - t_1)}{A} \left(\frac{F_0 k \pi \alpha}{\nu \phi} \right)^{1/2} \right]^2 \quad (3.53)$$

where $\bar{h}_2 - \bar{h}_1$ is the mean vertical distance travelled by the first front over a time interval $t_2 - t_1$. By setting $\bar{h}_2 = H$ and $\bar{h}_1 = \bar{h}_{t_R}$, we can estimate the time, t_H , required by the first front to advect from the bottom to the top of the control

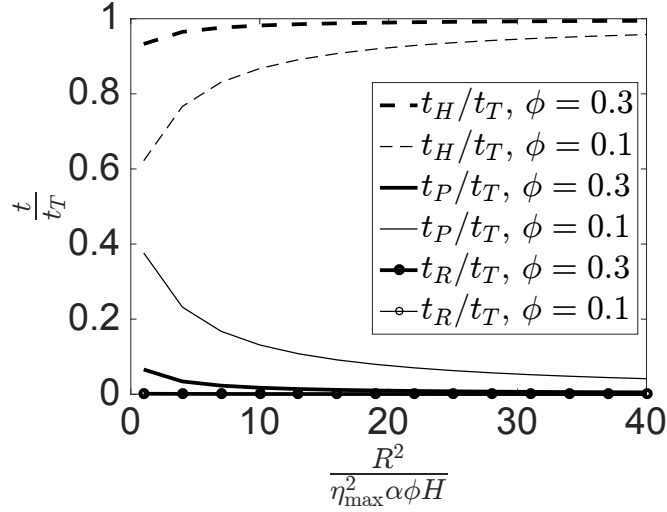


Figure 3.6: Time scales $\frac{t_P}{t_T}$, $\frac{t_R}{t_T}$ and $\frac{t_H}{t_T}$ vs. $\frac{R^2}{\eta_{\max}^2 \alpha \phi H}$ for $\phi = 0.1, 0.3$.

volume. Thus

$$t_H = A \left(\frac{\nu \phi}{F_0 k \pi \alpha} \right)^{1/2} \left[(H + x_0 - \bar{h}_{t_R})^{1/2} - x_0^{1/2} \right]. \quad (3.54)$$

3.6 Discussion

In the above sections we have separately considered solutions for the plume, gravity current and first front. The latter two solutions are applicable for a closed box or reservoir with an open upper boundary whose radius is significantly larger than the maximum plume radius i.e. $R \gg b_{\max}$. On substituting $b_{\max} = \eta_{\max}(\alpha \phi H)^{1/2}$, where $\eta_{\max} = 2.4048$, we get

$$\frac{R^2}{\eta_{\max}^2 \alpha \phi H} \gg 1. \quad (3.55)$$

For real geophysical flows, the horizontal length-scale is usually much larger than the vertical length scale; moreover $\phi < 0.38$ (Peters, 2012), $\alpha < 0.01$ m (Delgado, 2007), and therefore the above criteria is well satisfied.

In the context of filling box flows, an important parameter is the time, t_T , required to completely fill the control volume void space with contaminated fluid.

For $t > t_T$, we expect contaminated fluid overflow and, possibly, the advection of contaminated fluid above the elevation of the source. We calculate t_T by superposition, i.e.

$$t_T = t_P + t_R + t_H, \quad (3.56)$$

and focus attention on cases where (3.55) is valid. Plotting t_P , t_R and t_H vs. $\frac{R^2}{\eta_{\max}^2 \alpha \phi H}$ shows that t_H is typically much larger than either t_P or t_R (see figure 3.6). In our subsequent analysis, it is therefore appropriate to assume $t_T \approx t_H$ where t_H is given by (3.54) with $\bar{h}_{t_R} \rightarrow 0$. On the basis of this approximation, it is possible to simplify (3.53). To wit

$$\bar{h} = \left[1 - \left(1 - \frac{t}{t_H} \right)^2 \right] H, \quad (3.57)$$

where \bar{h} is the mean height of the first front at time t . Thus, based on the time of injection, the mean depth and volume, V_c , of the contaminated layer can be straightforwardly predicted. In particular, V_c is given by

$$V_c = \phi A \bar{h} = \phi A \left[1 - \left(1 - \frac{t}{t_H} \right)^2 \right] H. \quad (3.58)$$

Conversely, the volume of injected source fluid is simply $V_t = Q_0 t$. With V_c and V_t to hand, we can compute their ratio from

$$\frac{V_t}{V_c} = \frac{V_T}{V} \frac{t}{t_H} \frac{1}{\left[1 - \left(1 - \frac{t}{t_H} \right)^2 \right]}, \quad (3.59)$$

where $V = V_c(t = t_H) = \phi A H$ is the pore volume and $V_T = V_t(t = t_H) = Q_0 t_H$ is the total volume of source fluid that can be injected up to the point of overflow.

Having calculated the volume of the contaminated layer, an estimate for the associated mean reduced gravity, \bar{g}'_c , can be obtained from simple mass balance, i.e.

$$\bar{\rho}_c V_c = \rho_0 V_t + \rho_\infty (V_c - V_t). \quad (3.60)$$

Here ρ_0 is the density of the source fluid, ρ_∞ is the reservoir fluid density at $t = 0$ and $\bar{\rho}_c$ is the mean density of the contaminated fluid. Manipulation of (3.60) gives

$$\frac{\bar{\rho}_c - \rho_\infty}{\rho_\infty} = \frac{\rho_0 - \rho_\infty}{\rho_\infty} \frac{V_t}{V_c} \quad \text{or} \quad \frac{\bar{g}'_c}{g'_0} = \frac{V_t}{V_c}, \quad (3.61)$$

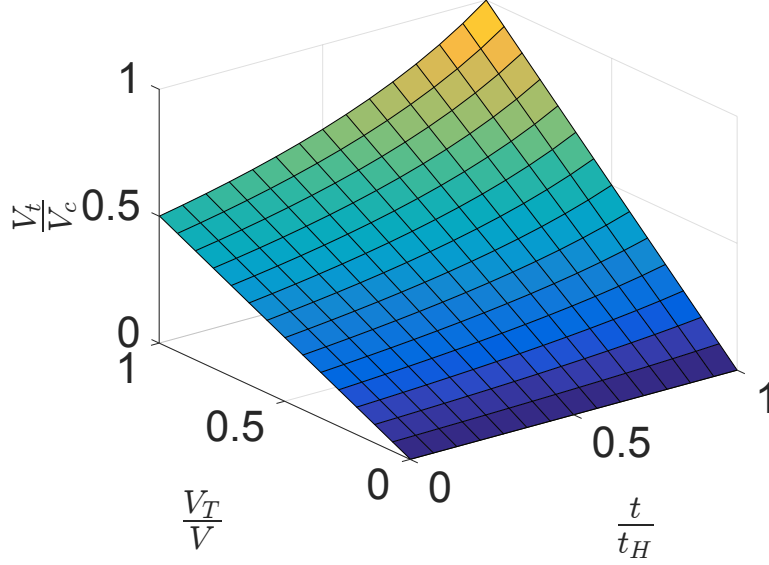


Figure 3.7: [Colour online] Volume ratio V_t/V_c vs. t/t_H for various V_T/V (see equation 3.59).

where g'_0 is the reduced gravity of the source fluid.

Figure 3.7 shows the variation of V_t/V_c with t/t_H for various V_T/V . The maximum value of \bar{g}'_c , realized when $t = t_H$, is $g'_0 \frac{V_T}{V}$. Using the definitions of V_T , V , (3.34) and (3.54), it can be shown that V_T/V varies with x_0/H as

$$\frac{V_T}{V} = \frac{2x_0}{H} \left[\left(1 + \frac{H}{x_0} \right)^{1/2} - 1 \right] \quad (3.62)$$

(see figure 3.8). Thus as x_0/H increases, so too does (i) the total volume of fluid injected up to the point of overflow relative to the pore volume, and, (ii) the final mean reduced gravity of the contaminated layer relative to the source reduced gravity. In turn, and for constant k , ϕ and H , (3.34) shows that larger V_T/V is associated, respectively, with larger and smaller Q_0 and g'_0 whereby entrainment into the plume is comparatively modest. Whereas the latter conclusion applies for arbitrarily small g'_0 , it cannot necessarily be said that the former applies for arbitrarily large Q_0 : large source volumes fluxes are associated with large flow velocities so that the Reynolds number restriction $\text{Re} \lesssim \mathcal{O}(10)$ must eventually be violated. More specifically, let us suppose a source diameter of $d_0 = 2b_0$ so

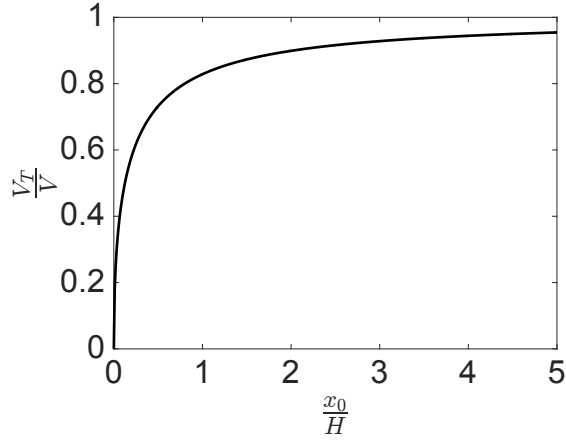


Figure 3.8: Variation of the volume ratio V_t/V_c vs. x_0/H based on (3.62).

that the source discharge velocity is given by $U_0 = \frac{4Q_0}{\pi d_0^2}$. Now on recalling that the Reynolds number in porous media is defined as $\text{Re} = \frac{dU_0}{\nu}$, we can conclude

$$Q_0 \leq \frac{5\pi\nu d_0^2}{2d}. \quad (3.63)$$

Using above results, we can also calculate the mass, M_T , of solute that can be sequestered up until $t = t_H$ from

$$M_T = C_0 V_T \quad (3.64)$$

where $C_0 = \frac{g'_0}{g\beta}$ is the solute concentration of the source fluid – see (3.7). Then by combining (3.64) with (3.54) and (3.34), it can be shown that

$$\frac{M_T\beta}{V} = \frac{\nu Q_0}{2\pi g k \alpha \phi H} \left[\left(1 + \frac{4\pi g k \alpha \phi H}{\nu Q_0} \frac{g'_0}{g} \right)^{1/2} - 1 \right]. \quad (3.65)$$

The variation of $\frac{M_T\beta}{V}$ with $\frac{\nu Q_0}{\pi g k \alpha \phi H}$ and $\frac{g'_0}{g}$ is shown in figure 3.9, which suggests that for a fixed pore volume, V , a larger mass of solute can be sequestered for larger Q_0 and g'_0 .

3.7 Conclusions

In this manuscript a solution for filling box flows in axisymmetric porous media, which has closed lower horizontal and side vertical boundaries, is presented. This

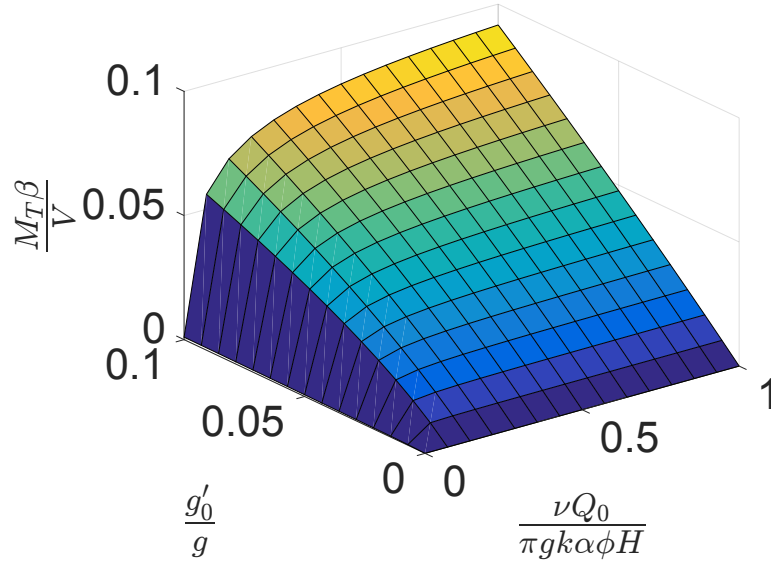


Figure 3.9: [Colour online] Dimensionless mass of sequestered solute, $M_T\beta/V$, vs. $\nu Q_0/(\pi g k \alpha \phi H)$ for various g'_0/g (see equation 3.65).

filling box model consists of three interrelated flow components: (i) a negatively-buoyant axisymmetric plume, (ii) a radially spreading gravity current consisting of plume fluid discharged along the bottom boundary, and (iii) an upwelling-type flow that develops after the gravity current reaches the sidewalls.

The plume is assumed to be in Darcy regime with $Pe > \mathcal{O}(1)$; moreover, the flow is Boussinesq and miscible. In section 3.3, we derive a novel similarity solution assuming an unstratified ambient and present formulas for the plume volume flux, Q , reduced gravity, \bar{g}' , and the time, t_P , required for the plume to reach the bottom of the control volume respectively in (3.35), (3.36) and (3.40). It is found that Q and \bar{g}' vary respectively as $x^{1/2}$ and $x^{-1/2}$, whereas in previous studies with $Pe < \mathcal{O}(1)$ it has been shown in that $Q \propto x$ and $\bar{g}' \propto x^{-1}$. We also argue that the new solution is more reasonable on physical grounds compared to the previous solution that Q and g' now depend on the buoyancy flux, viscosity and permeability, in addition to the porosity.

The above results are extended to derive a solution for the gravity current flow, where Q and \bar{g}' calculated at the bottom, $x = H$, of the control volume dictate

the gravity current source volume flux and reduced gravity, respectively. We adapt the similarity solution of Lyle *et al.* (2005), which is derived by combining Darcy’s law and a mass balance equation. By synthesizing the similarity solutions for plume and gravity current flow, we present in figure 3.5 a solution for the gravity current height profile. Moreover (3.49) gives the corresponding amount of time, t_R , required for the gravity current front to reach the vertical sidewalls, which are located a radial distance R from the plume source.

Finally when $t > t_P + t_R$, the dense plume discharge starts advecting upward towards the source elevation. There exists an interface between this dense fluid and the overlying ambient fluid which is termed the first front. An equation that describes the temporal evolution of the first front is derived in section 3.5 based on a volume flux balance borrowed from Sahu & Flynn (2015). We thereby obtain an estimate for the time, $t_H \gg t_P, t_R$, required for the first front to advect all the way to the elevation of the source.

In section 3.6, we estimate via (3.59) the total volume, V_T , of source fluid that can be injected into a reservoir of pore volume $V = \phi AH = \phi\pi R^2 H$ up to the point of overflow. For fixed reservoir properties and dimensions, larger V_T can be realized by respectively increasing and decreasing the source volume flux and source reduced gravity (or concentration). The corresponding maximum reduced gravity of the contaminated layer, consisting of source fluid plus ambient fluid entrained into the descending plume, is given by (3.61). Finally (3.65) gives an expression for the total mass of solute sequestered, again up till the point of overflow. In contrast to V_T , figure 3.9 confirms that it is advantageous to increase both the source volume flux and source concentration assuming the objective is to sequester as much of the solute as possible.

The current research is conducted assuming a Darcy flow regime with uniform porosity and permeability and miscible fluids. However, real geological reservoirs are characterized by spatial variations in ϕ and therefore k . In future, therefore, we will study filling box flows in porous medium with nonuniform permeability.

Chapter 4

The effects of sudden permeability changes in porous media filling box flows

4.1 Abstract

We report upon experimental and analytical investigations of filling box flows in non-uniform porous media characterized by a sudden change in the permeability. The porous medium consists of two layers separated by a horizontal interface and is initially filled with light ambient fluid. A line source located at the top of the upper layer supplies dense contaminated fluid that falls towards the bottom of the domain. Two configurations are studied, i.e. a low permeability layer on top of a high permeability layer and vice-versa. In the former scenario, the flow dynamics are qualitatively similar to the case of a uniform porous medium. Thus the analytical formulation of Sahu & Flynn (*J. Fluid Mech.*, vol. 782, 2015, pp. 455–478) can be adopted to compute the parameters of interest, e.g. the plume volume flux. In the latter scenario, the flow dynamics are significantly different from those of the uniform porous medium case; after reaching the interface, some fraction of the dense plume propagates horizontally as a pair of oppositely-directed interfacial gravity currents. Meanwhile, the remaining fraction of the plume flows downwards into the lower layer where it accumulates along the bottom boundary in the form of a deepening layer of discharged plume fluid. Depending on the permeability ratio of the upper and lower layers and the source conditions,

the gravity currents may become temporarily arrested after travelling some finite horizontal length. An analytical prediction for this so-called run-out length is adopted from Goda & Sato (*J. Fluid Mech.*, vol. 673, 2011, pp. 60–79), whose analysis pertains to immiscible fluids rather than the miscible fluids of interest here. Finally, a prediction of the filling box time, consisting of the time required to fill the control volume up to the point of contaminated fluid overflow, is made. These predictions are compared with analogue experimental measurements. Generally positive agreement is found when the higher permeability layer is located below the lower permeability layer. In the opposite circumstance, the agreement is conditional. If the run-out length of the gravity current is less than the horizontal dimensions of the control volume (or tank in case of the experiments), the agreement is relatively good. By contrast, when the run-out length is large, comparatively poor agreement may be realized: in spite of the higher density of the contaminated fluid, it may occupy the entirety of the upper layer before filling the lower layer.

4.2 Introduction

Filling box flows arise in closed or ventilated control volumes, often rectilinear or cylindrical in shape, where the flow is buoyancy-driven and originates from a compact hot or cold source. Though first developed in the context of turbulent buoyant convection (“plumes in rooms”), porous media filling box-type models have recently gained popularity because of their application to various geophysical phenomena, e.g. carbon sequestration (Bolster, 2014) and thermal storage in confined reservoirs (Dudfield & Woods, 2012). In that context, Roes et al. (2014) studied the particular impact of fissure drainage on the long time behaviour of a porous media filling box flow. As $t \rightarrow \infty$ outflow through the fissure(s) is balanced by the incoming volume flux supplied to the contaminated layer by the plume. They estimated the depth of this contaminated layer in terms of the plume source conditions (i.e. volume flux and reduced gravity), and the properties of the porous medium (height, porosity and permeability) and fissure(s)

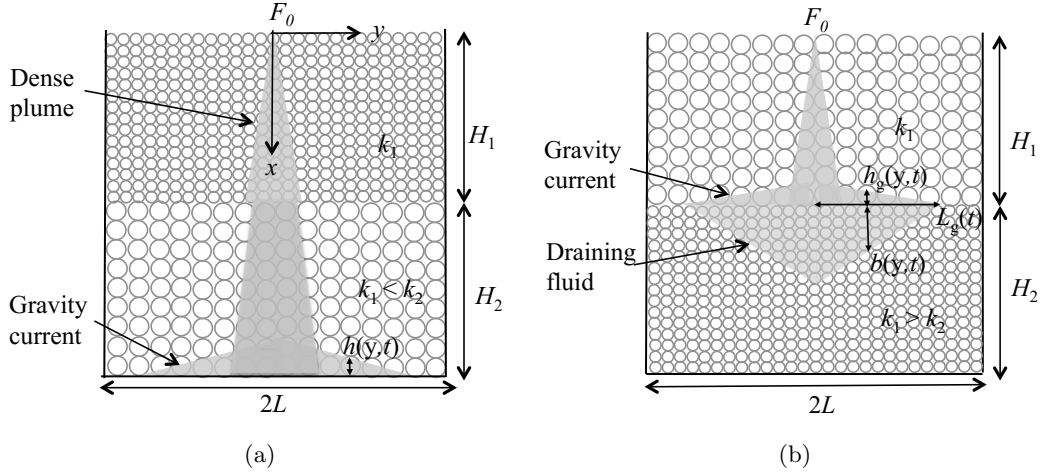


Figure 4.1: Filling box flows in two-layer porous media: (a) $k_1/k_2 < 1$, (b) $k_1/k_2 > 1$.

(height and permeability). Thereafter, and motivated by the analogue problem investigated by Baines & Turner (1969), Sahu & Flynn (2015, 2016b) studied filling box flows in closed rectilinear and axisymmetric geometries and presented analytical solutions for the associated flow dynamics consisting of a descending plume and plume outflow along the impermeable bottom boundary. For early times, the outflow takes the form of a horizontally-propagating gravity current or currents. Once the gravity current(s) reach the sidewalls of the control volume, there evolves a deepening layer of discharged plume fluid. An important simplifying assumption applied in each of the above studies is that they consider uniform porous media consisting of a constant porosity, ϕ , and permeability, k . In real geophysical scenarios, however, ϕ and k typically vary in space and can be considered constant only within localized, and often quite thin, geological strata. Although the effects of variations in ϕ and k have been studied previously in the context of gravity currents (Pritchard *et al.*, 2001; Goda & Sato, 2011), these effects remain unexplored in the more general context of filling box flows. Therefore in the present investigation, we study nonuniform porous media filling box flows paying particular attention to the effects of a sudden change of permeability between adjacent horizontal layers.

Figure 4.1 shows schematics of the flow and flow domain. A rectilinear control volume (or tank) consists of two different porous media layers and is closed along

all but the upper boundary. This upper boundary in turn contains a source of negatively-buoyant fluid that falls in the form of a laminar plume. We invoke the Boussinesq approximation, valid for modest density differences, according to which our results apply equally well to a buoyant rising plume. After falling a vertical distance H_1 , the plume encounters the interface between the upper and lower layers and thereafter its motion, and the consequent dispersion of contaminated fluid, depends upon the permeability, k_2 , of the lower layer. If $k_2 > k_1$ where k_1 is the permeability of the upper layer, then plume fluid easily descends to the bottom of the control volume (figure 4.1 a). Contrarily, when $k_2 < k_1$, the plume fluid splits in two with some fraction flowing horizontally in the form of a “leaky” interfacial gravity current and the remaining fraction propagating directly into the lower layer.

Predicting the fraction of the plume that detrains along the interface as a function of k_1/k_2 and the source conditions is a complicated task. Nonetheless, helpful insights into the flow behaviour can be realized using comparatively simple formulas based, in part, on existing plume models. Such models enjoy a rich history dating back to Wooding’s seminal paper wherein he derived an analytical solution for plumes in a Darcy regime, i.e. with Reynolds number $Re \leq \mathcal{O}(10)$. Wooding (1963) further assumed a small Péclet number, i.e. $Pe \ll \mathcal{O}(1)$. His study was subsequently extended to a non-Darcy flow regime by Chen & Ho (1986) and Lai (1991) who respectively considered cases where $Pe \ll \mathcal{O}(1)$ and $Pe \gg \mathcal{O}(1)$. More recently, Sahu & Flynn (2015) returned to Wooding’s Darcy flow formulation but assumed $Pe \gg \mathcal{O}(1)$. Following this line of inquiry, and consistent with the experiments to be described in section 4.3, we likewise consider the flow to be in a Darcy regime with $Pe \gg \mathcal{O}(1)$. Where needed (see section 4.4), Sahu & Flynn’s formulas may therefore be employed.

As indicated schematically in figure 4.1 b, fluid detrained from the plume at the interface (and also at the bottom of the control volume) form gravity currents that propagate left and right. Gravity current flow through a free medium but over a porous base has been studied by several researchers e.g. Thomas *et al.* (1998), Ungarish & Huppert (2000) and Spannuth *et al.* (2009). The problem

at hand draws insights from these helpful investigations but more properly falls into the category of gravity current flow in porous medium over a low permeability substrate, which was first studied analytically by Pritchard *et al.* (2001). They assumed a constant volume flux source and a lower layer thickness that was much less than the gravity current height. Pritchard *et al.* (2001) found that, after reaching a certain horizontal distance, the gravity current stopped moving forward at which point the influx from behind the gravity current head was balanced by drainage along the gravity current underside. Extending this investigation to lower (and upper) layers of infinite depth, Goda & Sato (2011) presented a numerical solution that specified the forward propagation of the gravity current and the downward motion of the draining fluid as functions of time as well as parameters such as the permeability ratio, k_1/k_2 . Consistent with Pritchard *et al.* (2001), Goda & Sato (2011) found that the gravity current length approaches some maximum value in the long time limit, $t \rightarrow \infty$. This maximum length is given by

$$\check{L}_g = \frac{q_1 \nu}{k_2 g'_1}. \quad (4.1)$$

Here ν is the kinematic viscosity and q_1 and $g'_1 = g \frac{\rho_1 - \rho_\infty}{\rho_\infty}$ are respectively the gravity current volume flux per unit length and reduced gravity. Moreover ρ_1 and ρ_∞ are the dense and far-field ambient fluid densities, respectively. Although the present investigation considers miscible fluids and a confined volume, we employ Goda & Sato's solution in section 4.4 to describe interfacial gravity current propagation until either the gravity current front or the draining fluid reaches a lateral sidewall or the lower boundary, respectively.

The model predictions derived as part of our analysis are compared against analogue laboratory data. Of particular interest are the gravity current run-out length and the timescales required for the contaminated fluid to reach to the point of overflow. These estimates are made with respect to the permeability and height ratios of the lower to upper layers and the source volume flux and reduced gravity.

The rest of the manuscript is organized as follows: section 4.3 outlines the

experimental setup and procedure, image post-processing details and qualitative observations. Corresponding model equations are developed and discussed in section 4.4 and a comparison with laboratory data is given in section 4.5. Finally, section 4.6 presents conclusions and defines topics for future work.

4.3 Experimental technique

4.3.1 Laboratory set-up and experiments

Laboratory experiments were performed with the aim of studying, both qualitatively and quantitatively, the effects of sudden permeability changes vis-à-vis porous media filling box flows. A schematic of the experimental set-up is shown in figure 4.2. A transparent acrylic tank 88.9 cm long \times 7.6 cm wide \times 50.8 cm tall was filled with tap water of density 0.998 g/cm³ and two layers of Potters Industries A Series Premium glass beads. We considered three different sets of experiments where the ratio of upper (H_1) to lower (H_2) layer depth was 0.5, 1.0 or 2.0. The total depth of both layers, $H = H_1 + H_2$, was always 40 cm. The beads measured either 0.1 cm, 0.3 cm and 0.5 cm in diameter, which yielded permeability ratios, k_1/k_2 , of 0.04, 0.11, 0.36, 2.77, 9.0 and 25.0. Permeabilities were calculated using the relationship originally derived by Rumpf & Gupte (1973), and described in Dullien (1992), such that $k = \frac{d^2 \phi^{5.5}}{5.6}$ where d is the bead diameter and ϕ is the porosity. Following Happel & Brenner (1991), we assume $\phi = 0.38$ corresponding to randomly distributed spherical beads. Note that, in the immediate vicinity of the interface and because of the bidisperse nature of the distribution, a reduction of porosity to $\phi \simeq 0.34$ was anticipated (Schulze *et al.*, 2015).

The plume source fluid consists of salty water to which Procion MX Cold Water dye has been added for purposes of flow visualization. Before the start of an experiment, this fluid was mixed in a 100 L reservoir (see figure 2). The dense fluid in question was then supplied to the rectangular acrylic tank using a hydraulic pump, overhead bucket, flowmeter, flow valves and a line nozzle. The overhead bucket had a cylindrical internal weir which helped to maintain a constant source

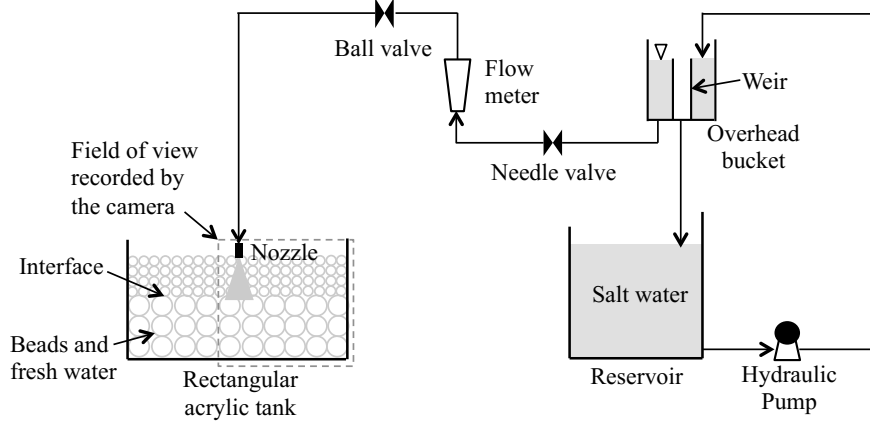


Figure 4.2: Schematic of the experimental setup.

pressure. A Gilmont GV-2119-S-P flowmeter was used to measure the flow rate, which was adjusted using ball and needle valves. The last component of the flow system before dense fluid reached the tank was a line nozzle of discharge area $A_{\text{nozzle}} = 2.8 \text{ cm}^2$, which was fitted at the top centre of the tank and spanned the tank width. The nozzle, which is further described in Roes (2014), was designed so as to minimize the momentum of the exiting fluid.

Experimental images were captured every 60 s using a Canon Rebel EOS T2i 18.0 PM camera fitted with an 18-55 mm IS II zoom lens. The experiments usually lasted between 1 h and 3 h depending upon the flow rate and permeability ratio. Thus, over the course of a single experiment, roughly 60 to 200 images were recorded. Because of the symmetric nature of the flow, and so as to reduce parallax errors, only one half of the experimental tank was visualized. The tank was backlit using a 3M 1880 overhead projector and its backside was covered with tracing paper, which acted to diffuse the light from this projector.

As summarized in Appendix E, a total of 50 experiments were performed where we regard k_1/k_2 , H_1/H_2 , the plume source volume flux, Q_0 , and reduced gravity, g'_0 , as independent variables. Here $g'_0 = g \frac{\rho_0 - \rho_\infty}{\rho_\infty}$ where ρ_0 is the source fluid density.

4.3.2 Experimental images

Experimental images were post-processed using Matlab. Images were first cropped then converted from RGB to grey-scale. They were then subtracted from a reference image taken just before the beginning of an experiment. This subtraction operation helped to highlight differences between ambient (clear) fluid and dense (dyed) fluid whether within the plume or discharged in the form of a deepening layer along the bottom of the tank. Regions uncontaminated by dense fluid therefore have an intensity of zero and appear as black in the figures to follow.

Low permeability layer on top of high permeability layer: experiments with $k_1/k_2 < 1$

Figure 4.3 shows post-processed experimental images for all six permeability ratios considered in this study. In each case, images are collected 1000 s after the descending plume is “switched on.” For the first three cases where $k_1/k_2 < 1$, the flow behaviour is qualitatively similar to the case of a uniform porous medium (Sahu & Flynn, 2015, figure 6). The dense plume flows with comparative ease into the lower layer, and subsequently produces a pair of laterally propagating gravity currents, followed by a deepening layer of discharged plume fluid. The depth of this lower layer is described in terms of the average elevation of the “first front,” the fluid interface separating the dense lower layer from the ambient upper layer. First front elevations were determined using the maximum gradient algorithm developed by Roes (2014) and subsequently employed by Roes *et al.* (2014) and Sahu & Flynn (2015). By measuring the first front elevation and its time derivative, it was straightforward to estimate the advection speed as a function of time. Consequently the time required by the first front to reach the interface and then the nozzle was calculated. Further quantitative details, e.g. showing the filling box time vs. k_1/k_2 , H_1/H_2 etc., are presented in section 4.4.1.

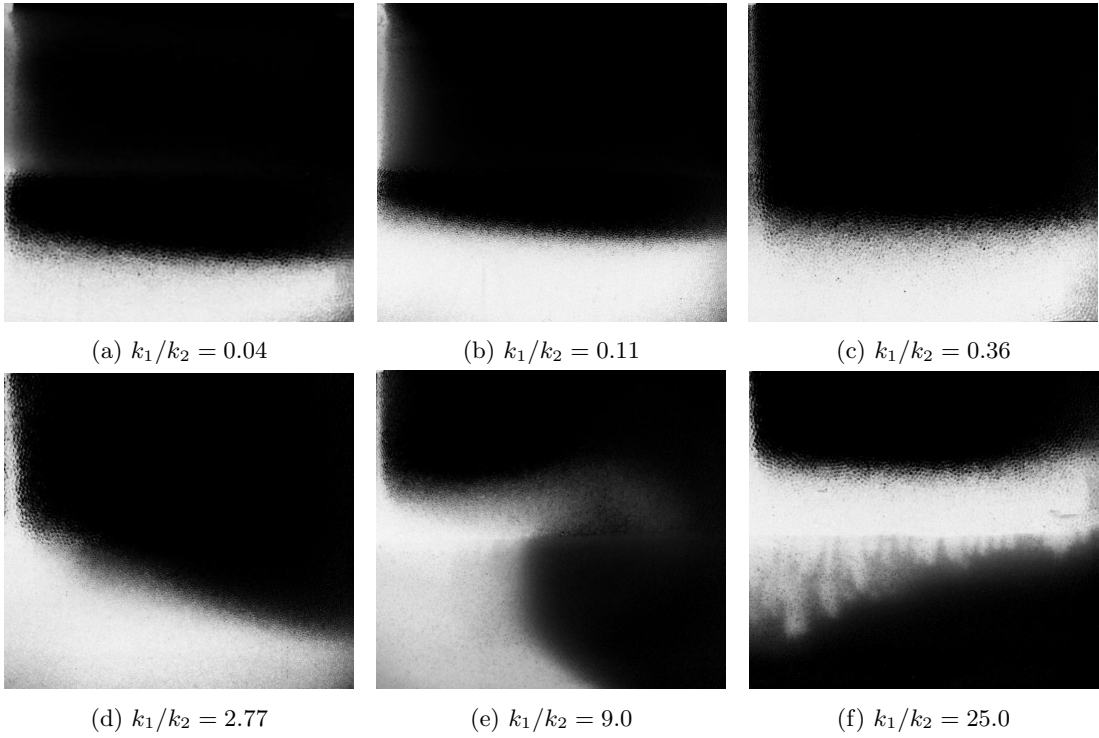


Figure 4.3: Sample images of experiments with $Q_0 = 0.75 \text{ cm}^3/\text{s}$, $g'_0 = 80.0 \text{ cm}/\text{s}^2$ and $H_1/H_2 = 1.0$ at $t = 1000 \text{ s}$. Permeability ratios are as indicated. In sequence, the images belong respectively to Experiments 19, 22, 27, 31, 35 and 40 from table E.2, Appendix E. The field of view for each image measures 44 cm long \times 40 cm tall.

High permeability layer on top of low permeability layer: experiments with $k_1/k_2 > 1$

In cases where $k_1/k_2 > 1$ (i.e. figures 4.3 d,e,f), we observe qualitatively different flow dynamics from cases where $k_1/k_2 < 1$. To wit, some fraction of the plume detrains along the interface and forms a pair of (primary) gravity currents that propagate in the tank interior. The remaining fraction of the plume drains down into the lower layer. Because the horizontal length of the primary gravity current (at $x = H_1$) is significantly larger than that of the line nozzle (at $x = 0$), the former works as a distributed source of dense fluid at the interface for the lower layer, contrary to the latter that works as a discrete source for the upper layer. Note that in a discrete source, mixing occurs via entrainment from the sides whereas in case of distributed source the mixing process is more complicated in that it results from a Rayleigh-Taylor-type instability. The draining fluid from this distributed source eventually reaches the tank bottom where it ultimately forms a pair of secondary gravity currents (see figure 4.3 e). As k_1/k_2 increases, so too does the relative flow resistance in the lower layer and the fraction of plume fluid detrained along the interface. However, as indicated by (4.1), there exists a primary gravity current run-out length \check{L}_g . Once the front travels this horizontal distance, the volume flux of fluid that drains from the gravity current underside matches that detrained from the plume at the level of the interface, H_1 . Consistent with the above remarks, \check{L}_g increases with k_1/k_2 . Figure 4.3 f shows that when the permeability ratio is large, i.e. $k_1/k_2 = 25$, \check{L}_g exceeds the tank half-length, L . In this case, the primary gravity currents reach the sidewalls and start advecting upward well before the lower layer is filled with contaminated fluid. In other words, when $\check{L}_g > L$ plume fluid detrained at $z = H_1$ advects upwards much more quickly than it drains into the (tight) lower layer; the lower layer therefore becomes effectively isolated. Consequently, by the time of control volume overflow, only a small amount of dense fluid has permeated into the lower layer, a scenario that becomes more pronounced with decreasing H_1/H_2 whereby the time required to fill the upper layer decreases. For an effective filling of the entire control volume with dense fluid, it is, irrespective of H_1/H_2 , advantageous

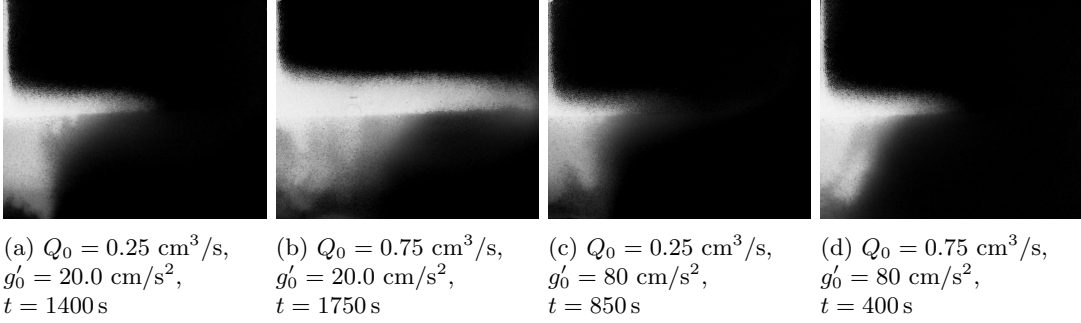


Figure 4.4: Sample images of experiments with $k_1/k_2 = 9.0$ and $H_1/H_2 = 1.0$ at the approximate time instants when the draining fluid first reaches the lower impermeable boundary. In sequence, the images belong respectively to Experiments 32, 33, 34 and 35 from table E.2, Appendix E. The field of view for each image measures 44 cm long \times 40 cm tall.

for $\check{L}_g < L$ as in figures 4.3 d,e.

Because the inflow conditions for the primary gravity currents are prescribed by the outflow conditions of the plume at the interface, the primary gravity current behaviour also depends on the source parameters, i.e. Q_0 and g'_0 , as well as k_1/k_2 and H_1/H_2 . Figure 4.4 shows experimental images collected at the approximate time instants when the draining fluid first reaches the lower boundary. The source conditions represent different permutations of $Q_0 = 0.25, 0.75 \text{ cm}^3/\text{s}$ and $g'_0 = 20, 80 \text{ cm}/\text{s}^2$, whereas $H_1/H_2 = 1.0$ and $k_1/k_2 = 9.0$. Thus we compare in the different panels of figure 4.4 the gravity current length, L_g , against Q_0 and g'_0 for the same mean depth, \bar{b} , of the draining fluid. Consistent with (1), L_g increases with increasing Q_0 and decreasing g'_0 . For fixed Q_0 , larger L_g (and hence \check{L}_g) signifies a smaller fraction of plume fluid propagating into the lower, less permeable layer.

Figure 4.5 depicts gravity current flows for the same Q_0 , g'_0 and k_1/k_2 , but various H_1/H_2 , namely 0.5, 1.0 and 2.0. Owing to the influence of ambient entrainment into the plume, L_g increases as the depth of the upper layer (and hence H_1/H_2) increases. Additional quantitative details relevant to this observation will be provided in section 4.4.

Note finally that the draining flow, particularly that of figure 4.3 f, is typically characterized by fingering patterns, which are indicative of a Rayleigh-Taylor-

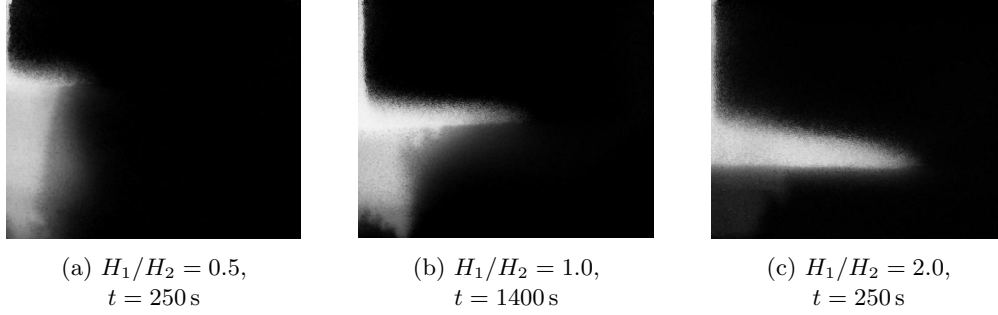


Figure 4.5: Sample images of experiments with $Q_0 = 0.25 \text{ cm}^3/\text{s}$, $g'_0 = 30.0 \text{ cm}/\text{s}^2$ and $k_1/k_2 = 9.0$ at the approximate time instants when the draining fluid reaches the lower impermeable boundary. Height ratios are as indicated. In sequence, the images belong respectively to Experiments 9, 32 and 48 from tables E.1, E.2 or E.3, Appendix E. The field of view for each image measures 44 cm long \times 40 cm tall. (Note that in last image the lower layer appears to be completely dark, which is however not the case. Because of the smaller reduced gravity of the draining fluid compared to panels (a) and (b), the draining fluid is visible only through magnification and/or image thresholding.).

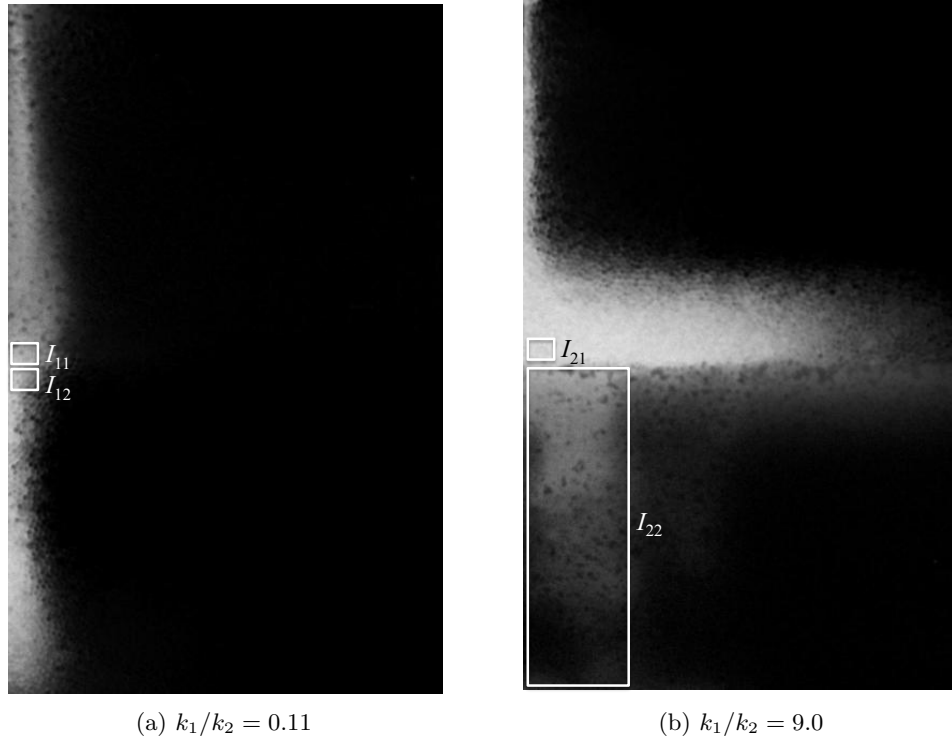


Figure 4.6: Sample images of experiments with $Q_0 = 0.30 \text{ cm}^3/\text{s}$, $g'_0 = 50.0 \text{ cm}/\text{s}^2$ and $H_1/H_2 = 1.0$ at the approximate time instants when the dense fluid reaches the lower impermeable boundary. Permeability ratios are as indicated. In sequence, the images belong respectively to Experiments 23 and 36 from table E.2, Appendix E. The field of view for each image measures 22 cm long \times 40 cm tall.

type instability (Saffman & Taylor, 1958; Homsy, 1987; Drazin & Reid, 2004). Because of the mixing associated with the downwards propagation of these fingers, pixel intensities tend to be depressed beneath the interface as compared to the brighter pixels seen behind the front of the primary gravity current. Dye concentration can be taken as a surrogate for salinity, therefore, we likewise expect that the contaminated fluid below the interface is generally less dense than that above the interface. However, because the tank is backlit and the images are recorded from the front, the image intensity must also depend upon the local bead diameter. Therefore to make a more definitive statement regarding the entrainment of ambient fluid into the draining fluid, it is necessary to consider bead diameter effects. In this spirit, figures 4.6 a and b show snapshots of post processed experimental images from two separate experiments where the beads in the upper and lower layers are flipped, such that $k_1/k_2 = 0.11$ in panel (a) and $k_1/k_2 = 9.0$ in panel (b). All other parameters were kept the same between the two experiments. In panel (a), we assume that the entrainment in the immediate neighbourhood of the interface is small enough that the reduced gravity just above and below the interface is effectively the same. Thus the difference in the spatial-average intensities, $I_{12} - I_{11}$, of the two boxes shown in panel (a) is primarily as a result of the difference of bead diameter. Of course in panel (b) the situation is more complicated because the intensity difference $I_{21} - I_{22}$ arises both because of the difference of bead diameter as well as the aforementioned entrainment. Provided $I_{21} - I_{22} > I_{12} - I_{11}$ and assuming a linear variation between pixel intensity and fluid density, the mean reduced gravity, g'_{2B} , of the lower layer relative to the reduced gravity, g'_1 , of the upper layer can be estimated from

$$g'_{2B} = g'_1 \left(\frac{I_{22} + I_{12} - I_{11}}{I_{21}} \right). \quad (4.2)$$

For the parameters relevant to figure 4.6, $g'_{2B}/g'_1 = 0.43$: vertical mixing is obviously less dramatic than in the analogue turbulent case devoid of porous media, but its influence here is nonetheless palpable. Unfortunately, our efforts to further quantify the extent of mixing were frustrated poor measurement repeatability. Not surprisingly, we found that g'_{2B}/g'_1 depends on g'_0 and, to a lesser extent, Q_0 .

However, even for the images of a single experiment, we found that the magnitude of g'_{2B}/g'_1 can vary significantly depending on frame number and the size of the interrogation window. Wishing to avoid a lengthy, and ultimately tangential, discussion of this topic, we defer to future studies a detailed investigation of the influence of the source and medium parameters and other factors on g'_{2B}/g'_1 .

Horizontal time series for measuring gravity current propagation

Post-processed images were assembled to make movies using Matlab's `immovie` command. Horizontal time series (HTS) images of the type shown in figure 4.7 d,e,f were then constructed. They show the time variation of pixel intensity along a particular horizontal line within the field of view. In the HTS images, light and dark regions correspond, respectively, to regions occupied by discharged plume fluid and ambient fluid. The boundaries between the light and dark regions therefore denote the front position of the primary (figure 4.7 d) and secondary (figure 4.7 f) gravity current against time, which is here non-dimensionalized by the residence time, defined by

$$t_0 = \frac{2\phi\Lambda LH}{Q_0}. \quad (4.3)$$

The primary gravity current is first apparent shortly after the time, $t = 0$, when the plume is switched on. (Note that for the quantitative analysis to be presented in section 4.4, we assume $t = 0$ when the dense plume first reaches either the lower impermeable boundary or the interface, for $k_1/k_2 \leq 1$ or $k_1/k_2 > 1$, respectively). Until the time instant, t_1 , when the draining fluid first reaches the bottom boundary, the primary gravity current propagates with a large (nearly-constant) velocity, which drops to a much smaller value as L_g reaches \check{L}_g . The gravity current then maintains roughly the same length \check{L}_g until $t = t_2$, i.e. when the secondary gravity current, formed just after t_1 , reaches the right sidewall. Discharged plume fluid then steadily accumulates in the lower layer and the primary gravity current again advances along the interface. Finally at $t = t_3$ the lower layer becomes completely filled with contaminated fluid.

To experimentally measure \check{L}_g , we consider the flow dynamics only until t_1 ,

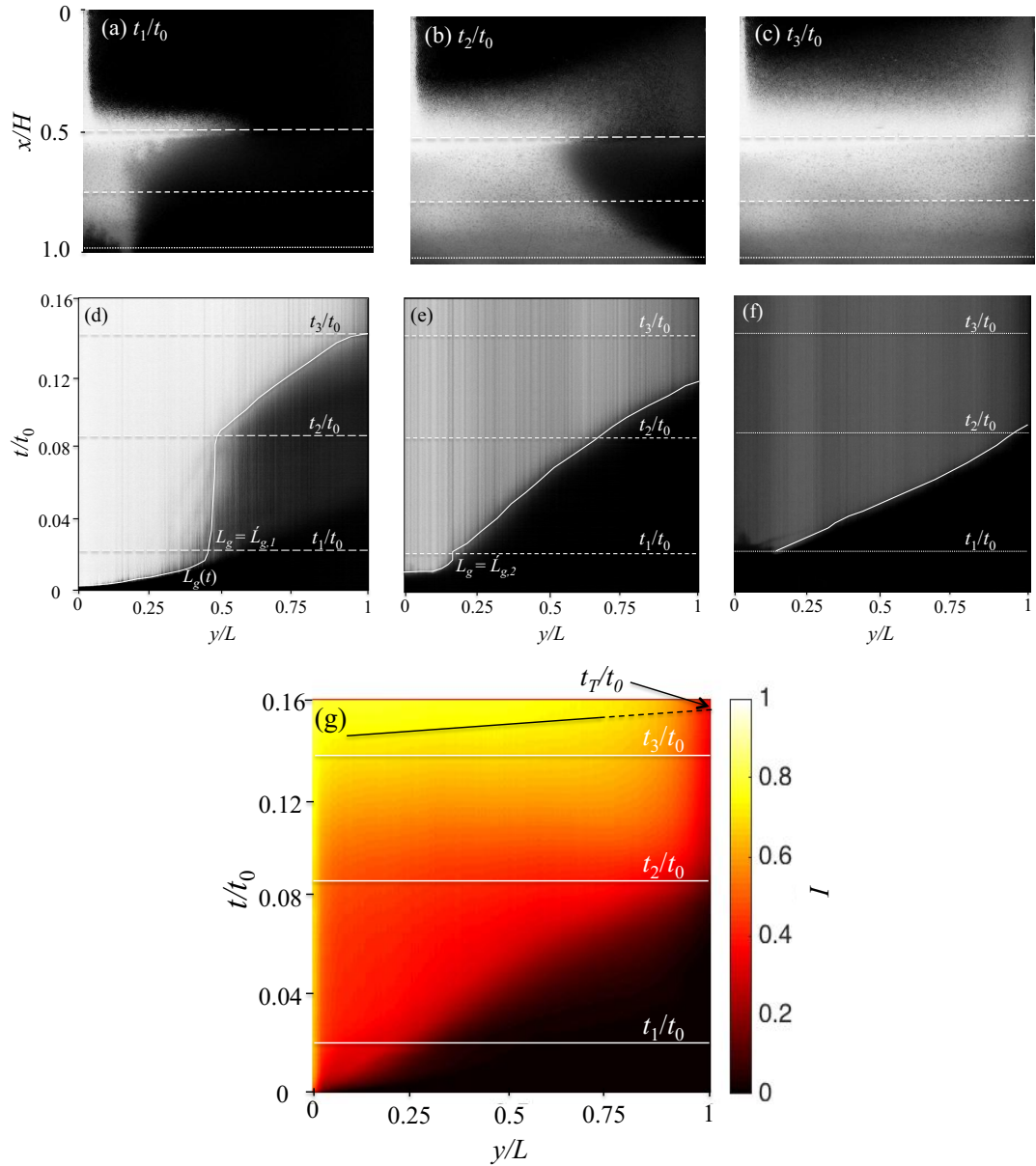


Figure 4.7: [Colour online] Images showing examples of horizontal (HTS) and composite (CTS) time series images. HTS images are collected along the interface (panel d corresponding to the long-dashed lines in panels a, b and c), at a depth $H_2/2$ below the interface (panel e corresponding to the dashed lines in panels a, b and c) and close to the bottom of the tank (panel f corresponding to the dotted lines in panels a, b and c). The associated timescale t_0 is defined in (4.3). Images belong to Experiment 32 from table E.2, Appendix E, for which the experimental parameters read $Q_0 = 0.25 \text{ cm}^3/\text{s}$, $g'_0 = 20.0 \text{ cm/s}^2$, $k_1/k_2 = 9.0$ and $H_1/H_2 = 1.0$.

i.e. when the flow is not yet influenced by the finite boundaries of the experimental tank. From figures 4.7 d and 4.7 e, and in contrast to figure 2 of Goda & Sato (2011), we find that experimental estimates for \check{L}_g vary considerably depending on whether measurements are made at or below the interface. For purposes of comparing the measured and predicted values of \check{L}_g in section 4.5, we restrict attention to laboratory estimates derived from figures such as figure 4.7 e. The rationale for this choice shall become obvious in section 4.4.2.

Composite time series (CTS) for measuring filling box time

In experiments where $k_1/k_2 < 1$, a single sharp nearly-horizontal boundary appears between the ambient fluid and that discharged from the plume (see figures 4.3 a,b,c). Therefore and by using the interface detection algorithm described in section 4.3.2, it is straightforward to measure the time required for this first front to reach the point of overflow. However, when $k_1/k_2 > 1$, figures 4.3 d,e,f suggest a more convoluted boundary between ambient and contaminated fluid. Because it is oftentimes difficult to unambiguously identify a first front or to measure its vertical velocity directly from snapshot images, we choose instead to focus attention on a composite time series (CTS). The algorithm for constructing these images is similar to that of section 4.3.2 but replaces, for each time instant, the intensity at a particular pixel with the column-average pixel intensity in the interval $0 < x < H$ (Nicholson & Flynn, 2015). A sample CTS image is shown in figure 4.7 g. The horizontal lines labeled as t_1/t_0 , t_2/t_0 and t_3/t_0 correspond to the snapshot images shown in panels (a), (b) and (c), respectively. The intensity index, I , which appears in the colorbar on the right hand side of the CTS image, and which ranges from 0 to 1, is a surrogate for the fraction of discharged plume fluid contained within a particular column of pixels. From (3.1) of Shin *et al.* (2004), and assuming again that the fluid density scales in proportion to dye concentration, a formula for I can be given as

$$I(y, t) = \frac{1}{H} \int_0^H \frac{\rho(y, x, t) - \rho_\infty}{\rho_0 - \rho_\infty} dx, \quad (4.4)$$

where $\rho(y, x, t)$ is the fluid density at any location (y, x) for a particular time, t . Thus, a value of $I = 0$ or 1 indicates, respectively, the presence of only ambient fluid or only source fluid. The latter value is, of course, never realized: because of the entrainment of ambient fluid into the plume, I remains strictly less than unity.

Once the dense fluid reaches the point of overflow, the time rate of increase in the average fluid density becomes much smaller than at early times. Therefore, (4.4) suggests that at large times the image intensity I should become nearly uniform; figure 4.7 g with $y/L \nearrow 1$ indeed displays this behaviour. In the region close to the sidewall, the lower image intensity is due to sidewall effects, which allow light from the projector to enter the tank without first passing through those beads adjacent to the back surface of the tank. In figure 4.7 g the solid black diagonal line shows the times beyond which the time rate of change of pixel intensity becomes suitably small. Meanwhile the dashed line indicates the extension of this solid black line to the point $y/L = 1$. This point of intersection defines the time for overflow, which we label as t_T .

4.4 Theoretical development

Over $0 < x \leq H_1$, the dense plume behaves like in an uniform porous medium and we can therefore use the formulas presented in Sahu & Flynn (2015) for estimating key parameters of interest, i.e. the plume volume flux, $Q(x)$, and reduced gravity, $g'(x)$, averaged over the plume cross-section. The associated equations respectively read

$$\begin{aligned} Q(x) &= \left[\left(\frac{16F_0 k_1 \Lambda}{\pi \nu} \right)^2 \alpha \phi_1 (x + x_0) \right]^{1/4}, \\ g'(x) &= \left[\left(\frac{\pi F_0 \nu}{16 k_1 \Lambda} \right)^2 \frac{1}{\alpha \phi_1 (x + x_0)} \right]^{1/4}. \end{aligned} \quad (4.5)$$

Here, F_0 is the source buoyancy flux, Λ is the line source width, ν is the fluid viscosity, ϕ_1 is the porosity of the upper layer and α is the dispersivity constant, which was measured experimentally by Sahu & Flynn (2015) and equals 0.015 cm

provided $Re \leq \mathcal{O}(10)$ and $Pe \gg \mathcal{O}(1)$. Furthermore, x_0 represents a virtual origin correction that accounts for the finite source volume flux $Q_0 (> 0)$ of the (non-ideal) plume; x_0 is given by

$$x_0 = \frac{1}{\alpha\phi_1} \left(\frac{\pi\nu}{16F_0k_1\Lambda} \right)^2 Q_0^4. \quad (4.6)$$

Re-iterating from Chapter 2, (4.5) shows that the volume flux of the dense falling plume increases with the increasing distance from the source. This increase occurs as a result of the entrainment of external fluid into the falling plume. For the same reason, the reduced gravity decreases as source fluid moves away from the source. Moreover, the virtual source location, x_0 , in (4.6) indicates that the volume flux at the source cannot be zero in case of real plumes.

From (4.5), we can easily calculate the volume flux, Q_1 , and mean reduced gravity, g'_1 , of the plume at the interface by setting $x = H_1$. Thus

$$\begin{aligned} Q_1 &= \left[\left(\frac{16F_0k_1\Lambda}{\pi\nu} \right)^2 \alpha\phi_1(H_1 + x_0) \right]^{1/4} \quad \text{and} \\ g'_1 &= \left[\left(\frac{\pi F_0\nu}{16k_1\Lambda} \right)^2 \frac{1}{\alpha\phi_1(H_1 + x_0)} \right]^{1/4}. \end{aligned} \quad (4.7)$$

The above results help to specify the inflow conditions for the lower layer plume and the primary gravity current, the latter of which appears only when $k_1/k_2 > 1$.

4.4.1 Permeability ratio $k_1/k_2 < 1$

When the dense plume enters a lower layer having permeability $k_2 > k_1$, the qualitative nature of the (primarily vertical) flow remains the same. To describe the lower layer plume quantitatively, we need to introduce a second virtual origin, x_1 , whose magnitude depends on Q_1 , i.e.

$$x_1 = \frac{1}{\phi_2\alpha} \left(\frac{\pi\nu}{16F_0k_2\Lambda} \right)^2 Q_1^4 = \frac{\phi_1}{\phi_2} \left(\frac{k_1}{k_2} \right)^2 (H_1 + x_0). \quad (4.8)$$

Then by adapting (4.5), we can predict the plume volume flux and reduced gravity as functions of x in the lower layer. Thus

$$\begin{aligned} Q(x) &= \left[\left(\frac{16F_0k_2\Lambda}{\pi\nu} \right)^2 \alpha\phi_2(x - H_1 + x_1) \right]^{1/4}, \\ g'(x) &= \left[\left(\frac{\pi F_0\nu}{16k_2\Lambda} \right)^2 \frac{1}{\alpha\phi_2(x - H_1 + x_1)} \right]^{1/4}, \end{aligned} \quad (4.9)$$

for $H_1 < x \leq H$. Here $H = H_1 + H_2$ is the control volume height. These results can easily be extended to calculate Q_2 and g'_{2A} , the respective values of the plume volume flux and reduced gravity at the bottom of the control volume, i.e.

$$\begin{aligned} Q_2 &= \left[\left(\frac{16F_0k_2\Lambda}{\pi\nu} \right)^2 \alpha\phi_2(H_2 + x_1) \right]^{1/4}, \\ g'_{2A} &= \left[\left(\frac{\pi F_0\nu}{16k_2\Lambda} \right)^2 \frac{1}{\alpha\phi_2(H_2 + x_1)} \right]^{1/4}. \end{aligned} \quad (4.10)$$

After the dense plume reaches this bottom boundary, its subsequent horizontal motion can be described using the equations for gravity current flow through a porous medium. Employing the equations of Sahu & Flynn (2015), which are themselves based on the seminal analysis of Huppert & Woods (1995), it can be shown that the gravity current front speed is given by

$$v_g = \frac{2\lambda}{3} \left(\frac{q_2 S_2}{t} \right)^{1/3}. \quad (4.11)$$

Here $q_2 = \frac{Q_2}{2\Lambda}$ and $S_2 = \frac{k_2 g'_{2A}}{\nu \phi_2}$. Moreover, $\lambda = 2.046$ represents the dimensionless position of the leading edge of the gravity current. Consistent with Sahu & Flynn (2015), we assume that the time scale associated with plume flow is much smaller than that of either the horizontal motion of the gravity current or the vertical motion of the first front, the latter of which is considered below. This assumption is valid provided $L/H \geq \mathcal{O}(1)$. On this basis, $t = 0$ corresponds to the time instant when the dense plume first reaches the bottom of the control volume.

On further simplification, and recalling that the buoyancy flux, $F_0 = Q_0 g'_0 =$

$Q(x)g'(x)$, is conserved, (4.11) yields

$$v_g = \frac{2\lambda}{3} \left(\frac{F_0 k_2}{2\Lambda\nu\phi_2 t} \right)^{1/3}. \quad (4.12)$$

The time required for the gravity current to reach the sidewall is therefore

$$t_L = \left[\left(\frac{L}{\lambda} \right)^3 \frac{1}{q_2 S_2} \right]^{1/2} = \left[\left(\frac{L}{\lambda} \right)^3 \frac{2\Lambda\nu\phi_2}{F_0 k_2} \right]^{1/2}. \quad (4.13)$$

Because the plume buoyancy flux is independent of x , v_g and t_L are independent of H and, for that matter, Q_0 . Note finally that at $t = t_L$, the mean height of the gravity current is given by

$$\bar{h}_{t_L} = \frac{1}{\lambda} \left(\frac{q_2^2 t_L}{\phi_2^3 S_2} \right)^{1/3}. \quad (4.14)$$

Because \bar{h}_{t_L} separately depends on Q_2 (through q_2) and g'_{2A} (through S_2), this mean height does depend on H , unlike v_g and t_L .

After reaching the sidewalls, the discharged dense fluid forms a deepening layer of contaminated fluid whose upper boundary, termed the first front by Baines & Turner (1969), begins advecting upwards. The motion of the first front can again be determined based on the analysis of Sahu & Flynn (2015). However, and relative to the rising first front, there appears a sudden decrease of permeability at height $\bar{h} = H_2$, measured from the bottom of the tank. Consequently, the timescales associated with the motion of the first front need to be defined separately in the lower and upper layers.

In the lower layer, at $t = t_L$, the curvature of the first front is dictated by the shape of the gravity current at the time instant when it collides with the lateral sidewall. In other words, the initial mean elevation of the first front is given by (4.14). If t_{H_2} is the time required for the first front to subsequently advect to the interface, we then require a formula for the mean height, \bar{h} , of the first front over $t_L < t < t_L + t_{H_2}$. The expression in question reads

$$\bar{h} = H_2 + x_1 - \left[(H_2 + x_1 - \bar{h}_{t_L})^{3/4} - \frac{3(t - t_L)}{4A} \left(\frac{16F_0 k_2 \Lambda \alpha^{1/2}}{\pi\nu\phi_2^{3/2}} \right)^{1/2} \right]^{4/3}. \quad (4.15)$$

This result is valid up to the point where $\bar{h} = H_2$ and shows the correct limiting behaviour as $t \rightarrow t_L$ whereby $\bar{h} = \bar{h}_{t_L}$ as specified in (4.14). In the above equation, $A = 2\Lambda L$ is the tank cross-sectional area.

As the first front rises, its curvature decreases, i.e. the first front becomes progressively more horizontal. This levelling process is accelerated close to the interface due to the added flow resistance associated with advection through the upper layer, whose permeability is less than that of the lower layer. Heuristically speaking, it becomes easier for discharged plume fluid to flow outwards than to flow upwards. To a first approximation, we therefore assume that the first front is horizontal as it begins to advect through the upper layer. The strength of this approximation obviously improves with increasing H_2 and decreasing k_1/k_2 . When $t = t_L + t_{H_2}$, $\bar{h} = H_2$, and (4.15) therefore yields

$$t_{H_2} = \frac{4}{3}A \left(\frac{\pi\nu\phi_2^{3/2}}{16F_0k_2\Lambda\alpha^{1/2}} \right)^{1/2} \left[(H_2 + x_1 - \bar{h}_{t_L})^{3/4} - x_1^{3/4} \right]. \quad (4.16)$$

By extension, the counterpart of (4.15) for the upper layer reads

$$\bar{h} = H + x_0 - \left[(H + x_0 - H_2)^{3/4} - \frac{3}{4} \frac{(t - t_L - t_{H_2})}{A} \left(\frac{16F_0k_1\Lambda\alpha^{1/2}}{\pi\nu\phi_1^{3/2}} \right)^{1/2} \right]^{4/3}. \quad (4.17)$$

Equation (4.17) is valid for $t_L + t_{H_2} < t < t_L + t_{H_2} + t_{H_1}$ where

$$t_{H_1} = \frac{4}{3}A \left(\frac{\pi\nu\phi_1^{3/2}}{16F_0k_1\Lambda\alpha^{1/2}} \right)^{1/2} \left[(H + x_0 - H_2)^{3/4} - x_0^{3/4} \right], \quad (4.18)$$

is the time required for the first front to advect over the vertical distance H_1 . Thus the total time required for the first front to advect to the level of the source is $t_{H_2} + t_{H_1}$.

The variation of \bar{h} vs. t is presented in figure 4.8 for various k_1/k_2 assuming equal upper and lower layer depths. The surface of figure 4.8 shows an obvious kink, which becomes more pronounced as k_1/k_2 decreases; the kink reflects the sudden increase of volume flux experienced by the plume as it enters the lower layer. Of course, the kink disappears in the limit $k_1/k_2 \rightarrow 1$ in which case the porous medium becomes uniform so that the value of H_1/H_2 is irrelevant.

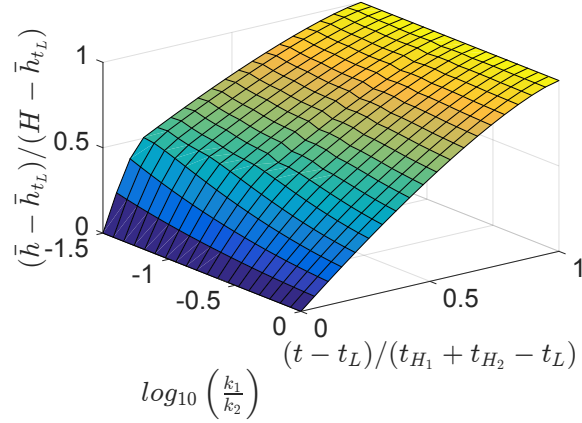


Figure 4.8: [Colour online] Variation of \bar{h} with time and k_1/k_2 for $H_1/H_2 = 1$ (see equations 4.15–4.18).

For the purposes of further comparing the above results with the uniform porous medium case, let us assume that the control volume consists of a uniform porous medium where the permeability and porosity are given by the following depth-weighted average values: $k_m = (H_1 k_1 + H_2 k_2) / (H_1 + H_2)$ and $\phi_m = (H_1 \phi_1 + H_2 \phi_2) / (H_1 + H_2)$. In this case, the time required for the gravity currents to reach the left and right sidewalls is given by

$$t_{L_m} = \left[\left(\frac{L}{\lambda} \right)^3 \frac{2\Lambda\nu\phi_m}{F_0 k_m} \right]^{1/2}. \quad (4.19)$$

Meanwhile the time required for the first front to advect from the bottom to the top of the control volume is given by

$$t_{H_m} = \frac{4}{3} A \left(\frac{\pi\nu\phi_m^{3/2}}{16F_0 k_m \Lambda \alpha^{1/2}} \right)^{1/2} [(H + x_m - \bar{h}_{t_{L_m}})^{3/4} - x_m^{3/4}]. \quad (4.20)$$

Here

$$x_m = \frac{1}{\phi_m \alpha} \left(\frac{\pi\nu}{16F_0 k_m \Lambda} \right)^2 Q_0^4 \quad \text{and} \quad \bar{h}_{t_{L_m}} = \frac{1}{\lambda} \left(\frac{q_2^2 \nu t_L}{\phi_m^2 k_m g'_m} \right)^{1/3}. \quad (4.21)$$

Furthermore, $q_m = Q_m / 2\Lambda$ and g'_m are calculated using the formulas given in (4.10) by replacing k_2 , ϕ_2 , x_1 and H_2 with k_m , ϕ_m , x_m and H , respectively. The dimensionless timescale associated with filling both the upper and lower layers

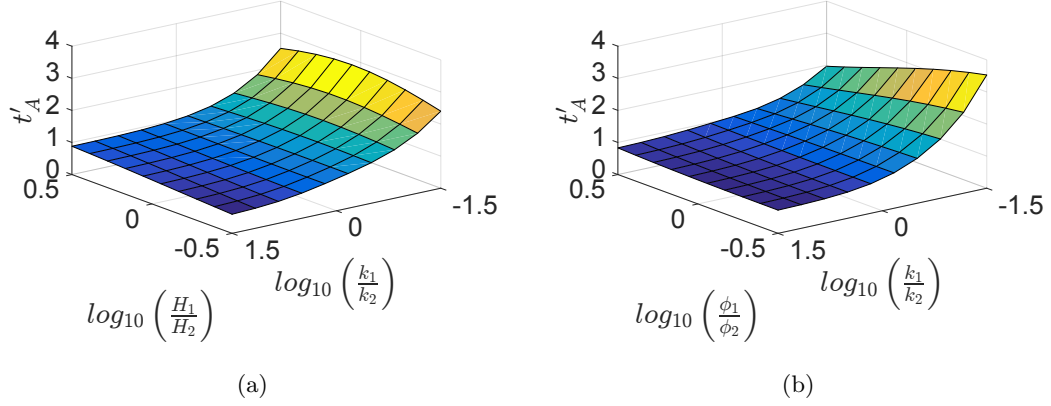


Figure 4.9: [Colour online] Variation of t'_A vs. k_1/k_2 based on (4.23) for (a) various H_1/H_2 with $\phi_1/\phi_2 = 1$, and (b) various ϕ_1/ϕ_2 with $H_1/H_2 = 1$.

can therefore be written as

$$t'_A = \frac{t_L + t_{H_1} + t_{H_2}}{t_{L_m} + t_{H_m}}. \quad (4.22)$$

We now recall that the gravity current solutions, and therefore t_L and t_{L_m} , are obtained presuming sharp interfaces and a constant source volume flux. If \bar{h}_{t_L} and $\bar{h}_{t_{L_m}}$ are respectively removed from (4.16) and (4.20) whereby the details of the gravity current motion are ignored but the first front is presumed to start from the very bottom of the control volume, t_L and t_{L_m} can then be omitted from (4.22). In other words, and with reference to (4.22), equivalent results for t'_A are obtained by ignoring t_L and t_{L_m} , but likewise assuming \bar{h}_{t_L} and $\bar{h}_{t_{L_m}}$ to be zero when computing t_{H_1} and t_{H_m} , respectively. For further simplification, we recall that the flow is in a Darcy regime and therefore assume either a weak non-ideal plume source with $x_0 \ll H_1$ and $x_m \ll H$, or, alternatively, an ideal source with $x_0 = x_m = 0$. In either case, (4.8) shows that $x_1 = \frac{\phi_1}{\phi_2} \left(\frac{k_1}{k_2}\right)^2 H_1$. Then on substituting (4.16), (4.18) and (4.20) into (4.22), it can be shown that

$$t'_A = \frac{\left(1 + \frac{k_1}{k_2} \frac{H_1}{H_2}\right)^{1/2} \left\{ \left(\frac{\phi_1}{\phi_2} \frac{H_1}{H_2}\right)^{3/4} + \left(\frac{k_1}{k_2}\right)^{1/2} \left[\left(1 + \frac{\phi_1}{\phi_2} \left(\frac{k_1}{k_2}\right)^2 \frac{H_1}{H_2}\right)^{3/4} - \left(\frac{\phi_1}{\phi_2} \left(\frac{k_1}{k_2}\right)^2 \frac{H_1}{H_2}\right)^{3/4} \right] \right\}}{\left(\frac{k_1}{k_2}\right)^{1/2} \left(1 + \frac{H_1}{H_2}\right)^{1/2} \left(1 + \frac{\phi_1}{\phi_2} \frac{H_1}{H_2}\right)^{3/4}}. \quad (4.23)$$

The variation of t'_A with k_1/k_2 for various H_1/H_2 and ϕ_1/ϕ_2 are shown in figure 4.9. Although (4.23) is strictly valid when $k_1/k_2 \leq 1$, we extend t'_A to $k_1/k_2 > 1$ for reasons that will become obvious below. In panel (a), where $\phi_1/\phi_2 = 1$, $t'_A = 1$ for all values of H_1/H_2 when $k_1/k_2 = 1$. In this case, there is no difference between the lower and upper layers. By contrast, the porous medium of panel (b) is uniform only when both horizontal axis variables equal unity. In either panel it is observed that t'_A increases as k_1/k_2 decreases: when $k_1/k_2 < 1$, (4.5), shows that the plume volume flux remains very small throughout the upper layer. This has the effect of increasing t_{H_1} significantly as compared to the case where the upper layer permeability is $k_m (> k_1)$. This behaviour is consistent with the time-scales presented in figure 4.8 for $H_1/H_2 = 1$, whereby $t_{H_1} \gg t_{H_2}$ when $k_1/k_2 \ll 1$. Note, moreover, that the surface of panel (a) shows a peak when the upper and lower layers are equal in depth. As H_1/H_2 decreases from unity, the upper layer becomes thinner such that its influence on $t_{H_1} + t_{H_2}$ decreases, which further suggests that $t'_A \approx 1$ as $H_1/H_2 \rightarrow 0$. On the other hand, for $H_1/H_2 > 1$ the difference between k_1 and k_m decreases as does t'_A , which again approaches unity as H_1/H_2 now approaches infinity.

4.4.2 Permeability ratio $k_1/k_2 > 1$

As discussed in section 4.3.2, when the permeability of the lower layer is comparatively small, the plume fluid discharged at the interface takes the form of a porous media gravity current flowing over a porous base having an even lower permeability. While the solution presented by Huppert & Woods (1995) for gravity current flow over an impermeable base has already been used to good effect in section 4.4.1, we adopt Goda & Sato (2011)'s methodology in approaching the current problem. An important difference between our work and theirs is that we consider a control volume with closed boundaries whereas their two-layer porous medium was infinite in extent. Their solutions are therefore only applicable until the primary gravity current reaches the sidewall and whatever fluid that drains from this gravity current has not yet reached the bottom boundary. Using variables defined in figure 1, we therefore require that $L_g < L$ and $b < H_2$. Thus,

and by assuming a hydrostatic pressure distribution, the governing equation for the primary gravity current height, $h_g(y, t)$, measured relative to the elevation of the interface reads

$$\phi_1 \frac{\partial h_g}{\partial t} = \frac{k_1 g'_1}{\nu} \frac{\partial}{\partial y} \left(h_g \frac{\partial h_g}{\partial y} \right) - w. \quad (4.24)$$

Here $w = w(y, t)$ is the drainage velocity, whose value depends both on the primary gravity current height and the draining fluid depth $b(y, t)$ such that

$$w = \phi_2 \frac{\partial b}{\partial t} = \frac{k_2}{\nu} \left(\frac{g'_{2_B} b + g'_1 h_g}{b} \right). \quad (4.25)$$

Note that g'_1 and g'_{2_B} are the mean reduced gravity of the gravity current and the draining fluid, respectively. The experimental images of section 4.3 (i.e. figures 4.3f, 4.4 and 4.6) suggest that g'_1 and g'_{2_B} are different, however, for analytical tractability we apply the same sharp interface approximation used by Goda & Sato (2011) whereby mixing and entrainment are assumed small. Thus $g'_{2_B} = g'_1$, in which g'_1 is defined in (4.7). The validity of this approximation is further discussed below. Setting $g'_{2_B} = g'_1$, (4.25) simplifies to

$$w = \phi_2 \frac{\partial b}{\partial t} = \frac{k_2 g'_1}{\nu} \left(1 + \frac{h_g}{b} \right). \quad (4.26)$$

Equations (4.24) and (4.26) are subject to the following boundary conditions

$$\frac{k_1 g'_1}{\nu} h_g \frac{\partial h_g}{\partial y} = -q_1 \quad \text{and} \quad h_g(L_g(t), t) = b(L_g(t), t) = 0, \quad (4.27)$$

where $q_1 = \frac{Q_1}{2\Lambda}$ is the plume volume flux per unit length at the interface. Furthermore h_g and b must also satisfy an expression of global volume conservation such that

$$\int_0^{L_g(t)} [\phi_1 h_g(y, t) + \phi_2 b(y, t)] dy = q_1 t. \quad (4.28)$$

In contrast to the discussion of section 4.4.1, we now assume that $t = 0$ corresponds to the instant in time when the plume first reaches the interface.

As b progressively increases, the primary gravity current stops moving forward as the influx of dense plume fluid becomes balanced by fluid draining from the gravity current underside (Goda & Sato, 2011). In other words, as time

progresses, $\frac{h_g}{b}$ becomes small and $L_g(t) \rightarrow \check{L}_g$, where \check{L}_g is defined by (4.1). Consequently, or by a trivial rearrangement of (4.1),

$$q_1 = \check{L}_g w = \check{L}_g \frac{k_2 g_1'}{\nu}. \quad (4.29)$$

Furthermore, as $L_g(t) \rightarrow \check{L}_g$, Goda & Sato (2011) suggest that the gravity current height varies linearly with y . Converting their non-dimensional height profile, i.e. given in (3.20) of Goda & Sato (2011), into dimensional form yields

$$\check{h}_g = \left(\frac{k_2}{k_1}\right)^{1/2} (\check{L}_g - y) \quad \Rightarrow \quad \check{h}_g = \left(\frac{k_2}{k_1}\right)^{1/2} \frac{\check{L}_g}{2}, \quad (4.30)$$

where \check{h}_g is the mean gravity current height associated with the run-out length of \check{L}_g . The corresponding time instant, \check{t} , cannot be determined exactly from Goda & Sato (2011): their figure 2 shows that the run-out length is approached asymptotically. For the present purposes, therefore, we associate \check{t} with the moment when $L_g = 0.9\check{L}_g$ ¹. On this basis, and using data from Goda & Sato's figure 3 a, it can be shown that

$$\check{t} = \frac{9.8q_1}{\phi_1 S_1^2} \left(\frac{k_1}{k_2}\right)^{3/2}. \quad (4.31)$$

At this time instant, the mean draining fluid depth is \check{b} . To determine the value of \check{b} , we use (4.28) and infer that

$$\check{b} = \frac{1}{\phi_2} \left[\frac{q_1 \check{t}}{\check{L}_g} - \phi_1 \left(\frac{k_2}{k_1}\right)^{1/2} \frac{\check{L}_g}{2} \right], \quad (4.32)$$

where the latter term incorporates the mean height of the primary gravity current at $t = \check{t}$. Note that the mean draining fluid depth, \bar{b} , continuously increases with time and the corresponding value of \bar{b} at $t > \check{t}$ can be determined by simply replacing \check{t} with t in (4.32).

If $\check{b} < H_2$, the additional time required by the draining fluid to reach the lower impermeable boundary can be estimated from

$$t_{B_1} = \frac{\phi_2 \Lambda \check{L}_g (H_2 - \check{b})}{Q_1}. \quad (4.33)$$

¹While comparing the predicted and measured values of \check{L}_g in section 4.5, we employ the formula presented in (4.1), and therefore the above assumption of $L_g = 0.9\check{L}_g$ does not affect our result.

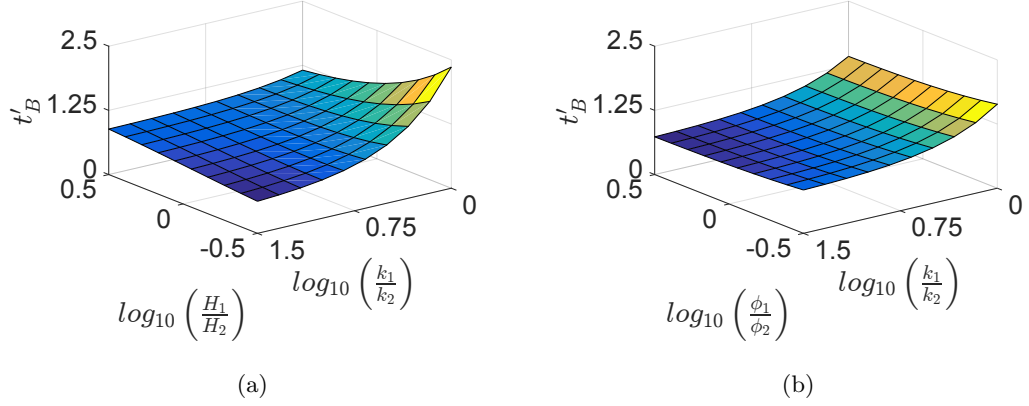


Figure 4.10: [Colour online] Variation of t'_B vs. k_1/k_2 based on (4.36) for (a) various H_1/H_2 with $\phi_1/\phi_2 = 1$, and (b) various ϕ_1/ϕ_2 with $H_1/H_2 = 1$.

Thereafter, a secondary gravity current is formed that fills, from the bottom up, the lower layer with contaminated fluid. Assuming a sharp interface between this contaminated fluid and the overlying ambient, we can infer the time required to fill the remaining part of the lower layer with discharged plume fluid. The corresponding formula reads

$$t_{B_2} = \frac{2\phi_2\Lambda H_2(L - \check{L}_g)}{Q_1}. \quad (4.34)$$

The total time required to fill the lower layer can then be approximated as $t_B = \check{t} + t_{B_1} + t_{B_2}$. However, this estimation is valid only if $\check{L}_g < L$ and $\check{b} < H_2$. In cases where $\check{L}_g < L$ but $\check{b} > H_2$, the total time required to fill the lower layer can instead be estimated by treating the lower layer as its own control volume, where the only inflow is due to the plume at the interface. The formula for the associated time scale reads

$$t_B = \frac{2\phi_2\Lambda LH_2}{Q_1}, \quad (4.35)$$

provided that $H_2 \gg \check{h}_g$ and a sharp interface assumption is valid. Equation (4.35) differs from the prediction for t_{H_2} given by (4.16) in two ways: (i) (4.35) ignores lower layer entrainment whereas (4.16) does not, and (ii) the control volume used in the derivation of (4.35) is the entire lower layer whereas that considered in the analysis leading to (4.16) is the portion of the lower layer below the first front.

After filling the lower layer, the interface between the dense and ambient fluids

is assumed to advect upwards in the form of a first front as shown in figure 4.7 c. Therefore, to simplify the analysis, we proceed by considering a mean first front height, \bar{h} , as defined in (4.17). Equation (4.18) can then be used to estimate the time, t_{H_1} , required to fill the upper layer. Finally the total filling box time for this configuration with $k_1/k_2 > 1$ is given by $t_B + t_{H_1}$.

To find a dimensionless time similar to that given by (4.23), we take the ratio of $t_B + t_{H_1}$ and t_{H_m} , the latter of which is defined by (4.20) where, as with the previous analysis, we assume $\bar{h}_{t_{Lm}} = 0$. After some simplification, it can be shown that

$$t'_B = \frac{\left(1 + \frac{k_1 H_1}{k_2 H_2}\right) \left(\frac{3}{4} + \frac{\phi_1 H_1}{\phi_2 H_2}\right)}{\frac{k_1}{k_2} \left(\frac{\phi_1}{\phi_2}\right)^{1/4} \left(1 + \frac{\phi_1 H_1}{\phi_2 H_2}\right)^{3/4} \left(\frac{H_1}{H_2}\right)^{3/4} \left(1 + \frac{H_1}{H_2}\right)^{1/2}}. \quad (4.36)$$

Figure 4.10 shows the variation of t'_B vs. k_1/k_2 for various H_1/H_2 and ϕ_1/ϕ_2 . Unlike in figure 4.9 where $t'_A = 1$ when $k_1/k_2 = 1$ and $\phi_1/\phi_2 = 1$, here we find that $t'_B > 1$ when $k_1/k_2 = 1$ for all values of H_1/H_2 and ϕ_1/ϕ_2 . This anomalous prediction arises because of the sharp interface assumption used in the derivation of t_B , and therefore t'_B . The sharp interface assumption obviously ignores mixing so that a longer time is needed to render the lower layer contaminated. Furthermore, (4.7) suggests that Q_1 decreases with k_1 , ϕ_1 , H_1 , therefore in both panels of figure 4.10 the peaks of t'_B coincide with the smallest possible values of k_1/k_2 and ϕ_1/ϕ_2 or H_1/H_2 .

4.5 Comparison between theory and experiment

Figure 4.11 shows the mean elevation, \bar{h} , of the first front vs. time for various $k_1/k_2 < 1$. The figure considers the case of equal upper and lower layer depths; similar results (not shown) apply when $H_1/H_2 \neq 1$. For each of the three k_1/k_2 values, the solid curves of figure 4.11 are extracted from the surface of figure 4.8. Model predictions are verified using experimental data corresponding to different source conditions. For a meaningful comparison, the measured mean height and corresponding advection time are non-dimensionalized using the control volume height, H , and corresponding time-scale, t_H . Moreover, the gravity current

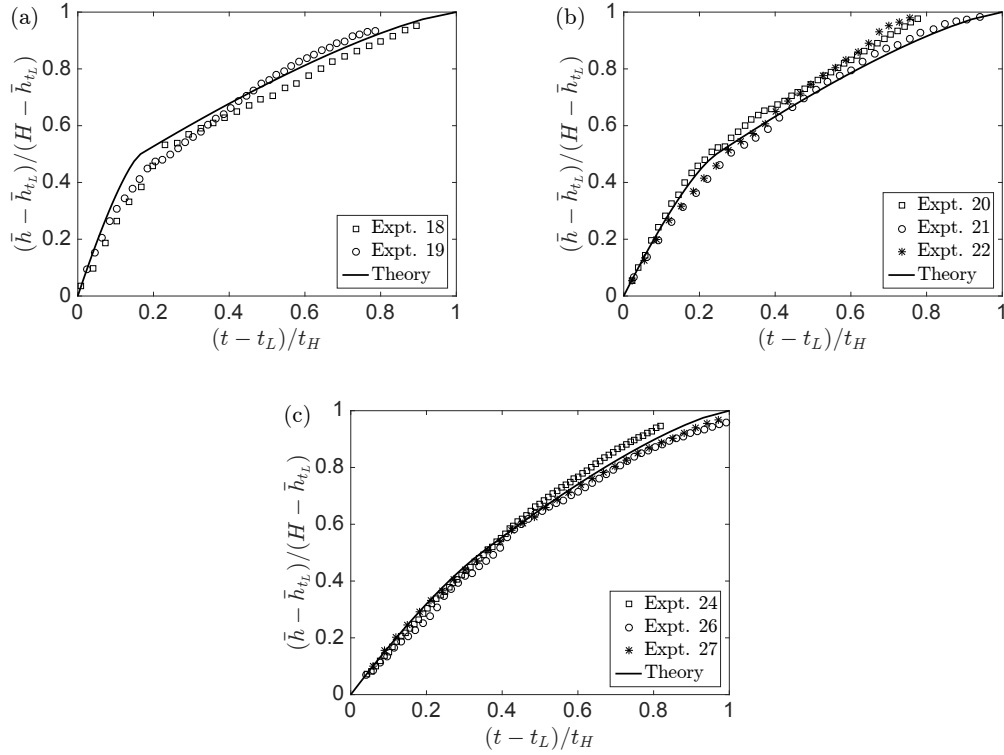


Figure 4.11: First front mean elevation when (a) $k_1/k_2 = 0.04$, (b) $k_1/k_2 = 0.11$ and (c) $k_1/k_2 = 0.36$. Experimental parameters are specified in table E.2, Appendix E. Note that $H_1/H_2 = \phi_1/\phi_2 = 1.0$ in all cases.

height, \bar{h}_{t_L} , and time scale, t_L , are respectively subtracted so that data from different experiments, organized by permeability ratio, can collapse well with the theoretical prediction. Figure 4.11 shows that a good agreement is observed in all cases. More specifically, the experimental data capture the sudden change of slope experienced when the first front reaches the interface; this effect is obviously more pronounced for smaller values of k_1/k_2 . Indirectly the favourable comparisons of figure 4.11 verify the predictions for the plume volume flux given by (4.5) and (4.9) because the first front elevation is determined from Q using a volume flux balance. Comparing panels (a) and (c), in particular the horizontal coordinate of the kink, also confirms that as k_1/k_2 decreases, the fraction of time required to fill the upper layer increases significantly for fixed height ratio.

When $k_1/k_2 > 1$, a well-defined first front does not exist in the lower layer (see figure 4.3). However, because a pair of gravity currents is generated at the

Table 4.1: Comparison of the predicted (\check{L}_g) vs. measured ($\check{L}_{g,1}$ and $\check{L}_{g,2}$) run-out lengths of the primary gravity current for various H_1/H_2 , Q_0 and g'_0 . In all experiments, $k_1/k_2 = 9.0$. Note that \check{L}_g is defined in (4.1). Moreover, $\check{L}_{g,1}$ and $\check{L}_{g,2}$ are measured using HTS images, as shown in figure 4.7 and summarized in section 4.3.2. Further experimental parameters are specified in tables E.1 and E.2, Appendix E.

Expt no.	H_1/H_2	Q_0 (cm ³ /s)	g'_0 (cm/s ²)	\check{L}_g/L	$\check{L}_{g,1}/L$	$\check{L}_{g,2}/L$
9	0.5	0.30	29.43	0.134	0.248	0.186
10	0.5	0.80	29.43	0.140	0.471	0.335
11	0.5	0.30	78.48	0.133	0.233	0.231
12	0.5	0.80	78.48	0.134	0.366	0.295
32	1.0	0.25	21.20	0.173	0.422	0.241
33	1.0	0.75	21.20	0.186	0.646	0.402
34	1.0	0.25	82.40	0.172	0.281	0.228
35	1.0	0.75	82.40	0.172	0.385	0.241

interface, we compare measured run-out lengths with the analogue predictions due to (4.1) in table 4.1. This table is limited to eight entries for the following reason: when $k_1/k_2 = 2.8$, $\check{L}_g/L \ll 1$ and when $k_1/k_2 = 25.0$ (or when $k_1/k_2 = 9.0$ but $H_1/H_2 = 2.0$), $\check{L}_g/L > 1$ – see figure 4.3 d,f. In the former (latter) case, measurements of \check{L}_g are problematic (impossible), and hence any comparison with the predictions of section 4.4 is not worthwhile. On the other hand, when $k_1/k_2 = 9.0$ and $H_1/H_2 = 0.5$ or 1.0 , $\mathcal{O}(0.1) < \check{L}_g/L < 1$, and therefore it is possible to make a comparison with theory. In drawing such a comparison, note that table 4.1 reports two different experimental values, one measured immediately above ($\check{L}_{g,1}$) the interface and one measured below ($\check{L}_{g,2}$), i.e. midway between the interface and the lower boundary. Drawing such a distinction is necessary because, as figures 4.7 d,e indicate, but in contrast to figure 2 of Goda & Sato (2011), measurements of the primary gravity current length are different between the two layers with $\check{L}_{g,1} > \check{L}_{g,2}$. Moreover, recall from (4.29) that \check{L}_g is predicted by balancing the plume volume flux, q_1 , and the flux of dense fluid draining into the lower layer from the gravity current underside. Figure 4.7 a suggests that the volume flux of the draining fluid is associated only with $\check{L}_{g,2}$, not $\check{L}_{g,1}$. On this basis, it is more appropriate to compare \check{L}_g vs. $\check{L}_{g,2}$.

In table 4.1, we find that measured values for \check{L}_g are larger than their predicted

counterparts by 39% on average. The likely reason for this discrepancy is as follows: the prediction for \check{L}_g given by (4.1), is predicated on a sharp interface assumption. On the other hand, if interfaces are not sharp such that mixing occurs, this mixing results in a decrease of g'_{2B} , the reduced gravity measured below the interface. In that case, (4.25) ought to instead yield $\check{L}_g = q_1\nu/k_2g'_{2B}$. For reasons discussed previously in section 4.3.2 it is difficult to precisely estimate g'_{2B} from our current experimental images, however, figures 4.3f, 4.4, 4.5 and 4.6 b clearly support the notion that mixing leads to a depressed value for g'_{2B} (i.e. notably below g'_1), which, in turn, leads to an under-prediction of \check{L}_g on the part of (4.1).

In order to compare the variation of the filling box time, t_T , with k_1/k_2 , results are plotted in figure 4.12 for all 50 experiments where panels (a), (b) and (c) correspond, respectively, to $H_1/H_2 = 0.5, 1.0$ and 2.0 . The comparison is made in two steps: first, the dimensionless timescales, t'_A and t'_B , defined by (4.23) and (4.36), respectively, are compared with each other, then the comparisons are drawn against laboratory data.

Although t'_A was derived by assuming $k_1/k_2 \leq 1.0$, we extend the (thick) curve in question into the regime where $k_1/k_2 > 1.0$ to examine its applicability for larger values of the permeability ratio. The extension of t'_A to $k_1/k_2 > 1.0$ implies, in effect, that whatever entrainment may be associated with contaminated fluid draining from the underside of the primary gravity current is comparable to that associated with a single descending plume. On the other hand, t'_B from (4.36) is predicted using a sharp interface assumption such that any mixing between the contaminated and ambient fluid is assumed negligible. Thus the thick dashed and thin solid curves denoting t'_A and t'_B , respectively, converge for sufficiently large k_1/k_2 . In this limit, k_2 is comparatively small suggesting only a limited opportunity for entrainment of lower layer ambient fluid on the part of descending contaminated fluid. The models leading to (4.23) and (4.36) therefore become effectively the same: in neither case is appreciable mixing below the interface permitted. Furthermore, we observe a reduced difference between t'_A and t'_B for smaller H_1/H_2 . When the lower layer is relatively thin, the contaminated fluid

has less opportunity to mix with large volumes of ambient fluid before reaching the lower impermeable boundary. Therefore, and as in the case of large k_1/k_2 , the plume volume flux deviates little from Q_1 for $H_1 < x < H$.

On comparing theory and experiment in figure 4.12, we generally find good agreement between measured data points and the thick solid curve. By contrast, when $k_1/k_2 > 1.0$, favourable agreement is typically observed only for sufficiently large H_1/H_2 and k_1/k_2 whereby entrainment in the lower layer is expected to be modest. The divergence of data observed in panel (b) when $k_1/k_2 = 25.0$ is primarily because $\check{L}_g/L > 1$ in these experiments. The lower layer therefore becomes isolated as in figure 4.3 f, whereby the upper layer fills faster than the lower layer and it becomes difficult to ascertain when the entire control volume has become filled with contaminated fluid. There are, in other words, additional physical effects at play that are not thoroughly accounted by (4.23) and (4.36). Further examination of these effects is outside the scope of the present study.

4.6 Conclusions

Extending the works of Roes *et al.* (2014) and Sahu & Flynn (2015, 2016b), filling box flows in porous media are studied experimentally and analytically to examine the effects of sudden permeability changes in a rectilinear control volume. The flow is assumed to be Boussinesq and laminar such that the $Pe \gg \mathcal{O}(1)$ where Pe is the Péclet number. The buoyant convection is driven by a line source that spans the width of the control volume and whose effluent is miscible within the ambient fluid that saturates the porous medium.

Experiments were performed considering as independent variables the permeability (k_1/k_2) and height (H_1/H_2) ratios of the upper and lower layers as well as the source volume flux (Q_0) and reduced gravity (g'_0). As summarized in Appendix E, a total of six permeability ratios, namely 0.04, 0.11, 0.36, 2.78, 9.0 and 25.0, were considered in combination with three height ratios, namely 0.5, 1.0 and 2.0. Meanwhile source conditions were varied over the following intervals: $0.25 \leq Q_0 \leq 0.80$ (cm³/s) and $20.0 \leq g'_0 \leq 80.0$ (cm/s²).

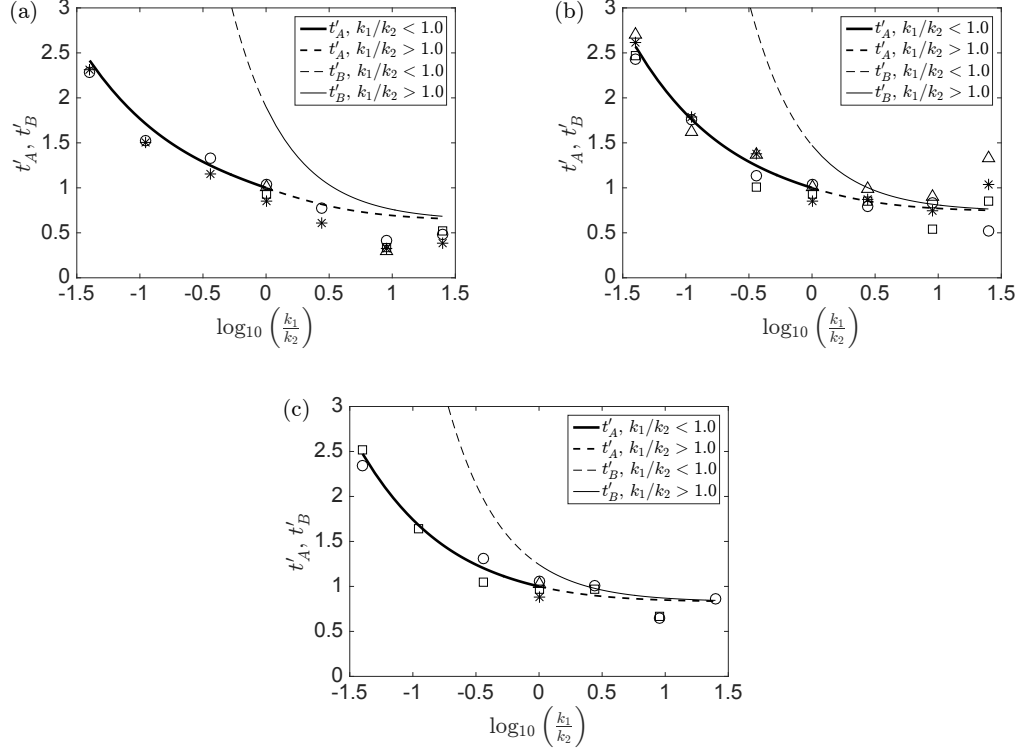


Figure 4.12: Non-dimensional filling box time when (a) $H_1/H_2 = 0.5$, (b) $H_1/H_2 = 1.0$ and (c) $H_1/H_2 = 2.0$. Note that $\phi_1/\phi_2 = 1.0$ in all cases. Discrete data shows the measured values; the data presented for $k_1/k_2 = 1.0$ correspond to Experiments 1, 3, 7 and 8 of Sahu & Flynn (2015, table 1). Experimental data are corrected for finite source effects by adding the time required for the first front to advect from $x = 0$ to $x = -x_0$. Symbols represent the following range of values for Q_0 and g'_0 : (i) circles: $0.20 \leq Q_0 \leq 0.50$ (cm^3/s), $25.0 \leq g'_0 \leq 50.0$ (cm/s^2), (ii) stars: $0.60 \leq Q_0 \leq 0.80$ (cm^3/s), $25.0 \leq g'_0 \leq 50.0$ (cm/s^2), (iii) squares: $0.20 \leq Q_0 \leq 0.50$ (cm^3/s), $60.0 \leq g'_0 \leq 80.0$ (cm/s^2) and (iv) triangles: $0.60 \leq Q_0 \leq 0.80$ (cm^3/s), $60.0 \leq g'_0 \leq 80.0$ (cm/s^2).

When $k_1/k_2 < 1.0$, the observed flow dynamics are qualitatively similar to the case of a uniform porous medium, i.e. when $k_1/k_2 = 1$. Thus, consistent with Sahu & Flynn (2015), the filling box flows are dominated by (i) a negatively-buoyant plume, (ii) oppositely-directed gravity currents that propagate along the lower impermeable boundary and (iii) a first front that propagates in the vertical direction towards the source. Accordingly the analytical formulations of Sahu & Flynn (2015) are adopted when predicting key dynamical parameters e.g. the time-scales associated with the motion of the gravity currents and first front. In the present case, however, different permeabilities and virtual source corrections must be applied for the upper and lower layers.

On the other hand, the experiments with $k_1/k_2 > 1.0$ exhibit significantly different flow dynamics from those relevant to the uniform porous medium case. The dense plume after reaching the interface divides into two parts. Some of the plume fluid propagates horizontally outward as a pair of oppositely-directed (primary) gravity currents. The remaining volume of the plume fluid directly drains into the lower layer and subsequently creates a pair of (secondary) gravity currents that propagate along the lower impermeable boundary. The flow of the primary and secondary gravity currents are distinct one from the other. Because of continuous drainage from the underside of the primary gravity current, the motion of the front is irregular, i.e. the front temporarily stops after traveling a horizontal distance \check{L}_g , which decreases with g'_0 but increases with k_1/k_2 and Q_0 . Therefore, in several cases, for instance the experiments with $k_1/k_2 = 25.0$, $\check{L}_g > L$, where L is the horizontal distance of the sidewall from the source. In such instances, the ambient fluid in the lower layer becomes isolated from that in the upper layer. Consequently, only a relatively small volume of discharged plume fluid may infiltrate the lower layer by the time of overflow, defined as the time at which discharged plume fluid reaches the elevation of the source in the upper layer. A formula for \check{L}_g , taken from Goda & Sato (2011), is presented in (4.1). The equation was originally derived by assuming immiscible fluids, and therefore a sharp interface between the draining fluid and the lower layer ambient fluid. However the image analysis of section 4.3 shows that significant mixing may arise

in case of miscible fluids and media with comparatively large ϕ (here $\phi \simeq 0.38$ away from the interface). Although it is outside of the scope of the present inquiry to analytically estimate the degree of mixing, the analysis associated with figure 4.6 suggests that the reduced gravity the draining fluid can be notably smaller than that of the primary gravity current. Therefore, when considering miscible fluids, the prediction of Goda & Sato (2011) must be regarded as a lower bound that is easily exceeded by measured values (table 4.1).

For $k_1/k_2 < 1.0$, the time, t'_A , required for overflow is given by (4.23). The corresponding time, t'_B , for the $k_1/k_2 > 1.0$ case is given by (4.36). Consistent with the above remarks, the latter formula ignores any detailed analytical accounting for mixing and instead assumes a sharp interface model in the lower layer. Correspondingly, we find from figure 4.12 that predicted values for t'_B generally over-predict analogue measurements, though the agreement typically improves with decreasing lower layer depth: as H_2 decreases, there is less opportunity for mixing between the discharged plume fluid and the surrounding ambient. On the other hand, relatively poor agreement is noted when $\check{L}_g/L > 1.0$. As remarked previously, the primary gravity current in this case isolates the lower from the upper layer whereby overflow may occur before the lower layer is fully or even moderately contaminated with discharged plume fluid. Furthermore, on comparing the measured values with t'_A for $k_1/k_2 > 1.0$, provided $\check{L}_g/L < 1.0$, in figure 4.12, a reasonably good agreement is obtained; the entrainment into the descending dense fluid is interestingly therefore similar to or slightly larger than that associated with a single discrete plume.

The derivations of section 4.4.2, when $k_1/k_2 > 1.0$, consider several simplifying assumptions, e.g. that of the sharp interface, which are necessary to make analytical progress in the current work. Determining more precisely the rate of entrainment of ambient fluid into the dense fluid that drains from the underside of the primary gravity current is an important topic of future study. Moreover, the current work assumes a horizontal interface between two permeable media. However, in real geophysical scenarios, thrust may render such interfaces non-horizontal and also non-planar. In the near future, we therefore plan to study

the effects of inclined porous layers in the context of filling box flows.

Chapter 5

Summary and conclusions

While “filling box” flows have been extensively studied in context of free turbulent plumes since the investigation of Baines & Turner (1969), negligible efforts have been made for studying them in context of a porous medium. Roes *et al.* (2014) studied filling box type flow in a leaky porous medium but focused only on the long-time behavior. Thus Roes *et al.* (2014)’s investigation considers steady conditions wherein the plume volume flux at the first front elevation balances the outflux of discharged plume fluid through the fissures located at the bottom of the box. Expanding significantly on this previous work, we herein study the transient behavior of filling box flows in confined porous media. Two specific cases are considered: a uniform and a non-uniform porous media. In the former case, filling box flows are studied both in a rectilinear and in an axisymmetric geometry, whereas in the latter case, filling box flows are studied only in a rectilinear geometry.

The flow components in the uniform case are divided into three primary regimes, namely the plume, gravity current and first front. The source of dense fluid is located at the top of the control volume and creates a negatively-buoyant plume in an ambient of light fluid. Moreover, the flow is assumed to be in a Boussinesq, Darcy regime with Péclet number $Pe \gg \mathcal{O}(1)$. For Darcy plumes with $Pe \lesssim \mathcal{O}(1)$, a solution describing the plume behavior already exists in the literature (Wooding, 1963). However, the situation is different for $Pe \gg \mathcal{O}(1)$ and the self-similar solutions presented in Chapters 2 and 3 are the first of their kind to the best of our knowledge.

In Chapter 2 we study filling box flows that originate from a line source in a rectilinear box, which is filled with a uniform porous medium. By considering the governing equations for mass and momentum continuity, solute transport and an equation of state, a self-similar solution is derived for the plume streamfunction and solute concentration. This self-similar solution is further used to determine the parameters of particular interest, i.e. the plume volume flux, momentum flux and reduced gravity, as functions of the source and porous medium parameters and the distance from the source. We found that the plume volume flux varies as $Q \propto x^{1/4}$, whereas in Wooding's analysis $Q \propto x^{1/3}$. After reaching the horizontal impermeable boundary, the dense plume spreads laterally outwards in the form of gravity currents. Although gravity current solutions have been derived previously by several researchers like Huppert & Woods (1995) and Lyle *et al.* (2005), the gravity current problem has not yet been studied in the context of a filling box flow in which case the inflow to the gravity current is specified by the outflow from the plume. We adapt the previously derived similarity solution for 2-D gravity currents (Huppert & Woods, 1995) and couple that with our plume solution. For prescribed plume volume flux and reduced gravity at $x = H$, where H is the control volume height, resulting solution consequently gives the length and height profile of the gravity current as functions of time, porous medium porosity and permeability. Once the gravity current reaches the impermeable sidewall, the discharged dense fluid begins advecting upwards. Initially, the first front, i.e. the interface between the dense and ambient fluids, has a curved interface, however, this curvature later disappears and the first front becomes nearly horizontal. We solve for the spatio-temporal evolution of the first front numerically using a finite difference scheme in space and time. By considering the mean first front height, \bar{h} , an analytical solution is also derived by applying a volume flux balance between the plume and the first front. The resultant formula suggests that the first front advects upwards in time, t , as $(H - \bar{h}) \propto t^{4/3}$. Furthermore, the mean first front elevation is found to have the same value whether calculated numerically or analytically.

Similitude laboratory experiments were performed in a rectangular box that

was filled with uniform beads and tap water. While the tap water served as a light ambient fluid, salt water was used as a dense source fluid and was supplied at the top of the box using a line nozzle designed by Roes (2014). During each experiment, images of the flow field were recorded, and later post-processed in Matlab. The post-processing of the recorded images gave the measured values for the parameters of interest, namely the gravity current length and height and the first front elevation. These measurements were then compared with their analytical counterparts. This method of comparing theory and experiment is deemed preferable to one involving a direct assessment of plume properties such as the plume volume flux because of the significant experimental difficulty associated with measuring such fluxes e.g. using particle image velocimetry. It should be noted, however, that parameters such as the first front height are directly related to the plume volume flux (see e.g. equation 2.43), and so the favorable agreement seen in figures like figure 2.10 is strong confirmation that the plume model of Chapter 2 is robust.

Chapter 3 of the thesis includes a theoretical model of filling box flows in an axisymmetric geometry having a point source. Similar to Chapter 2, here also the filling box flow is divided into the plume, gravity current and first front flow regimes. The plume is considered to be in a Boussinesq, Darcy regime with $Pe \gg \mathcal{O}(1)$ where, again, no known self-similar solution is previously available. We therefore derive a novel similarity solution for the plume streamfunction and solute concentration by considering the governing equations for mass and momentum continuity, solute transport and an equation of state. This solution is then used to evaluate the volume flux, reduced gravity and momentum flux. Contrary to the case where $Pe \lesssim \mathcal{O}(1)$, we find that with $Pe \gtrsim \mathcal{O}(1)$, the plume volume flux also depends on the permeability, viscosity and the source buoyancy flux in addition to the porosity and the distance from the source.

Regarding the horizontal outflow of the discharged plume fluid at the bottom boundary, Lyle *et al.* (2005)'s similarity solution for an axisymmetric gravity current is used. The plume volume flux and reduced gravity at $x = H$ serve as inputs for the gravity current problem. Thus the plume and gravity current

solutions are coupled together and this coupling must be exploited to determine the propagation of the gravity current. As the gravity current leading edge reaches the lateral wall of the cylindrical control volume, the contaminated fluid starts advecting upward towards the source in the form of a deepening layer whose upper boundary is the first front. Although the first front in this case ought to have a curved interface, we solve only for its mean elevation by again employing a volume flux balance. On recalling from the solution of rectilinear geometry of Chapter 2 that the mean first front elevation has effectively the same value calculated whether numerically or analytically, it can be assumed that such an approach where the curvature of the first front is ignored still gives a robust estimate of the mean elevation.

Apart from deriving solutions for various flow regimes, an analysis is also presented concerning the maximum amount of source fluid or solute that may be sequestered without overflow in a porous medium of given properties. We found that more source fluid can be injected by setting a larger flow rate but smaller reduced gravity. However, for injecting more solute mass both the source volume flux and reduced gravity should be made large.

Because in real geophysical scenarios the reservoir permeability and porosity may not necessarily be uniform, in Chapter 4 a non-uniform medium is considered. Thereby filling box flows are studied in a two layer porous medium characterizing the effects of sudden changes in permeability and porosity. Two configurations are considered: first, a lower permeable medium over a higher permeable medium, and vice-versa. The flow behavior obtained in the former configuration is qualitatively similar to that of the uniform porous medium case. For quantifying the flow parameters, therefore, the analytical solutions from Chapter 2 are employed. We derive formulas for the gravity current length and height, the first front elevation and the filling box time i.e. the time required by the source fluid to fill the control volume up to the point of overflow.

In the latter configuration when the higher permeability layer is on top, the flow pattern observed is qualitatively quite different from the uniform case. The dense plume, after reaching the interface, splits into two parts. While some frac-

tion of the plume fluid moves horizontally outwards in the form of a (leaky) gravity current, the remaining portion flows downwards into the lower layer. Note that, due to draining along its underside, the interfacial gravity current can propagate only up to a certain maximum horizontal distance from the source. We refer to this distance as the runout length, \check{L}_g . \check{L}_g depends upon the source parameters and the permeability ratio k_1/k_2 , i.e. the ratio of the upper vs. lower layer permeabilities. If k_1/k_2 is sufficiently large or the control volume length, L , is sufficiently small, \check{L}_g may be greater than L . In that case, the lower layer becomes isolated and the majority of the fluid discharged by the plume remains in the upper layer. For an effective filling of a layered porous reservoir, it is therefore advantageous to have $\check{L}_g < L$. We use Goda & Sato (2011)'s asymptotic solution to analytically determine \check{L}_g . Goda & Sato (2011) derived their solution considering immiscible fluids, thus assuming a sharp interface between the draining dense fluid and the lower layer ambient fluid. However, in the current investigation miscible fluids are used for experiments, and therefore Goda & Sato (2011)'s solution shows some discrepancies with our measurements. As a remedy, instead of applying in (4.26) the reduced gravity of the gravity current as in Goda & Sato (2011), the reduced gravity of the draining fluid should instead be considered. Because of entrainment of the ambient fluid into the fluid that drains from the gravity current, the reduced gravity of the latter is smaller than that of the gravity current. By substituting one reduced gravity for the other, the predicted runout length, which varies inversely with the reduced gravity, should in fact be larger than the prediction of Goda & Sato (2011).

An analytical formulation is also developed for predicting the filling box time. It is calculated using two different methods that employ the following separate assumptions: (i) an entrainment of lower ambient fluid into draining dense fluid equal to that due to laminar plume flow and (ii) the existence of a sharp such that there is no mixing between the draining and ambient fluids. We found a significant difference in the associated predictions when $k_1/k_2 \simeq 1.0$. This difference disappears when $k_1/k_2 \gg 1.0$ in which case the total amount of entrained fluid in the lower layer is negligible compared to the plume volume flux at the

interface. Effectively the assumptions considering or neglecting the entrainment become the same. Measurements from the experiments with smaller k_1/k_2 show a good agreement with the former (entrainment-permitting) model. This agreement implies that the amount of entrainment of ambient fluid into the dense fluid that falls from a point vs. distributed source is quantitatively similar, this in spite of the numerous important physical differences between localized and distributed convection. On the other hand, for larger k_1/k_2 the agreement rather depends upon \check{L}_g/L . While good agreement is found when $\check{L}_g/L < 1.0$, in cases when $\check{L}_g/L > 1.0$ our models fail to estimate the filling box time because, as discussed above, the lower layer becomes isolated from the dense fluid. For finding the filling box time when $\check{L}_g/L > 1.0$, a Rayleigh-Taylor-Instability problem has to be solved which is outside the scope of the current thesis and is therefore considered as future work.

5.1 Primary contributions from the present work

The main findings and contributions of this thesis work can be summarized in the following major points:

- Filling box flows are studied in the context of confined porous media which, to our knowledge, has not been studied previously. Analytical solutions are presented for the associated flows, i.e. the plume, gravity current and first front. The analytical models are validated using similitude laboratory experiments for rectilinear geometry. However, in case of axisymmetric geometry, only a theoretical model is presented whose result should be validated experimentally in future.
- Related to the previous bullet, novel similarity solutions are derived for laminar plumes with line and point sources having Péclet number $Pe \gg \mathcal{O}(1)$. Particularly in case of a point source, and unlike in the case when $Pe \lesssim \mathcal{O}(1)$ (Wooding, 1963), our new formula suggests that the plume volume flux also depends on the source buoyancy flux, permeability and viscosity in addition to the porosity and the distance from the source.

- Filling box flows in a non-uniform porous medium having a sudden change in porosity and permeability are investigated. Experiments are conducted for a total of seven permeability ratios ranging from 0.04 to 25.0. We find that for an effective filling of a layered porous medium, the runout length of the (interfacial) gravity current should be smaller than the length of the porous medium.
- An analysis is presented for maximizing the volume of source fluid or mass of solute sequestered in a reservoir of given parameters by controlling the source volume flux and reduced gravity. We found that a larger fluid volume can be injected by increasing the source volume flux and/or decreasing the source reduced gravity. On the other hand, if it is desired to inject the maximum solute mass, both the source volume flux and reduced gravity should be made large.
- Filling box times, i.e. the times required by the dense fluid to reach overflow, are estimated and verified using laboratory experiments. We find that our theoretical predictions show satisfactory agreement with the measured values for uniform porous medium experiments. In case of a non-uniform porous medium, good agreement is found only when the runout length is smaller than that of the porous medium. The theoretical prediction of our investigation assumes that both layers are entirely contaminated with dense fluid which, however, is not the case when the former is greater than the latter. As a result, our model predictions are not in good agreement with experimental measurements in this case.

5.2 Future work

After solving several critical problems related to filling box flows in porous media, there are still underlying problems that ought to be pursued in future investigations. Primary topics for future studies are identified as follows:

- So as to make analytical progress, the current filling box model is studied

by making some unavoidable assumptions, i.e. Darcy flow and miscibility. While the first assumption can be controlled by setting the source volume flux, the second condition depends on the nature of the problem and the chemical composition of the fluids involved. For example, in carbon sequestration the supercritical CO₂ and brine are primarily immiscible with each other (Riaz *et al.*, 2006). Keeping such practical situations on mind, the above mentioned assumptions should be relaxed and filling box flows can then be investigated in a non-Darcy regime and/or with immiscible fluids. Considering again the same example, Huppert & Neufeld (2014) discuss how for long-time feasibility of carbon sequestration, the residual trapping of supercritical CO₂ in brine-filled aquifers plays as important a role as convective dissolution. Thus, while studying filling box flows in the immiscible fluid context, interfacial phenomena like residual trapping should be taken into account.

- The analytical solution derived by Goda & Sato (2011) for the gravity current runout length in layered porous media strictly applies only for immiscible fluids. On the other hand, the miscible fluid experiments of Chapter 4 show that there is significant entrainment of lower layer fluid into the fluid that drains from the base of the interfacial gravity current. Not surprisingly then and because Goda & Sato (2011) assumed a sharp interface between the former and latter fluids, their prediction does not agree well with our measurements. In a future investigation, one could quantify the amount of entrainment experimentally or theoretically, and thereby modify the present formula for the runout length by employing an empirical or semi-empirical factor whose value depends upon the amount of entrainment.
- In real geophysical scenarios, permeability and porosity may be highly non-uniform not only in the vertical direction, but also in the horizontal plane. In other words, the layered porous strata may not necessarily be horizontal and the interface between adjacent layers may be inclined at some angle (Gunn & Woods, 2011; Loubens & Ramakrishnan, 2011). Filling box flows

can therefore be studied in the context of inclined layered porous media to determine the effect of such an inclination on parameters like the gravity current runout length, filling box times etc. The observations from such a study are expected to differ from the present (symmetric) investigation in numerous important ways: the dense plume after reaching the interface should divide unequally into two gravity currents that flow left and right at different speeds and with different heights and runout lengths. The larger the inclination angle, the larger should be the fraction of discharged plume fluid flowing downslope. Moreover, this fraction may also depend upon the permeability ratio, the plume volume flux and reduced gravity. As a result of the above asymmetry, the amount of dense fluid draining into the lower layer should be different on either side of the plume and this is expected to nontrivially influence the calculation of the filling box time. In future study, it is therefore important to study filling box flows in a porous medium with inclined porous layers to investigate the above effects in detail and to quantify the precise influence of the inclination angle on key parameters of interest.

- Apart from the analytical studies of filling box flows, numerical modelling can also be done. The findings from the current research can be used to validate the base models in numerical simulation, which can then be further extended to add higher complications, e.g. immiscible fluids.

Appendices

Appendix A

Rectilinear plumes in Darcy regime with $\text{Pe} \lesssim \mathcal{O}(1)$

A dense plume generating from a line source of width Λ is considered. The flow is assumed to be in Darcy regime with Péclet number $\text{Pe} \lesssim \mathcal{O}(1)$. Moreover, the Boussinesq approximation is assumed to be valid. The associated governing equations therefore read

$$\frac{\partial u}{\partial x} + \frac{\partial v}{\partial y} = 0, \quad (\text{A.1})$$

$$\frac{1}{\rho_0} \frac{\partial P}{\partial x} + \frac{\nu}{k} u = \frac{g\rho}{\rho_0}, \quad (\text{A.2})$$

$$\frac{1}{\rho_0} \frac{\partial P}{\partial y} + \frac{\nu}{k} v = 0, \quad (\text{A.3})$$

$$\frac{1}{\phi} \left(u \frac{\partial C}{\partial x} + v \frac{\partial C}{\partial y} \right) = D_d \left(\frac{\partial^2 C}{\partial x^2} + \frac{\partial^2 C}{\partial y^2} \right), \quad (\text{A.4})$$

$$\rho = \rho_0(1 + \beta C). \quad (\text{A.5})$$

In the above equations, P is the fluid pressure, u and v are the transport velocities in vertical and horizontal axes, respectively, ν is the kinematic viscosity, C is the solute concentration and D_d is the molecular diffusion coefficient. Moreover, ρ is the fluid density whose value at far-field is ρ_0 and β is the solute contraction coefficient.

By combining the momentum equations, (A.2) and (A.3), the fluid pressure can be eliminated such that

$$\frac{\nu}{k} \left(\frac{\partial u}{\partial y} - \frac{\partial v}{\partial x} \right) = \frac{g}{\rho_0} \frac{\partial \rho}{\partial y}. \quad (\text{A.6})$$

Then a boundary layer approximation is applied which assumes

$$\left| \frac{\partial v}{\partial x} \right| \ll \left| \frac{\partial u}{\partial y} \right| \quad \text{and} \quad \left| \frac{\partial^2 C}{\partial x^2} \right| \ll \left| \frac{\partial^2 C}{\partial y^2} \right|. \quad (\text{A.7})$$

Now a streamfunction, ψ , can be introduced such that

$$u = \frac{\partial \psi}{\partial y} \quad \text{and} \quad v = -\frac{\partial \psi}{\partial x}. \quad (\text{A.8})$$

Substitution of ψ straightforwardly satisfy (A.1), whereas, (A.6) and (A.4) become, respectively,

$$\frac{\partial^2 \psi}{\partial y^2} = \frac{g\beta k}{\nu} \frac{\partial C}{\partial y} \quad (\text{A.9})$$

and

$$\frac{\partial \psi}{\partial y} \frac{\partial C}{\partial x} - \frac{\partial \psi}{\partial x} \frac{\partial C}{\partial y} = D_d \phi \frac{\partial^2 C}{\partial y^2}. \quad (\text{A.10})$$

The above equations suggest a selfsimilar solution of the form

$$\psi = Ax^{1/3} \mathcal{F}(\eta), \quad C = \frac{B}{x^{1/3}} \mathcal{F}'(\eta), \quad (\text{A.11})$$

where A and B are constants to be determined shortly and η is the selfsimilar variable that is defined as $\eta = \frac{y}{x^{2/3}} \left[\frac{F_0 k}{(D_d \phi)^2 \Lambda \nu} \right]^{1/3}$. By substituting (A.11) into (A.9), and with some simplification, one can get

$$B = \frac{A\nu}{g\beta k} \left[\frac{F_0 k}{(D_d \phi)^2 \Lambda \nu} \right]^{1/3}. \quad (\text{A.12})$$

On the other hand, substitution of (A.11) into (A.10) yields

$$\frac{D_d \phi F_0 k}{\Lambda \nu} \mathcal{F}''' + \frac{1}{3} A (\mathcal{F} \mathcal{F}')' = 0. \quad (\text{A.13})$$

For purpose of getting a dimensionless form of (A.13), the constant A should be defined as

$$A = \left(\frac{D_d \phi F_0 k}{\Lambda \nu} \right)^{1/3}, \quad \text{and therefore} \quad B = \frac{1}{g\beta} \left(\frac{F_0^2 \nu}{\Lambda^2 D_d \phi k} \right)^{1/3}. \quad (\text{A.14})$$

Now on integrating (A.13), and recalling that $S = 0$ at far-field, yields

$$\mathcal{F}' = \frac{1}{6} (c^2 - \mathcal{F}^2), \quad (\text{A.15})$$

which has a solution of the form

$$\mathcal{F} = c \tanh \left(\frac{1}{6} c \eta \right). \quad (\text{A.16})$$

Here c is a constant of integration and determined by recalling that the buoyancy flux, F_0 , is independent of the vertical coordinate, x , in an unstratified ambient. Mathematically,

$$F_0 = \Lambda \int_{-\infty}^{\infty} u g' dy. \quad (\text{A.17})$$

Here g' is the reduced gravity and defined as

$$g' = g \left(\frac{\rho - \rho_0}{\rho_0} \right) = g\beta C. \quad (\text{A.18})$$

The last term in (A.18) follows from (A.5). Substitutions of (A.8), (A.11), (A.16) and (A.18) into (A.17) and some useful cancellation yield $c = (9/2)^{1/3}$. Finally on using this derived solution the plume volume flux, Q , can be determined as

$$Q = \Lambda \int_{-\infty}^{\infty} u dy = \left(\frac{36D_d F_0 k \Lambda^2 x}{\nu} \right)^{1/3}. \quad (\text{A.19})$$

Moreover, the plume momentum flux, M , can be given as

$$M = \Lambda \int_{-\infty}^{\infty} u^2 dy = \frac{F_0 k}{\nu}. \quad (\text{A.20})$$

Appendix B

Axisymmetric plumes in Darcy regime with $\text{Pe} \lesssim \mathcal{O}(1)$

Making similar assumptions as in Appendix A, the governing equations for a circular plume generating from a point source can be given as

$$\frac{\partial u}{\partial x} + \frac{\partial u_r}{\partial r} = 0, \quad (\text{B.1})$$

$$\frac{1}{\rho_0} \frac{\partial P}{\partial x} + \frac{\nu}{k} u = \frac{g\rho}{\rho_0}, \quad (\text{B.2})$$

$$\frac{1}{\rho_0} \frac{\partial P}{\partial r} + \frac{\nu}{k} u_r = 0, \quad (\text{B.3})$$

$$\frac{1}{\phi} \left(u \frac{\partial C}{\partial x} + u_r \frac{\partial C}{\partial r} \right) = D_d \left[\frac{\partial^2 C}{\partial x^2} + \frac{1}{r} \frac{\partial}{\partial r} \left(r \frac{\partial C}{\partial r} \right) \right], \quad (\text{B.4})$$

$$\rho = \rho_\infty (1 + \beta C). \quad (\text{B.5})$$

A boundary layer approximation similar to (A.7) is assumed and a streamfunction, ψ_s , is introduced such that

$$u = -\frac{1}{r} \frac{\partial \psi_s}{\partial r} \quad \text{and} \quad u_r = \frac{1}{r} \frac{\partial \psi_s}{\partial x}, \quad (\text{B.6})$$

The momentum equations, (B.2) and (B.3), and solute transport, (B.4), can be then modified to, respectively,

$$\frac{\partial}{\partial r} \left(\frac{1}{r} \frac{\partial \psi_s}{\partial r} \right) = \frac{g\beta k}{\nu} \frac{\partial C}{\partial r} \quad (\text{B.7})$$

and

$$\frac{1}{r} \frac{\partial \psi_s}{\partial r} \frac{\partial C}{\partial x} - \frac{1}{r} \frac{\partial \psi_s}{\partial x} \frac{\partial C}{\partial r} = \frac{D_d \phi}{r} \frac{\partial}{\partial r} \left(r \frac{\partial C}{\partial r} \right). \quad (\text{B.8})$$

Further, a self-similar solution of the following form can be obtained for (B.7) and (B.8)

$$\psi_s = Ax\mathcal{F}(\eta), \quad C = \frac{B}{x}\mathcal{G}(\eta), \quad (\text{B.9})$$

where $\eta = \frac{r}{D_d\phi x} \sqrt{\frac{F_0 k}{2\pi\nu}}$. Substituting (B.9) into (B.7) gives

$$\mathcal{G} = \frac{1}{\eta}\mathcal{F}', \quad (\text{B.10})$$

provided B is defined as $B = \frac{F_0 A}{2\pi g\beta(D_d\phi)^2}$. On the other hand, (B.8) delivers

$$-\mathcal{F}'(\mathcal{G}\eta)' - \mathcal{G}'(\mathcal{F} - \mathcal{F}'\eta) = \frac{D_d\phi}{A}(\mathcal{G}'\eta)', \quad (\text{B.11})$$

which also suggests that $A = D_d\phi$. Following (Phillips, 1991), analytical solutions of (B.10) and (B.11) can be given as

$$\psi_s = \frac{3D_d\phi x\eta^2}{8 + \frac{3}{4}\eta^2}, \quad C = \frac{3F_0}{8\pi g\beta D_d\phi x \left(1 + \frac{3}{32}\eta^2\right)^2}. \quad (\text{B.12})$$

Similar to the discussion of Appendix A, the numerical values of above parameters, i.e. \mathcal{F} and \mathcal{G} , can be derived by recalling that the buoyancy flux is independent of vertical coordinate for an unstratified ambient. Thereby,

$$F_0 = 2\pi \int_0^\infty ug'rdr d\theta. \quad (\text{B.13})$$

The volume flux of the axisymmetric plume can be then straightforwardly given as

$$Q = 2\pi \int_0^\infty urdr = 8\pi D_d\phi x. \quad (\text{B.14})$$

Appendix C

Curved interface methodology

In this appendix, we present the details of the numerical technique employed to solve for the motion of the (curved) first front.

Space and time derivatives are discretized so that (2.41) is replaced by

$$\frac{h_i^{n+1} - h_i^n}{\Delta t} = \frac{S}{2\Delta y^2} (h_{i-1}^{n+1} h_{i-1}^n - 2h_i^{n+1} h_i^n + h_{i+1}^{n+1} h_{i+1}^n) \quad (\text{C.1})$$

where i and n represent space and time indices, respectively. By symmetry, we only concern ourselves with the right-hand side of the control volume so that $i = 1$ corresponds to the box centerline at $y = 0$ whereas $i = L/\Delta y + 1 = I + 1$ corresponds to the position of the right sidewall at $y = L$. On further simplification and rearranging, (C.1) becomes,

$$-(Rh_{i-1}^n)h_{i-1}^{n+1} + (1 + 2Rh_i^n)h_i^{n+1} - (Rh_{i+1}^n)h_{i+1}^{n+1} = h_i^n \quad (\text{C.2})$$

where $R = \frac{S\Delta t}{2\Delta y^2}$. In matrix form, (C.2) is expressed as

$$\begin{bmatrix} 1 + 2Rh_2^n & -Rh_3^n & 0 & 0 & \dots & 0 \\ -Rh_2^n & 1 + 2Rh_3^n & -Rh_4^n & 0 & \dots & 0 \\ & & \ddots & & & \\ 0 & \dots & 0 & -Rh_{I-1}^n & 1 + 2Rh_I^n & -Rh_{I+1}^n \\ 0 & \dots & 0 & 0 & -2Rh_I^n & 1 + 2Rh_{I+1}^n \end{bmatrix} \begin{bmatrix} h_2^{n+1} \\ h_3^{n+1} \\ h_4^{n+1} \\ \vdots \\ h_{I-1}^{n+1} \\ h_I^{n+1} \\ h_{I+1}^{n+1} \end{bmatrix} = \begin{bmatrix} h_2^n + Rh_1^n h_1^{n+1} \\ h_3^n \\ h_4^n \\ \vdots \\ h_{I-1}^n \\ h_I^n \\ h_{I+1}^n \end{bmatrix} \quad (\text{C.3})$$

The additional factor of 2 that appears in matrix entry $(I, I - 1)$ is due to the application of a “ghost point” (Causon & Mingham, 2010), which is required

because of the no-flux boundary condition at the sidewalls i.e. $\partial h/\partial y = 0$ when $y = \pm L$.

Equation (C.3) is solved using a shooting method. Thus an initial guess is provided for h_1^{n+1} , whose value is refined through iteration whilst enforcing volume conservation via (2.40) (Causon & Mingham, 2010). The discrete form of (2.40) reads

$$\phi \Delta y \sum_{i=1}^I \left[\frac{(h_{i+1}^{n+1} + h_i^{n+1})}{2} - \frac{(h_{i+1}^n + h_i^n)}{2} \right] = Q_g (H - h_1^n) \Delta t. \quad (\text{C.4})$$

The left hand side of (C.4), discretized in space, represents the volume displaced by the advancing first front over time Δt , whereas the right hand side of the equation, discretized in time, represents the volume of discharged plume fluid supplied over the same time interval.

Appendix D

Uniform porous medium experimental details

Table D.1 provides the details of the experiments described in section 2.4. Parameters such as F_0 , Re_0 and Pe_0 are defined previously whereas Re_H , the plume Reynolds number at the bottom of the control volume is estimated from

$$\text{Re}_H = \frac{U(H)d_0}{\nu} = \left[\left(\frac{4F_0k}{\pi^3\nu^3\Lambda} \right)^2 \frac{\alpha^3}{\phi(H+x_0)} \right]^{1/4}. \quad (\text{D.1})$$

The velocity $U(x) = \frac{\alpha u(x)}{d_0}$ is a characteristic velocity where the transport velocity $u(x)$ is calculated by dividing the plume volume flux by its cross-sectional area. Thus,

$$U(x) = \frac{\alpha}{d_0} \frac{Q(x)}{\Lambda[y(\eta = \pi) - y(\eta = -\pi)]}. \quad (\text{D.2})$$

Finally the error, ϵ , is calculated via

$$\epsilon = \frac{100\%}{N} \left(\sum_1^N \frac{\bar{h}_{ex} - \bar{h}_{th}}{\bar{h}_{ex}} \right), \quad (\text{D.3})$$

where N is the number of experimental images collected (typically 60) and \bar{h}_{ex} and \bar{h}_{th} are the time-dependent measured and predicted first front heights. The value of \bar{h}_{th} , determined from (2.44), directly depends upon the plume volume flux, Q . Therefore, it is understood that the value of ϵ obtained using (D.3) incorporates the deviation of the theoretically predicted volume flux from its corresponding experimental value.

Table D.1: A summary of the experimental parameters: bead diameter, d_0 , permeability, k , source volume flux, Q_0 , source reduced gravity, g'_0 , source buoyancy flux, F_0 , source Reynolds number, Re_0 , plume Reynolds number at the bottom boundary, Re_H (defined in D.1), source Péclet number, Pe_0 , and the mean error, ϵ (defined in D.3).

Expt no.	d_0 (cm)	k ($\times 10^{-4}$ cm ²)	Q_0 (cm ³ s ⁻¹)	g'_0 (cm s ⁻²)	F_0 (cm ⁴ s ⁻³)	Re_0	Re_H	Pe_0 ($\times 10^3$)	ϵ (%)
1	0.3	0.78	0.20	24.53	4.91	2.14	0.05	1.60	1.65
2	0.3	0.78	0.49	24.53	12.02	5.25	0.08	3.92	4.72
3	0.3	0.78	0.75	24.53	18.39	8.04	0.10	6.00	3.25
4	0.3	0.78	0.90	54.94	49.44	9.64	0.17	7.20	-2.29
5	0.3	0.78	0.18	54.94	9.89	1.93	0.08	1.44	0.21
6	0.3	0.78	0.84	54.94	46.15	9.00	0.17	6.72	1.93
7	0.3	0.78	0.17	85.35	14.51	1.82	0.09	1.36	-3.49
8	0.3	0.78	0.90	85.35	76.81	9.64	0.22	7.20	1.58
9	0.3	0.78	0.53	85.35	45.23	5.68	0.17	4.24	1.98
10	0.5	2.20	0.30	21.09	6.33	5.36	0.10	4.00	-4.27
11	0.5	2.20	0.60	21.09	12.65	10.71	0.15	8.00	-4.85
12	0.5	2.20	1.00	21.09	21.09	17.86	0.19	13.3	-3.48
13	0.5	2.20	1.00	58.86	58.86	17.86	0.32	13.3	1.37
14	0.5	2.20	0.60	58.86	35.32	10.71	0.25	8.00	-4.38
15	0.5	2.20	0.61	94.18	57.45	10.89	0.32	8.13	-4.85
16	0.5	2.20	0.92	94.18	86.64	16.43	0.39	12.26	-3.72

Appendix E

Layered porous medium experimental details

Tables E.1, E.2 and E.3 specify the parameters for the 50 experiments that were performed with the height ratios $H_1/H_2 = 0.5, 1.0$ and 2.0 , respectively.

Table E.1: Summary of the experimental parameters for the cases where $H_1/H_2 = 0.5$. Here d_1 and d_2 respectively denote the bead diameters of the upper and lower layers. Moreover, k_1 and k_2 respectively denote the permeabilities of the upper and lower layers. Furthermore, Q_0 and g'_0 are the source volume flux and reduced gravity. Horizontal lines separate the experiments with identical permeability ratios. Note that $\phi_1/\phi_2 = 1.0$ in all cases.

Expt no.	d_1 (cm)	d_2 (cm)	k_1 ($\times 10^{-5}$ cm ²)	k_2 ($\times 10^{-5}$ cm ²)	k_1/k_2	Q_0 (cm ³ s ⁻¹)	g'_0 (cm s ⁻²)
1	0.1	0.5	0.87	21.80	0.04	0.30	29.43
2	0.1	0.5	0.87	21.80	0.04	0.80	29.43
3	0.1	0.3	0.87	7.84	0.11	0.30	29.43
4	0.1	0.3	0.87	7.84	0.11	0.80	29.43
5	0.3	0.5	7.84	21.80	0.36	0.30	29.43
6	0.3	0.5	7.84	21.80	0.36	0.80	29.43
7	0.5	0.3	21.80	7.84	2.78	0.30	29.43
8	0.5	0.3	21.80	7.84	2.78	0.80	29.43
9	0.3	0.1	7.84	0.87	9.0	0.30	29.43
10	0.3	0.1	7.84	0.87	9.0	0.80	29.43
11	0.3	0.1	7.84	0.87	9.0	0.30	78.48
12	0.3	0.1	7.84	0.87	9.0	0.80	78.48
13	0.5	0.1	21.80	0.87	25.0	0.30	29.43
14	0.5	0.1	21.80	0.87	25.0	0.80	29.43
15	0.5	0.1	21.80	0.87	25.0	0.30	78.48

Table E.2: As in table E.1 but with $H_1/H_2 = 1.0$.

Expt no.	d_1 (cm)	d_2 (cm)	k_1 ($\times 10^{-5} \text{ cm}^2$)	k_2 ($\times 10^{-5} \text{ cm}^2$)	k_1/k_2	Q_0 ($\text{cm}^3 \text{ s}^{-1}$)	g'_0 (cm s^{-2})
16	0.1	0.5	0.87	21.80	0.04	0.30	29.43
17	0.1	0.5	0.87	21.80	0.04	0.75	29.43
18	0.1	0.5	0.87	21.80	0.04	0.30	78.48
19	0.1	0.5	0.87	21.80	0.04	0.75	78.48
20	0.1	0.3	0.87	7.84	0.11	0.30	29.43
21	0.1	0.3	0.87	7.84	0.11	0.30	78.48
22	0.1	0.3	0.87	7.84	0.11	0.75	78.48
23	0.1	0.3	0.87	7.84	0.11	0.30	48.07
24	0.3	0.5	7.84	85.35	0.36	0.30	29.43
25	0.3	0.5	7.84	21.09	0.36	0.80	29.43
26	0.3	0.5	7.84	21.09	0.36	0.30	78.48
27	0.3	0.5	7.84	21.09	0.36	0.80	78.48
28	0.5	0.3	21.80	7.84	2.78	0.30	31.39
29	0.5	0.3	21.80	7.84	2.78	0.80	31.39
30	0.5	0.3	21.80	7.84	2.78	0.30	77.49
31	0.5	0.3	21.80	7.84	2.78	0.75	77.49
32	0.3	0.1	21.80	0.87	25.0	0.25	21.20
33	0.3	0.1	21.80	0.87	25.0	0.75	21.20
34	0.3	0.1	21.80	0.87	25.0	0.25	82.40
35	0.3	0.1	21.80	0.87	25.0	0.75	82.40
36	0.3	0.1	7.84	0.87	9.0	0.30	48.07
37	0.5	0.1	7.84	0.87	9.0	0.30	17.16
38	0.5	0.1	7.84	0.87	9.0	0.30	31.39
39	0.5	0.1	7.84	0.87	9.0	0.80	31.39
40	0.5	0.1	7.84	0.87	9.0	0.80	81.42

Table E.3: As in table E.1 but with $H_1/H_2 = 2.0$.

Expt no.	d_1 (cm)	d_2 (cm)	k_1 ($\times 10^{-5} \text{ cm}^2$)	k_2 ($\times 10^{-5} \text{ cm}^2$)	k_1/k_2	Q_0 ($\text{cm}^3 \text{ s}^{-1}$)	g'_0 (cm s^{-2})
41	0.1	0.5	0.87	21.80	0.04	0.30	23.43
42	0.1	0.5	0.87	21.80	0.04	0.40	23.43
43	0.1	0.3	0.87	7.84	0.11	0.70	43.16
44	0.3	0.5	7.84	21.80	0.36	0.30	29.43
45	0.3	0.5	7.84	21.80	0.36	0.80	29.43
46	0.5	0.3	21.80	7.84	2.78	0.30	43.16
47	0.5	0.3	21.80	7.84	2.78	0.70	43.16
48	0.3	0.1	7.84	0.87	9.0	0.25	43.16
49	0.3	0.1	7.84	0.87	9.0	0.50	43.16
50	0.5	0.1	21.09	7.84	25.0	0.25	43.16

Appendix F

List of symbols

Table F.1 presents a list of all symbols used in the thesis with their respective definitions and dimensions.

Table F.1: List of variables.

Symbol	Meaning	Unit
α	dispersivity	cm
β	solute contraction coefficient	cm ³ /g
η	similarity variable	-
λ	gravity current dimensionless length	-
Λ	source width (line nozzle length)	cm
μ	dynamic viscosity	g/(cms)
ν	kinematic viscosity	cm ² /s
ϕ	porosity	-
ϕ_1, ϕ_2	upper, lower layer porosity	-
ρ	density	g/cm ³
ρ_0, ρ_∞	density	g/cm ³
τ	tortuosity	-
ξ	similarity variable	-
ξ_N	gravity current dimensionless radius	-
A	control volume, tank cross-section	cm ²
A_1, A_2, A_3	constants	-
b	draining fluid depth, plume radius	cm
C, C_0	solute concentration, source solute concentration	g/cm ³
\bar{C}	mean solute concentration of plume	g/cm ³
d_0	bead diameter, mean grain size	cm
D_d	molecular diffusion coefficient	cm ² /s
D, D_L, D_T	mechanical dispersion coefficient	cm ² /s
F, F_0	buoyancy, source buoyancy	cm ⁴ /s ³
$\mathcal{F}, \mathcal{G}, \mathcal{H}$	similarity functions	-
g'_0, \bar{g}'	source, mean reduced gravity of plume	cm/s ²

g'_g, g'_1, g'_{2A}	reduced gravity of the gravity currents based on plume	cm/s ²
g'_{2B}	reduced gravity of the draining fluid	cm/s ²
h	gravity current, first front height	cm
\bar{h}, h_f	mean first front height	cm
$\bar{h}_{tL}, \bar{h}_{tR}$	mean gravity current height when it reaches sidewall	cm
H	control volume height	cm
H_1, H_2	upper, lower layer height	cm
I	image intensity	-
k	permeability	cm ²
k_1, k_2	upper, lower layer permeability	cm ²
m, n, p, q	constants	-
L, R	control volume horizontal length, radius from center	cm
L_g	gravity current length	cm
\check{L}_g	gravity current runout length	cm
p	pressure	Pa
Pe	Peclet number	-
Re	Reynolds number	-
Q, Q_0	volume flux, source volume flux	cm ³ /s
Q_g, Q_1, Q_2	gravity current volume flux	cm ³ /s
q_g, q_1, q_2	gravity current volume flux per unit length	cm ² /s
r	radial coordinate	cm
r_N	gravity current radius	cm
S	Buoyancy parameter	cm/s
Sc	Scmidt number	-
t	time	s
$t_P, t_H, t_L/t_R$	time scales: plume, first front, gravity current	s
u	horizontal velocity, horizontal velocity	cm/s
U, \bar{U}	mean transport velocity	cm/s
U_f	mean first front velocity	cm/s
v	horizontal velocity	cm/s
v_g	gravity current horizontal velocity	cm/s
V	total volume, gravity current volume	cm ³
V_g	gravity current volume	cm ³
x	vertical coordinate	cm
y	horizontal coordinate	cm

Bibliography

- ACTON, J. M., HUPPERT, H. E. & WORSTER, M. G. 2001 Two-dimensional viscous gravity currents flowing over a deep porous medium. *J. Fluid Mech.* **440**, 359–380.
- ALHASHASH, A., SALEH, H. & HASHIM, I. 2013 Effect of conduction in bottom wall on benard convection in a porous enclosure with localized heating and latent cooling. *Transp. Porous Med.* **96**, 305–318.
- BAINES, S. J. & WORDEN, R. H. 2004 Geological storage of carbon dioxide. *Geological Society, London* **233**, 1–6.
- BAINES, W. D. & TURNER, J. S. 1969 Turbulent buoyant convection from a source in a confined region. *J. Fluid Mech.* **37**, 51–80.
- BAKER, E. T., LAVELLE, J. W., FEELY, R. A., MASSOTH, G. J. & WALKER, S. L. 1989 Episodic venting of hydrothermal fluids from the juan de fuca ridge. *J. Geophys. Res.* **95**, 9237–9250.
- BARNETT, S. J. 1991 The dynamics of buoyant releases in confined spaces. PhD thesis, DAMTP, University of Cambridge.
- BEAR, J. 1972 *Dynamics of fluids in porous medium*. American Elsevier.
- BEAR, J. & VERRUIJT, A. 1987 *Modelling Groundwater Flow and Pollution*. D. Reid, Norwell, MA, USA.
- BEJAN, A. & KHAIR, K. R. 1985 Heat and mass transfer by natural convection in a porous medium. *Int. J. Heat Mass Transfer* **28**, 909–918.
- BICKLE, M., CHADWICK, A., HUPPERT, H. E., HALLWORTH, M. & LYLE, S. 2007 Modelling carbon dioxide accumulation at sleipner: Implications for underground carbon storage. *Earth and Planetary Science Letters* **255**, 164–176.
- BICKLE, M. J. 2009 Geological carbon storage. *Nature Geoscience* **2**, 815–818.
- BOLSTER, D. 2014 The fluid mechanics of dissolution trapping in geologic storage of CO_2 . *J. Fluid Mech.* **740**, 1–4.
- BRITTER, B. E. 1979 The spread of a negatively buoyant plume in a calm environment. *Atmospheric Environment* **13**, 1241–1247.
- BUBNOVICH, V. & TOLEDO, M. 2007 Analytical modeling of filtration combustion in inert porous media. *Applied Thermal Engineering* **27**, 1144–1149.

- BUSH, J. & WOODS, A. W. 1999 Vortex generation by line plumes in a rotating stratified fluid. *J. Fluid Mech.* **388**, 289–313.
- CAULFIELD, C. P. & WOODS, A. W. 2002 The mixing in a room by a localized finite-mass-flux source of buoyancy. *J. Fluid Mech.* **471**, 33–50.
- CAUSON, D. & MINGHAM, C. G. 2010 *Introductory Finite Difference Methods for PDEs*. Ventus Publishing ApS.
- CHEN, K. S. & HO, J. R. 1986 Effect of flow inertia on vertical natural convection in saturated porous media. *Int. J. Heat Mass Transfer* **29**, 753–759.
- DELGADO, J. M. P. Q. 2007 Longitudinal and transverse dispersion in porous media. *ICChemE* **85**, 1245–1252.
- DICKINSON, J. S., BUIK, N., MATTHEWS, M. C. & SNIJDERS, A. 2009 Aquifer thermal energy storage: theoretical and operational analysis. *Geotechnique* **59**, 249–260.
- DRAZIN, P. G. & REID, W. H. 2004 *Hydrodynamic stability*. Cambridge University press.
- DUDFIELD, P. & WOODS, A. W. 2012 On the periodic injection of fluid into, and its extraction from, a porous medium for seasonal heat storage. *J. Fluid Mech.* **707**, 467–481.
- DULLIEN, F. A. L. 1992 *Porous medium fluid transport and pore structures*. Academic press.
- DUTIL, Y., ROUSSE, D. R., SALAH, N. B., LASSUE, S. & ZALEWSKI, L. 2011 A review on phase change materials: Mathematical modeling and simulations. *Renewable and Sustainable Energy Reviews* **15**, 112–130.
- ENNIS-KING, J. & PATERSON, L. 2003 Role of convective mixing in the long-term storage of carbon dioxide in deep saline formations. *Society of Petroleum Engineers Inc. SPE* **84344**, 1–12.
- ERGUN, S. 1952 Fluid flow through packed columns. *Chem. Eng. Prog.* **48**, 89–94.
- GERMELES, A. E. 1975 Forced plumes and mixing of liquids in tanks. *J. Fluid Mech.* **71**, 601–623.
- GODA, T. & SATO, K. 2011 Gravity currents of carbon dioxide with residual gas trapping in a two-layered porous medium. *J. Fluid Mech.* **673**, 60–79.
- GUIN, J. A., KESSLER, D. P. & GREENKORN, R. A. 1972 The dispersion tensor in anisotropic porous media. *Ind. Eng. Chem. Fundam.* **11-4**, 477–482.
- GUNN, I. & WOODS, A. W. 2011 On the flow of buoyant fluid injected into a confined, inclined aquifer. *J. Fluid Mech.* **672**, 109–129.
- HAPPEL, J. & BRENNER, H. 1991 *Low Reynolds Number Hydrodynamics: With Special Applications to Particulate Media*, 2nd edn. Kluwer Academic.
- HEAD, J. W. & WILSON, L. 2003 Deep submarine pyroclastic eruptions: theory and predicted landforms and deposits. *J. Volcanol. Geotherm. Res.* **121**, 155–196.

- HOMSY, G. M. 1987 Viscous fingering in porous media. *Ann. Rev. Fluid Mech.* **19**, 271–311.
- HOUSEWORTH, J. E. 1984 Longitudinal dispersion in non-uniform, isotropic porous media. *Tech. Rep.* KH-R-45. California Institute Of Technology, Pasadena, California.
- HUGHES, G. O. & GRIFFITHS, R. W. 2006 A simple convective model of the global overturning circulation, including effects of entrainment into sinking regions. *Ocean Modelling* **12**, 46–79.
- HUNT, G. R. & KAYE, N. G. 2001 Virtual origin correction for lazy turbulent plumes. *J. Fluid Mech.* **435**, 377–396.
- HUPPERT, H. E. 1986 The intrusion of fluid mechanics into geology. *J. Fluid Mech.* **173**, 557–594.
- HUPPERT, H. E. & NEUFELD, J. A. 2014 The fluid mechanics of carbon dioxide sequestration. *Annu. Rev. Fluid Mech.* **46**, 255–272.
- HUPPERT, H. E. & WOODS, A. W. 1995 Gravity-driven flows in porous layers. *J. Fluid Mech.* **292**, 55–69.
- IGLAUER, S. 2011 Dissolution trapping of carbon dioxide in reservoir formation brine – a carbon storage mechanism. In *Mass Transfer – Advanced Aspects*, chap. 10, pp. 233–262. InTechOpen.
- JUMAH, R. Y., BANAT, F. A. & ABU-AL-RUB, F. 2001 Darcy-forchheimer mixed convection heat and mass transfer in fluid saturated porous media. *I. J. Num. Meth. Heat & Fluid Flow* **11**, 600–618.
- KAYE, N. B. & HUNT, G. R. 2007 Overturning in a filling box. *J. Fluid Mech.* **576**, 297–323.
- KESTIN, J., KHALIFA, H. E. & CORREIA, R. J. 1981 Tables of the dynamic and kinematic viscosity of aqueous nacl solutions in the temperature range 20-150 ° c and the pressure range 0.1-35mpa. *J. Phys. Chem. Ref. Data* **10**, 71–87.
- KHACHIKIAN, C. & HARMON, T. C. 2000 Nonaqueous phase liquid dissolution in porous media: current state of knowledge and research needs. *Transport in Porous Media* **38**, 3–28.
- KNEAFSEY, T. J. & PRUESS, K. 2010 Laboratory flow experiments for visualizing carbon dioxide-induced, density-driven brine convection. *Transp. Porous Med.* **82**, 123–139.
- KUEPER, B. H., WEALTHALL, G. P., SMITH, J. W. N., LEHARNE, S. A. & LERNER, D. N. 2003 An illustrated handbook of dnapl transport and fate in the subsurface. *Tech. Rep.* R&D Publication 133. Environment Agency.
- LAI, F. C. 1991 Non-darcy convection from a line source of heat in a saturated porous medium. *Int. Comm. Heat Mass Transfer* **18**, 445–457.
- LESAGE, S. & JACKSON, R. E. 1992 *Groundwater contamination and analysis at hazardous waste sites*. Marcel Dekker, Inc.

- LEU, J. & JANG, J. 1995 The natural convection from a point heat source embedded in a non-darcian porous medium. *Int. J. Heat Mass Transfer* **38**, 1097–1104.
- LINDEN, P. F., LANE-SERFF, G. F. & SMEED, D. A. 1990 Emptying filling boxes: the fluid mechanics of natural ventilation. *J. Fluid Mech.* **212**, 309–335.
- LOUBENS, R. D. & RAMAKRISHNAN, T. S. 2011 Analysis and computation of gravity-induced migration in porous media. *J. Fluid Mech.* **675**, 60–86.
- LYLE, S., HUPPERT, H. E., HALLWORTH, M., BICKLE, M. & CHADWICK, A. 2005 Axisymmetric gravity currents in a porous medium. *J. Fluid Mech.* **543**, 293–302.
- MACKAY, D. J. 2009 *Sustainable energy – without the hot air*. UIT Cambridge Ltd.
- MACMINN, C. W., NEUFELD, J. A., A., H. M. & HUPPERT, H. E. 2012 Spreading and convective dissolution of carbon dioxide in vertically confined, horizontal aquifers. *Water Resour. Res.* **48**, 1–11.
- MANINS, P. C. 1979 Turbulent buoyant convection from a source in a confined region. *J. Fluid Mech.* **91**, 765–781.
- MANSOUR, M. A., AHMED, S. E. & Y., B. M. A. 2013 Free convection in h-shaped enclosures filled with a porous medium saturated with nanofluids mounted heaters on the vertical walls. *Special Topics & Reviews in Porous Media – An International Journal* **4**, 287–297.
- MCCURDY, R. 2011 Underground injection wells for produced water disposal. *Tech. Rep.*. USEPA Technical Workshops for the Hydraulic Fracturing Study: Water Resource Management. United States Environmental Protection Agency, Office of Research and Development.
- MORTON, B. R., TAYLOR, G. I. & TURNER, J. S. 1956 Turbulent gravitational convection from maintained and instantaneous sources. *Proc. R. Soc. Lond. A* **234**, 1–23.
- NABI, S. & FLYNN, M. R. 2013 The hydraulics of exchange flow between adjacent confined building zones. *Building and Environment* **59**, 76–90.
- NAKAYAMA, A. 1994 A unified theory for non-darcy free, forced, and mixed convection problems associated with a horizontal line heat source in a porous medium. *Trans. ASME* **116**, 508–513.
- NALLUSAMY, N., SAMPATH, S. & VELRAJ, R. 2007 Experimental investigation on a combined sensible and latent heat storage integrated with constant/varying (solar) heat sources. *Renewable Energy* **32**, 1206–1227.
- NEUFELD, J. A., HESSE, M. A., RIAZ, A., HALLWORTH, M. A., TCHELEPI, M. A. & HUPPERT, H. E. 2010 Convective dissolution of carbon dioxide in saline aquifers. *Geophysical Research Letters* **37**, 1–5.
- NEUFELD, J. A., VELLA, D. & HUPPERT, H. E. 2009 The effect of a fissure on storage in a porous medium. *J. Fluid Mech.* **639**, 239–259.

- NEUFELD, J. A., VELLA, D., HUPPERT, H. E. & LISTER, J. R. 2011 Leakage from gravity currents in a porous medium. part 1. a localized sink. *J. Fluid Mech.* **666**, 391–413.
- NICHOLSON, M. & FLYNN, M. R. 2015 Gravity current flow over sinusoidal topography in a two-layer ambient. *Phys. Fluids* **27**, 096603, 1–20.
- NIELD, D. A. 1968 Onset of thermohaline convection in a porous medium. *Water Resour. Res.* **4–3**, 553–560.
- NIELD, D. A. & BEJAN, A. 2013 *Convection in porous media*, 4th edn. Springer.
- NIELD, D. A. & KUZNETSOV, A. V. 2013 A historical and topical note on convection in porous media. *Journal of Heat Transfer* **135**, 1–10.
- NIZAMI, D. J., LIGHTSTONE, M. F., HARRISON, S. J. & CRICKSHANK, C. A. 2013 Negative buoyant plume model for solar domestic hot water tank systems incorporating a vertical inlet. *Solar Energy* **87**, 53–63.
- NORDELL, B. 2000 Large-scale thermal energy storage. *Energy and Environment* pp. 1–10.
- OGATA, A. 1970 Theory of dispersion in a granular medium. *Tech. Rep.* 411-1. U.S. Geol. Surv. Prof. Pap.
- OOSTROM, M., ROCKHOLD, M. L., THORNE, P. D., TRUEX, M. J., LAST, G. V. & ROHAY, V. J. 2007 Carbon tetrachloride flow and transport in the subsurface of the 216-z-9 trench at the hanford site. *Soil Science Society of America* **6-4**, 971–984.
- OZTOP, H. F., ESTELLE, P., YAN, W., AL-SALEM, K., ORFI, J. & MAHIAN, O. 2015 A brief review of natural convection in enclosures under localized heating with and without nanofluids. *Int. Comm. Heat and mass Transfer* **60**, 37–44.
- PARLANGE, M. B. & HOPMANS, J. W. 1999 *Vadose Zone Hydrology*. Oxford University Press.
- PETERS, E. J. 2012 *Advanced Petrophysics*. Live Oak Book Company.
- PHILLIPS, O. M. 1991 *Flow and Reactions in Permeable Rocks*. 1st edn. Cambridge University Press.
- POLING, B. E., PRAUSNITZ, J. M. & O’CONNELL, J. P. 2000 *The Properties of Gases and Liquids*. McGraw-Hill.
- PRITCHARD, D. & HOGG, A. J. 2002 Draining viscous gravity currents in a vertical fracture. *J. Fluid Mech.* **459**, 207–216.
- PRITCHARD, D., WOODS, A. W. & HOGG, A. J. 2001 On the slow draining of a gravity current moving through a layered permeable medium. *J. Fluid Mech.* **444**, 23–47.
- RAMSING, N. & GUNDERSEN, J. 1994 Seawater and gases. *Tech. Rep.*. Max Planck Institute for Marine Microbiology. Bremen, Germany.
- RIAZ, A., HESSE, M., TCHELEPI, H. A. & ORR, F. M. 2006 Onset of convection in a gravitationally unstable diffusive boundary layer in porous media. *J. Fluid Mech.* **548**, 87–111.

- ROES, M. A. 2014 Buoyancy-driven convection in a ventilated porous medium. Master's thesis, University of Alberta.
- ROES, M. A., BOLSTER, D. T. & FLYNN, M. R. 2014 Buoyant convection from a discrete source in a leaky porous medium. *J. Fluid Mech.* **755**, 204–229.
- SAFFMAN, P. G. & TAYLOR, S. G. 1958 The penetration of fluid into a porous medium or hele-shaw cell containing a more viscous liquid. *Proc. R. Soc. Lond. A*, 312–329.
- SAHU, C. K. & FLYNN, M. R. 2015 Filling box flows in porous media. *J. Fluid Mech.* **782**, 455–478.
- SAHU, C. K. & FLYNN, M. R. 2016a The effect of sudden permeability changes in porous media filling box flows. *J. Fluid Mech.* (**submitted**), 1–26.
- SAHU, C. K. & FLYNN, M. R. 2016b Filling box flows in an axisymmetric porous medium. *Transp. Porous Med.* **112**, 619–635.
- SALEH, H. & HASHIM, I. 2013 Non-darcy and localized heating effects on benard convection in porous enclosure. *J. Porous Med.* **16**, 1–10.
- SARAFRAZ, P. 2013 Thermal optimization of flat plate pcm in natural convection solar water heating systems. Master's thesis, McMaster University.
- SAUTY, J. P., GRINGARTEN, A. C., MENJOZ, A. & LANDEL, P. A. 1982 Sensible energy storage in aquifers: Theoretical study. *Water Resour. Res.* **18**, 245–252.
- SCHEIDEGGER, A. E. 1961 General theory of dispersion in porous media. *J. Geophys. Res.* **66-10**, 3273–3278.
- SCHULZE, S., NIKRITYUK, P. A. & MEYER, B. 2015 Porosity distribution in monodisperse and polydisperse fixed beds and its impact on the fluid flow. *Particulate Science and Technology* **33**, 23–33.
- SHAFFER, D. L., CHAVEZ, L. H. A., BEN-SASSON, M., CASTRILLON, S. R., YIP, N. Y. & ELIMELECH, M. 2013 Desalination and reuse of high-salinity shale gas produced water: drivers, technologies, and future directions. *Environ. Sci. Technol.* **47**, 9569–9583.
- SHIN, J. O., DALZIEL, S. B. & LINDEN, P. F. 2004 Gravity currents produced by lock exchange. *J. Fluid Mech.* **521**, 1–34.
- SIDDIKI, M. N., MOLLA, M. M. & SAHA, S. C. 2015 Natural convection flow in porous enclosure with localized heating below with heat flux. *Proc. ICME 2015* pp. 1–6.
- SPANNUTH, M. J., NEUFELD, J. A., WETTLAUFER, J. S. & WORSTER, M. G. 2009 Axisymmetric viscous gravity currents flowing over a porous medium. *J. Fluid Mech.* **622**, 135–144.
- SPEER, K. & MARSHALL, J. 1995 The growth of convective plumes at seafloor hot springs. *J. Marine Res.* **53**, 1025–1057.
- SPEER, K. & RONA, K. 1989 A model of an atlantic and pacific hydrothermal plume. *J. Geophys. Res.* **94**, 6213–6220.

- SZULCZEWSKI, M. L., HESSE, M. A. & JUANES, R. 2013 Carbon dioxide dissolution in structural and stratigraphic traps. *J. Fluid Mech.* **736**, 287–315.
- THOMAS, L. P., MARINO, B. M. & LINDEN, P. F. 1998 Gravity currents over porous substrates. *J. Fluid Mech.* **366**, 239–258.
- TURCOTTE, D. L. & SCHUBERT, G. 2014 *Geodynamics*. 3rd edn. Cambridge University Press.
- UNGARISH, M. & HUPPERT, H. E. 2000 High-reynolds-number gravity currents over a porous boundary: shallow-water solutions and box-model approximations. *J. Fluid Mech.* **418**, 1–23.
- VELLA, D. & HUPPERT, H. E. 2006 Gravity currents in a porous medium at an inclined plane. *J. Fluid Mech.* **555**, 353–362.
- WATCH, L. M., BECKER, J. & SEAGREN, E. 2014 Two phase flow of dense non-aqueous phase tetrachloroethene in a microfluidic groundwater model. *Tech. Rep.*. Michigan Technological University.
- WINSAUER, W. O., SHEARIN, H. M., MASSON, P. H. & WILLIAMS, M. 1952 Resistivity of brine-saturated sands in relation to pore geometry. *AAPG Bull.* **36–2**, 253–277.
- WOODING, R. A. 1963 Convection in a saturated porous medium at large rayleigh number or pécelet number. *J. Fluid Mech.* **15**, 527–544.
- WOODS, A. W. 1999 Liquid and vapour flow in superheated rock. *Annu. Rev. Fluid Mech.* **31**, 171–199.
- WOODS, A. W. 2010 Turbulent plumes in nature. *Annu. Rev. Fluid Mech.* **42**, 391–412.
- WOODS, A. W. & MASON, R. 2000 The dynamics of two-layer gravity-driven flows in permeable rock. *J. Fluid Mech.* **421**, 83–114.
- ZAKHAROV, Z. 2009 Bessel functions and their applications to solutions of partial differential equations. *Math 456 Lecture Notes, University of Arizona* .